Master's thesis

NTNU
Norwegian University of Science and Technology
Faculty of Natural Sciences
Department of Materials Science and Engineering

Erik Aas Koren

The Effect of Cooling Rate and Pre-Deformation on Corrosion Behaviour of Extruded AlMgSi(Cu, Zn)-Alloys

Master's thesis in Chemical Engineering and Biotechnology
Supervisor: Trond Furu, Otto Lunder, Andreas Erbe
July 2020

NTNU
Norwegian University of
Science and Technology

Erik Aas Koren

The Effect of Cooling Rate and Pre-Deformation on Corrosion Behaviour of Extruded AlMgSi(Cu, Zn)-Alloys

Master's thesis in Chemical Engineering and Biotechnology
Supervisor: Trond Furu, Otto Lunder, Andreas Erbe
July 2020

Norwegian University of Science and Technology
Faculty of Natural Sciences
Department of Materials Science and Engineering

NTNU
Norwegian University of
Science and Technology

Preface

This master's thesis is written during the spring semester of 2020, and finalises the five year study program Chemical Engineering and Biotechnology at NTNU. The thesis is a continuation of a preliminary specialisation project carried out during the fall of 2019, and it is conducted as a part of the *Fundamentals of Intergranular Corrosion in Aluminium Alloys (FICAL)* project, which is a collaboration between NTNU, Hydro, SINTEF, Steertec, Beneteler and Gränges.

The experimental work conducted by the author was performed at the Department of Materials Science and Engineering (IMA) at NTNU. Materials used for the thesis was provided by Hydro. TEM sample preparation was performed by Birgitte Karlsen (SINTEF) and Calin D. Marioara (SINTEF) did the TEM analysis. Stretching of profiles was performed by Pål Christian Skaret (IMA).

Erik Aas Koren
July 2020, Trondheim

Acknowledgements

I would like to thank my supervisor, Trond Furu[1,2], and my co-supervisors, Otto Lunder[2] and Andreas Erbe[3], for sharing your knowledge and expertise over the last year. Your guidance have been of most importance for me during this project.

Further, I would like to thank Berit Vinje Kramer[3] for training and help with sample preparation and heat treatments. Yingda Yu[3] deserves recognizing for helping me with SEM and EBSD analysis. For help conducting corrosion test I would like to thank Anita Storsve[3]. I also want to express my gratitude to everyone who has performed experimental work which I was not able to do or participate in due the restrictions. A big thank you to Pål Christian Skaret[3] who performed stretching of the profiles and to Birgitte Karlsen[4] who performed TEM sample preparation. Calin D. Marioara[2] deserves great recognition for performing TEM analysis and for help with interpretation of the results.

Finally, I would like to thank my family for their support over the last five years and to Anne for your support and encouragement during the course of this project.

[1]Norsk Hydro
[2]SINTEF Industry, Materials and Nanotechnology
[3]Department of Materials Science and Engineering, NTNU
[4]SINTEF Industry, Metal Production and Processing

Abstract

Aluminium alloys of the 6xxx-series, having a high strength-to-weight ratio, can contribute to reducing the emission of greenhouse gases (GHG) due to weight reduction in the transportation industry. Recycling of these components can further contribute to reducing GHG emission, as recycling only requires 5% of the energy required to produce primary aluminium. Trace elements may accumulate during recycling, and affect mechanical- and corrosion properties of the end product. Copper has a positive effect on hardness, however, it increases the susceptibility to intergranular corrosion (IGC). Copper segregates to the grain boundary and induces a microgalvanic coupling between grain boundary and the adjacent precipitate-free zone (PFZ). Appropriate thermomechanical processing is important to produce products with desirable strength and corrosion resistance.

Four variants of different processing route and six variants of different copper- and zinc-content was studied, resulting in a total of 24 different variants. The processing route was varied by applying either water-quenching or air-cooling after solution heat treatment (SHT) and whether pre-stretching was performed or not. IGC susceptibility was investigated by ISO Standard 11846 Method B, while hardness was measured by Vickers hardness. The microstructure was characterized by polarized light microscopy, SEM and TEM.

Variation in processing route had a more prominent effect on the IGC susceptibility and hardness than the variation of copper- and zinc-content studied. Slower cooling rate from SHT increased the IGC resistance, most likely due to a reduced amount of copper on grain boundaries. However, the reduced cooling rate also leads to decreased hardness. Pre-deformation reduced the severity of IGC attacks in water-quenched variants, but the corrosion mode transitioned into pitting corrosion. Hardness decreased in the water-quenched variant when pre-deformation was applied, which may be because of lower age-hardening response. Increased copper-content slightly increased the hardness and weight loss during IGC testing. The amount of zinc did not affect corrosion properties or hardness. Overall, the results highlight the contradicting effects of corrosion resistance and hardness of extruded AlMgSi-alloys.

Sammendrag

Aluminiumslegeringer i 6xxx-serien med høyt styrke-til-vekt-forhold kan, på grunn av vektreduksjon, bidra til å redusere utslipp av drivhusgasser i transportindustrien. Resirkulering av disse legeringene kan ytterligere bidra til å redusere klimagassutslipp, da resirkulering bare krever 5% av energibehovet nødvendig for å produsere primæraluminium. Sporelementer kan akkumulere under resirkulering, og påvirke mekaniske egenskaper og korrosjonsbestandighet til sluttproduktet. Kobber har en positiv effekt på hardhet, men reduserer bestandigheten mot intergranulær korrosjon ettersom legeringselementer segregeres til korngrenser og danner en mikrogalvanisk kobling mellom korngrensen og presipitatfrisone. Passende termomekaniskprosessering er viktig for å produsere produkter med ønsket styrke og korrosjonsbestandighet.

Fire varianter av forskjellig prosesseringsmetode og seks varianter med forskjellig kobber- og sinkinnhold ble studert. Prosesseringsmetoden ble variert ved å anvende enten vannavkjøling eller luftavkjøling i romtemperatur etter innherding, og om strekking før utherding ble utført eller ikke. Bestandigheten mot intergranulær korrosjon ble undersøkt ved bruk av ISO-standard 11846 Metode B, mens hardhet ble målt ved Vickers-hardhet. Mikrostruktur ble analysert ved bruk av polarisert lysmikroskopi, SEM og TEM.

Hardhet og bestandighet mot intergranulær korrosjon ble i større grad påvirket av varierende prosesseringsmetode enn variasjonene av kobber- og sinkinnhold som ble studert. Langsommere kjølehastighet fra innherding økte resistansen mot intergranulær korrosjon, mest sannsynlig på grunn av redusert mengde kobber på korngrensene, men reduserte den oppnådde hardheten. Pre-deformasjon reduserte alvorlighetsgraden av intergranulær korrosion, men introduserte mottakelighet for gropkorrosjon. Predeformasjon forårsakte redusert hardhet i vannavkjølt variant som kan skyldes lavere utherding respons. Økt kobberinnhold førte til en svak økning i hardhet, men økte vekttapet litt under korrosjonstest. Mengden sink påvirket hverken korrosjonsegenskaper eller hardhet. Resultatene understreker de motstridende effektene på mekaniske egenskaper og korrosjonsbestandighet ofte sett i AlMgSi-legeringer.

Table of Contents

Abbreviations

AC	Air cooling
ANSI	American National Standard Institute
APB	Anti-phase boundary
$\boldsymbol{\beta}$	Equilibrium phase in AlMgSi alloys
$\boldsymbol{\beta'}$	Metastable precursor to β
$\boldsymbol{\beta''}$	Metastable precursor to β'
CCP	Continuous cooling precipitation
EBSD	Electron backscatter diffraction
EDS	Energy-dispersive X-ray spectroscopy
HAGB	High angle grain boundary
HV1	Vickers hardness at 1 kg load
IGC	Intergranular corrosion
ISO	International Organization for Standardization
GHG	Green house gas
GP	Guinier Preston zones
L	Metastable precursor to Q′
LAGB	Low angle grain boundary
NS	Stretching not applied prior to artificial ageing
PFZ	Precipitate free zone
Q	Equilibrium phase in AlMgSi(Cu) alloys
Q′	Metastable precursor to Q
RT	Room temperature
S	Stretching applied prior to artificial ageing
S	Equilibrium phase

SEM	Scanning electron microscopy
SHT	Solution heat treatment
SSSS	Supersaturated solid solution
T6	Solution heat treated and artificially aged to peak hardness
TEM	Transmission electron microscopy
TTP	Time-temperature-precipitation
UCCR	Upper critical cooling rate
WQ	Water quenched
$\boldsymbol{\theta}$	Equilibrium phase

Chapter 1

Introduction

1.1 Background

The goal of the Paris Agreement is to maintain the global average temperature increase well below 2 °C compared to pre-industrial levels by reducing emission of green house gases (GHG) [1]. The only major industry in the European Union having increasing GHG emissions is the transportation industry, with an increase of approximately 20% between 1990 and 2017 [2, 3]. Emission of GHGs in the transportation industry can be reduced by increasing the fuel efficiency by weight reduction of vehicles. Weight reduction can be obtained by replacing heavy steel components with high strength-to-weight ratio components of aluminium alloys [4, 5]. Another contribution to reduction of GHG emission is by recycling of aluminium alloys, as recycling of aluminium only requires 5% of the energy to produce primary aluminium [6].

AlMgSi-alloys are heat treatable which means that increased strength can be achieved by proper thermomechanical processing and alloying. These alloys have desirable properties such as good weldability, corrosion resistance and excellent extrudability, and is often used as medium-strength structural alloys [7, 8]. However, alloying and thermomechanical processing may have undesirable effects on the intergranular corrosion (IGC) susceptibility of the alloys [9, 10, 11]. IGC is type of localized corrosion, that propagates along grain boundaries without significant attack of the grain bodies [12].

As the thermomechanical processing of AlMgSi-alloys affect the susceptibility to IGC, it is desired to investigate possibilities of processing routes that limit IGC susceptibility while still maintaining the mechanical integrity of the products [9, 13]. Difference in quench cooling rate after extrusion or solution heat treatment affect the susceptibility to IGC for AlMgSi-alloys. A faster cooling rate have shown to increase the IGC susceptibility in samples that are artificial aged subsequently [9, 14]. As rapid cooling rates may lead to distortions of extruded profiles, and extrudates are typically straightened by stretching [8, 15]. Deformation introduces dislocation that may affect precipitation during subsequent artificial ageing, which have shown to have a positive effect on the IGC resistance of AlMgSi-alloys [13, 16].

Copper is used as an alloying element to increase the strength, however, it may reduce the resistance to IGC, as it segregates to the grain boundaries and cause a microgal-

vanic coupling with a zone depleted of solutes [7, 9, 17]. Zinc is another element that may reduce the resistance to IGC and may accumulate due to the high solubility in aluminium [18, 19, 20, 21]. Recycling of aluminium alloys can cause accumulation of alloying and trace elements, such as copper and zinc. It is, therefore, important to understand how these elements affect mechanical properties and corrosion behavior to optimize both recycling and material properties [19].

1.2 Objective

The objective of this work is to investigate the effect of cooling rate from solution heat treatment and pre-deformation on the IGC susceptibility of a 6005.04 aluminium alloy. Further, the effect copper- and zinc-content on IGC susceptibility is investigated. Different variants of processing route is obtained by either air-cooling or water-quench after solution heat treatment, and whether pre-deformation, by stretching 5%, is performed or not. Effect of copper- and zinc-content is studied by six different variations in composition, making a total of 24 different variations. Hardness measurements is used to indicate mechanical properties, while susceptibility to IGC is tested by use of the ISO Standard 11846 Method B. IGC susceptibility of the same 6005.04 was investigated in a preliminary specialisation project, and the results will somewhat included and discussed. Relevant parts of the theory presented in the specialisation projected may be elaborated in an adapted way together with additional relevant literature [22].

Chapter 2

Theory

2.1 AlMgSi-alloys

Theory of AlMgSi-alloys that was presented in the specialisation project may, to some extent, be presented in the following sub-chapter together with other literature found relevant [22].

Aluminium alloys with magnesium and silicon as the main alloying elements are the prevailing alloy system in today's automotive industry [23]. These alloying systems are designated as the 6xxx-series by the ANSI standard H35.1 [24]. Alloys of the 6xxx-series are classified as wrought alloys which means that mechanical deformation can increase strength [25]. A combination of properties such as outstanding extrudability, heat treatable to moderately high strength, weldable and excellent corrosion resistance, makes alloys of the 6xxx-series desirable to many industries [7]. Often balanced magnesium- and silicon-content are added, corresponding to the stoichiometric ratio in the equilibrium phase β-Mg_2Si. Copper, manganese and chromium may be added for control of grain size and additional strength [26].

Extruded 6005 aluminium alloys have a desirable combination of properties such as good strength, toughness and surface finish. They can be used in various applications, such as in complex sections for bus, railway and truck structures. A typical composition of a 6005 aluminium alloy is given in Table 2.1 [27].

Table 2.1: Chemical composition of a 6005A aluminium alloy [wt%] [27].

Alloy	Si	Mg	Fe	Mn*	Cu	Zn	Cr	Ti	Other**
6005A	0.5-0.9	0.4-0.7	0-0.35	0-0.5	0-0.3	0-0.2	0-0.3	0-0.1	0.15

* Total amount of Cr+Mn must be between 0.12-0.5 wt%.
** Maximum amount of each element is 0.05 wt%.

2.2 Thermomechanical Processing

The thermomechanical processing of extruded AlMgSi-alloys consists of many steps to produce components with the desired shape and properties. Figure 2.1 illustrates the

typical processing route for extruded aluminium profiles [28]. Each of these steps can to some extent affect the mechanical and corrosion properties of the finished product, and will be further discussed in the following sub-chapters [9, 23, 28].

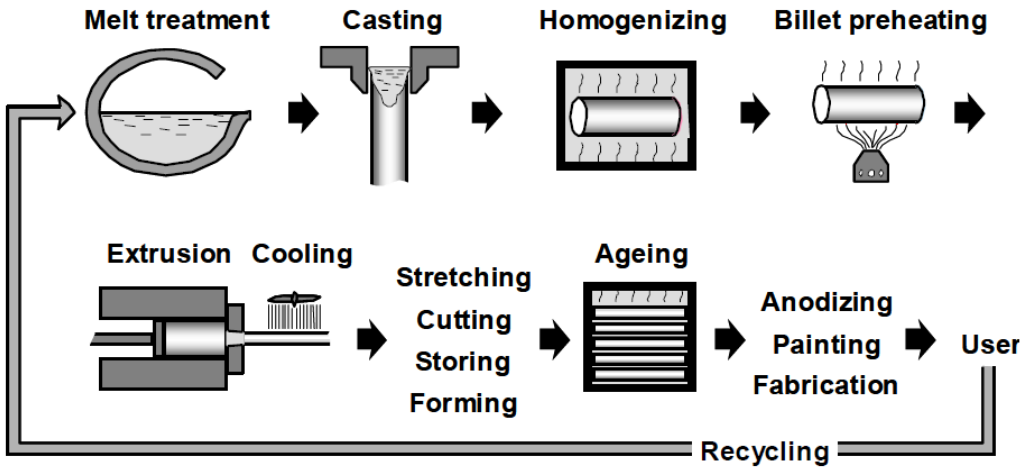

Figure 2.1: Illustration of the process route of extruded aluminium alloys. Reproduced from [28].

2.2.1 Melt Treatment and Casting

First, melt treatment and alloying are performed. Often master alloys containing high melting point elements are melted and mixed with recycled aluminium and high melting point elements, to obtain the desired composition [23]. To produce extrusion billets, semi-continuous direct-chill casting is mostly used, as it produces fine-grained billets at high production rates. Molten aluminium is poured into a water-cooled mould of the desired shape. As the molten aluminium solidifies the bottom, the mould is lowered at a suiting rate. As the solid aluminium exits the mould, water is sprayed onto the solid aluminium [7].

Primary and secondary precipitation occurs as aluminium alloys are cast, and across the grains, there will be a microsegregation of alloying elements [23]. During casting, the presence of iron as an impurity leads to the formation of AlFeMnSi-particles. As iron has very low solid solubility in aluminium, these particles will not dissolve during heat treatment [18, 23, 29]. These particles act as nucleation sites for β-Mg_2 as during quenching, which will be described in more detail in Section 2.3.2 [30].

2.2.2 Homogenisation

Homogenisation takes place in the temperature range of 450-600 °C, and is performed for several reasons. It reduces the effects of microsegregation and coring produced during casting and relieve internal stresses. Soluble elements go into solid solution and a more uniform structure is produced. The mechanism in homogenisation is mainly diffusion of solute elements from grain boundaries and solute rich regions to the grain

bodies to form a uniform distribution. Homogenisation time required depends on the length of the diffusion path and the rate of diffusion, which again depends on the temperature [7, 8, 23].

During heating to homogenisation temperature dispersoids containing silicon, manganese and iron may form. Compared to the AlFeMnSi-particles formed during casting, the dispersoids formed from solid solution are much finer. These dispersoids may act as heterogeneous nucleation sites for MgSi-phases during quenching [30, 31, 32]. Increased cooling rate after homogenisation increases the extrudability and is related to the size of Mg_2Si-particles. Rapidly cooled alloys will contain finer Mg_2Si-particles which will easily dissolve during extrusion preheating, while coarser Mg_2Si-particles will need longer time before dissolving and can cause surface tearing during extrusion. Water quench subsequent to homogenisation can prevent any precipitation of Mg_2Si-particles [28].

2.2.3 Extrusion

Extrusion is a process where a billet is pressed by a ram through a die to produce a long profile with reduced cross sectional area that may have complex geometries. The extrusion process is illustrated in Figure 2.2 [25, 26, 28].

AlMgSi-alloys have excellent extrudability due to the low alloying content and high melting point [23]. The rate of preheating is essential, as it is desirable to avoid further precipitation of Mg_2Si-particles and dissolve the Mg_2Si-particles that are already present. Dissolution of Mg_2Si-particles increase the amount of magnesium and silicon are made available for the formation of hardening phases during ageing. AlFeSi dispersoid number density decrease with increasing preheating temperature. These dispersoids are of importance as they may act as heterogeneous nucleation sites during ageing for MgSi-phases during cooling [28]. The cooling rate after extrusion is another important parameter, especially if no solution heat treatment (SHT) is performed subsequently. The cooling system may consist of air-cooling, water-cooling or a combination of the two. Choice of cooling system is dependent on the cooling rate that is adequate to maintain a proper age-hardening response, which will depend on the alloy composition and geometry of the extruded profile [15].

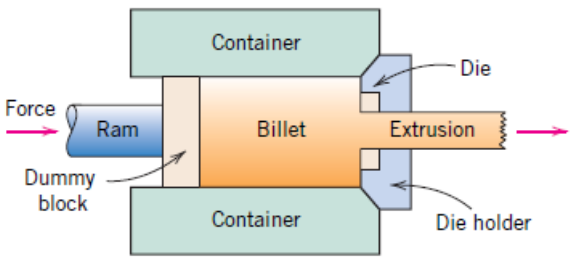

Figure 2.2: Illustration of the extrusion process. Reproduced from [25]

2.2.4 Pre-Deformation

A rapid quench may cause distortion and induce internal stresses of the extrudate. Therefore, it generally needs straightening by stretching due to geometrical changes that may occur during cooling. The amount of stretching may be adjusted based on the products size, shape, critical dimensions and surface finish, and is often between 1% and 3% elongation. If the extruded profile is solution heat treated after extrusion, the pre-deformation is generally performed subsequent to the SHT [8, 15].

2.2.5 Ageing

Age hardening of AlMgSi-alloys are performed in three steps. First, a solution heat treatment to bring solute atoms into a single phase solid solution. Following, a quench is performed to produce a SSSS by avoiding diffusion of solute atoms and formation of precipitates. Finally, the temperature is raised to induce precipitation of hardening phases, which is called artificial ageing [8, 25]. Ageing happening at room temperature is called natural ageing. It may take place due to logistical reasons during processing or forming operations before artificial ageing. For AlMgSi-alloys, natural ageing has a negative effect on the hardening response during artificial ageing [23]. Age hardening will be further discussed in Section 2.3.

2.3 Age-Hardening

Theory related to age-hardening was presented in the specialisation project, and parts of the following sub-chapters contain amended theory presented in the specialisation project together with additional relevant theory [22].

Proper heat treatment of extruded AlMgSi-alloys is essential to obtain the desired mechanical strength and corrosion properties. The three stages of age hardening are SHT, quenching and ageing [8, 25]. Proper age-hardening is of great importance as the mechanical and physical properties depend on amount of solutes in solid solution, specific atomic arrangements and size and dispersion of precipitates [18]. The process is illustrated in Figure 2.3. Step one is SHT, where a complete solid solution is produced. The second step is to quench, where the goal is to avoid precipitation to produce a SSSS. Step three is ageing at elevated temperature, which is performed to induce precipitation of hardening phases in a desirable matter. The precipitation sequence during artificial ageing will be discussed in Section 2.3.4. As stretching often is performed subsequent to quenching, it is included here as a step in the age-hardening procedure [8, 25].

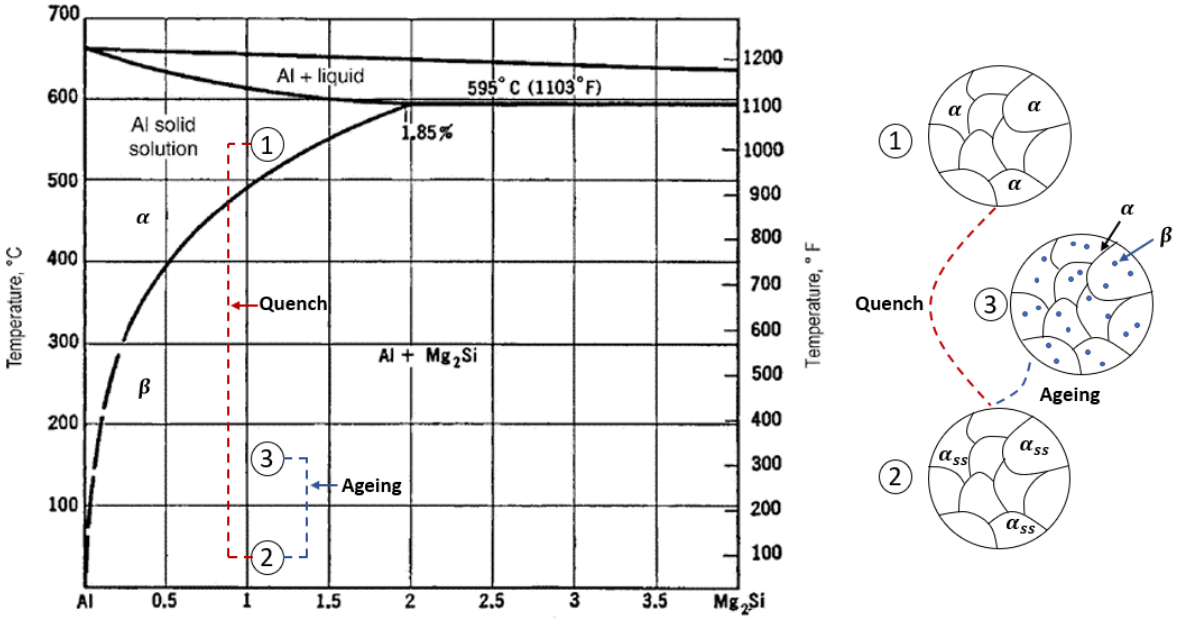

Figure 2.3: Quasi-binary section of Al-Mg_2Si for AlMgSi-alloys, and illustration of microstructure achieved during precipitation hardening. Adapted from [33, 34].

2.3.1 Solution Heat Treatment

The goal of SHT is to produce complete solubility of most of the alloying elements, so the temperature is raised to a temperature within a single phase, equilibrium solid solution [8]. During SHT of AlMgSi-alloys, the temperature is usually raised to 500-580 °C, close to the eutectic temperature. This temperature is kept for a time such that existing precipitates are dissolved. Dissolution of existing precipitates is important for maximising the amount of solute available for precipitation of desired precipitates and that a non-uniform distribution is produced during ageing. The cooling rate from SHT will determine whether solute remains in solid solution or if precipitation takes place [26].

2.3.2 Quench

The cooling rate after SHT has a considerable effect on the mechanical and corrosion properties of age-hardenable aluminium alloys [35]. Quenching aims to attain maximum supersaturation of alloying elements, which is obtained by a sufficiently high cooling rate [8]. Quench sensitivity is a measure of how easy an alloy retains all hardening solute elements in solid solution, and it is dependent on the content of alloying elements. Reducing the level of supersaturation will affect the hardening response during ageing since less solute is available for the formation of hardening phases [8, 36, 37, 38]. The number of eutectic AlFeMnSi-precipitates and dispersoids formed during casting and homogenisation also affect the quench sensitivity as these act as heterogeneous nucleation sites for MgSi-phases. Quench sensitivity has been found to be directly proportional to the dispersoid density. Reduced hardness because of precipitation on dispersoids of MgSi-containing precipitates, is caused by less solute magnesium and silicon available able to form hardening precipitates during artificial

ageing and that it leads to an inhomogeneous distribution of these precipitates [30, 31].

Atoms along a grain boundary are less regularly bonded than atoms of the matrix, which give rise to an interfacial energy. As the interaction between grain boundaries and solute atoms can reduce this interfacial energy, alloying elements can segregate to the grain boundaries [25, 39]. Quenching is related to non-equilibrium grain boundary segregation, which is a process based on the interaction between solute atoms and excess vacancies. Rapid cooling from SHT cause a supersaturation of vacancies. As grain boundaries act as vacancy sinks, a concentration gradient is produced between the matrix and the grain boundaries upon heating. Complexes are formed between vacancies and solute atoms, and because of the concentration gradient of vacancies, the solute atoms are dragged to the grain boundaries and are deposited. An enrichment of solute element on the scale of several nanometers can consequently form along the grain boundaries [39, 40]. The cooling rate will influence the number of quenched-in vacancies that are formed. Reducing the amount of quenched-in vacancies can suppress the clustering process of magnesium and silicon, which will also suppress the formation of hardening phases during artificial ageing [31, 41, 42].

Continuous cooling precipitation (CCP) diagrams describe precipitation behaviour after solution heat treatment depending on a continuous cooling rate. The slowest continuous cooling rate where no precipitation takes place is called the upper critical cooling rate (UCCR). The UCCR of a 6005A aluminium alloy determined by construction of a CCP-diagram have been reported to be 6.25 °C/s [37]. Further, a time-temperature-precipitation (TTP) diagram constructed for the same 6005A aluminium alloy, is shown in Figure 2.4 [43]. A TTP-diagram reveal information of about critical time and temperature ranges for precipitation during cooling from SHT. Three local time-minima are revealed by the C-curve, at 440 °C, 370 °C and 300 °C. The time-minima at 370 °C obtain 10% of the precipitate volume already after 25 seconds and is the most critical. The high-temperature precipitation is related to Mg_2Si, the medium-temperature precipitation is related to B′, and β' and the low-temperature precipitation is related to β'' [43].

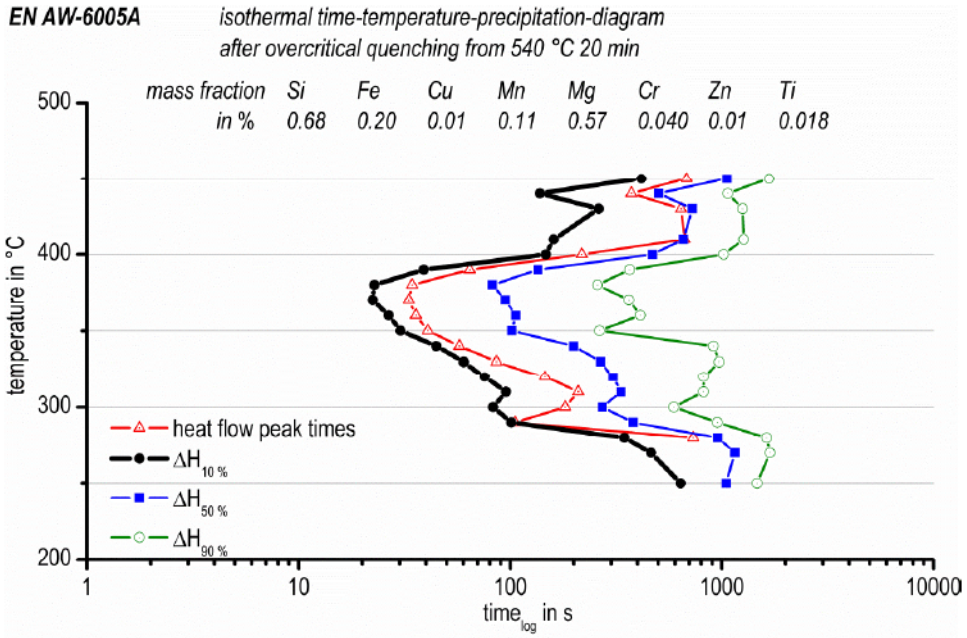

Figure 2.4: Isothermal time-temperature-precipitation diagram of a 6005A aluminium alloy. Reproduced from [43].

2.3.3 Pre-Deformation

As described in Section 2.2.4, profiles are usually straightened by stretching subsequent to the quench, which is classified as cold work. Cold work is deformation at a low temperature compared to the melting point of the material. Increased strength and hardness of a material by plastic deformation is called strain hardening. Upon plastic deformation, the dislocation density of the material increases and some of the deformation energy is stored in the material as strain energy associated with the dislocations. Cold work increases tensile strength, yield strength and hardness, while ductility, electrical conductivity and density decreases [25, 44]. Electrical conductivity of aluminium alloys is generally more affected by solutes in solid solution and thermal treatment than by strain hardening [18].

Effect on Precipitation

Dislocations are high diffusion paths, as atomic migration is much faster along dislocations than through the crystal lattice. For diffusion-controlled processes at relatively low temperatures, such as precipitation in metals, dislocation pipe diffusion can by the dominating transport mode [45]. Consequently, the formation of clusters may be altered and precipitation rates during artificial ageing are accelerated. Bulk diffusion coefficient of copper is one order of magnitude lower than those of silicon and magnesium, but in pipe diffusion, the diffusion coefficients of copper and silicon are of similar order. This was proposed as a reason for the suppressed formation of Si-Mg co-clusters and β''-precipitates [46]. Dislocations act as vacancy sinks which reduces the vacancy concentration in the matrix, and can suppress the formation of Guiniuer-Preston (GP)-zones that are nucleation sites for β''-precipitates. The reported effects

are that formation of β''-precipitates are replaced by post-β''-precipitates, such as β' and B′ [47, 48, 49, 50]. Precipitation of L- and Q′-phases is also enhanced by pre-deformation, where Q′-phase nucleates at dislocation lines [46, 50].

The main nucleation mechanism changes from homogeneous precipitation to heterogeneous precipitation on dislocations when pre-deformation is applied. Precipitates in pre-deformed variants are coarser than in undeformed materials, which is due to the increased atomic diffusion and increased precipitation kinetics [47, 49]. Dislocations increase the fraction of disorder precipitates, which increase the amount of copper that they can incorporate [13, 48, 51]. Heat treatment may remove the effect of strain hardening. Recovery is the phenomenon when some of the internal stress is relieved by dislocation movement upon heating by increased atomic diffusion. The dislocation density is reduced by annihilation and dislocation rearrangement into lower-energy configurations, which forms dislocation cells. The dislocation cells that may transition into sub-grains with low angle grain boundaries (LAGBs) [25, 52]. Still, heterogeneous precipitation on dislocation lines can take place, as precipitates on dislocation lines have been observed after only 10 minutes of artificial ageing at 190 °C [48].

The effect of pre-deformation on precipitation is illustrated in Figure 2.5. Figure 2.5(a) illustrates the grain boundary region in the undeformed and artificially aged condition, where a solute-enriched film has formed on the grain boundary and clustering has taken place in the matrix. The pre-deformed and artificially aged condition is illustrated in Figure 2.5(b). There is no solute-enriched film on the grain boundary and no clustering of solutes in the matrix, instead, nucleation is heterogeneously taking place at dislocations [16].

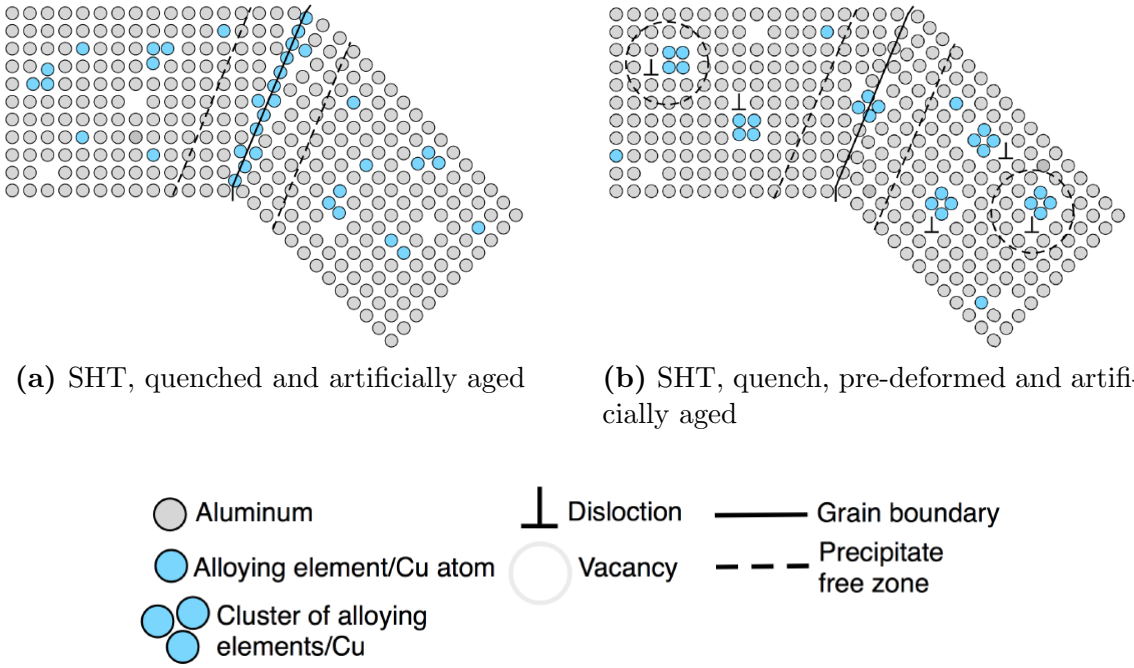

(a) SHT, quenched and artificially aged

(b) SHT, quench, pre-deformed and artificially aged

Figure 2.5: Illustration of vacancies, dislocations and clustering of undeformed and pre-deformed alloys before and after ageing. Reproduced from [16].

Effect on Hardness

AlMgSi-alloys must obtain a desirable strength and hardness to be used in industries for structural applications. Hardness and strength of a material increases with increasing ability to resist plastic deformation. As plastic deformation occurs through movement of dislocations, strengthening mechanisms are based on hindrance or restriction of dislocation movement. The most prominent sources to strain hardening by cold work is lattice distortion and interaction stresses between dislocations. Dislocation-dislocation interactions are repulsive on average, causing a hindrance of dislocation movement [18, 25]. As pre-deformation suppress the formation of Mg-Si co-clusters and β''-precipitates and produce coarser precipitates during artificial ageing, the age-hardening response is lowered [47, 49]. The hardening mechanism will be a combination of strain hardening and precipitation hardening in pre-deformed and subsequently artificially aged AlMgSi-alloys. Hardness of pre-deformed and artificially aged variants of AlMgSi-alloys have been reported to obtain significant higher hardness than undeformed and artificially aged variants of the same alloy [49]. While it has also been reported that hardness is independent of the degree of pre-deformation, or that the obtained hardness have been reduced by pre-deformation. Lower obtained hardness of pre-deformed and artificially aged condition compared to undeformed and artificially aged condition, is proposed to be caused by overageing as a consequence of increased precipitation rate [16].

2.3.4 Artificial Ageing

The most effective strengthening mechanism in AlMgSi-alloys is precipitation hardening [23]. It is obtained by artificial ageing, which is controlled precipitation of fine particles at elevated temperature to obtain desired mechanical properties. Thermal energy is required as the nucleation and growth process of precipitates is diffusion dependent [6, 18].

Precipitation Sequence

The precipitation process in AlMgSi-alloys is complex and there is today still some uncertainties related to the mechanism. As the equilibrium phases typically are incoherent with the matrix, it causes a great energy barrier for nucleation. As a consequence, precipitation takes place in a sequence with coherent and semi-coherent metastable phases, before the transition into the equilibrium phase. The steps of the precipitation sequence may involve several metastable and stable phases, which is dependent on thermomechanical processing and composition of the alloy. A simplified, precipitation sequence in AlMgSi-alloys can be written as shown in Equation 2.1 [6, 23].

$$\text{SSSS} \rightarrow \text{soluteclusters} \rightarrow \text{GP-zones} \rightarrow \beta'' \rightarrow \beta', \text{B}' \rightarrow \beta, \text{Si} \tag{2.1}$$

A SSSS forms after quenching from the α-phase-field after SHT [23]. In quenched condition, separate magnesium- and silicon-clusters can be present. Upon natural ageing or heating these aggregate to form magnesium-silicon co-clusters. GP-zones are formed early upon heating, and have a spherical shape with similar chemical nature as the co-clusters. GP-zones can act as heterogeneous nucleation sites β''-phase

[8, 53]. β''-precipitates are coherent, monoclinic needles and are the main strengthening precipitates in AlMgSi-alloys [8]. They might take several compositions, and compositions of both Mg_5Si_6 and $Mg_5Al_2Si_4$ has been proposed [54, 55]. Prolonged ageing causes the transition from β''-phase to β'-phase, corresponding to the transition from peak ageing to overageing. β'-precipitates are rod-shaped, semi-coherent with the matrix and typically in the range of hundreds of nanometer [23, 56]. B′-phase forms as semi-coherent laths together with β'-phase and is favoured by high Si:Mg-ratios [8]. The equilibrium phase β, has the composition Mg_2Si and is incoherent with the matrix. If silicon is present in excess, it may also form a pure silicon equilibrium phase [23, 56, 57]. AlMgSi-alloys are commonly artificial aged to a state containing metastable phases, as the equilibrium phases are distributed too coarse to offer significant strengthening [23]. Figure 2.6 illustrates the evolution of strength with artificial ageing time and evolution of precipitates.

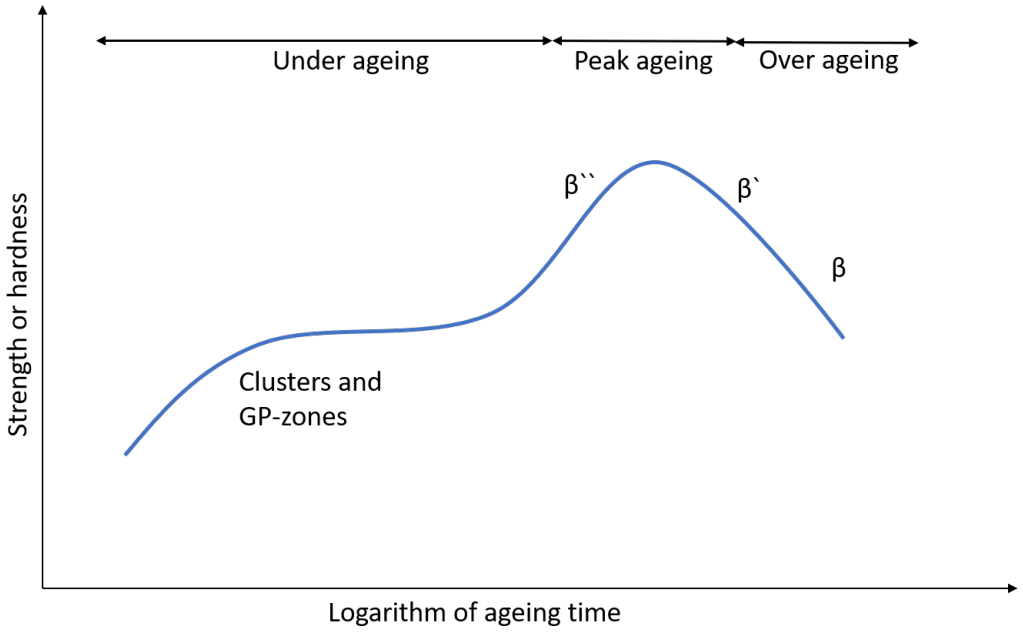

Figure 2.6: Sketch of strength or hardness as a function of time of artificial ageing. Adapted from [25], with additional information from [23, 56, 57].

Copper addition leads to finer microstructure and increased volume fraction of precipitates, and is therefore added to increase the hardness [17, 58]. Copper also alters the precipitation sequence in AlMgSi-alloys and different metastable- and equilibrium phases may form [23, 57, 59]. There are also still uncertainties related to the precipitation sequence of AlMgSi(Cu)-alloys, but a simplified sequence may be expressed as shown in Equation 2.2 [6, 23, 57],

$$\text{SSSS} \rightarrow \text{solute clusters} \rightarrow \text{GP} \rightarrow \beta'', \text{L}, \rightarrow \beta', \text{Q}' \rightarrow \beta, \text{Q}, S, \theta, \text{Si}. \tag{2.2}$$

Q is a quaternary equilibrium phase with a stoichiometry of $Al_3Cu_2Mg_9Si_7$ [6, 59]. Additionally equilibrium phases that may form depending on composition are θ-phase (Al_2Cu) and S-phase (Al_2CuMg) [6, 11]. When the Mg/Si-ratio is less than one, pure

silicon is stable, while for ratios larger than one β-phase is stable. Q- and θ-phase are stabilized with increasing amount of copper. Q′-phase is a metastable precursor to Q-phase and has the same crystal structure and lattice parameter as Q-phase, but it is semi-coherent with the matrix. L-phase is a metastable precursor to Q′-phase, and both L- and Q′-precipitates can contribute to strengthening [23, 57].

Hardening Mechanisms

The strength of age-hardened alloys depends on the interaction between precipitates and dislocations during dislocation movement. Both strain around GP-zones and precipitates, as well as the GP-zones and precipitates themselves, may cause hindrance to dislocation movement. This gives rise to three modes of hardening; coherency strain hardening, chemical hardening and dispersion hardening [44].

Coherency strain hardening is most dominant in the underaged condition and is caused by GP-zones or precipitates that have a slight misfit in the matrix producing stress fields acting as obstacles for dislocation movement. The applied stress must be equal to or greater than the average internal stress for a dislocation to move through the stress field [8, 23, 44]. The interaction between a dislocation line and the stress fields around coherent particles is illustrated in Figure 2.7 [44].

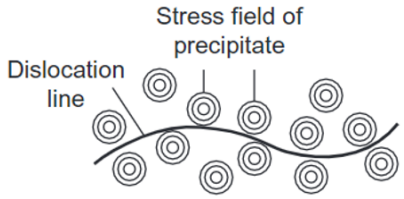

Figure 2.7: Illustration of coherency strain hardening mechanism. Reproduced from [44].

Chemical hardening occurs when a dislocation cuts through a precipitate or GP-zone, as shown in Figure 2.8. This provides a short-range interaction between dislocation and precipitate or cluster. During shearing of the GP-zone or precipitate, the number of neighbouring solvent to solute molecules will change along the slip plane, and the clustering process may consequently be somewhat reversed. Strengthening contribution may arise from the energy required to create a new interface between particle and the energy related required to form an anti-phase boundary (APB) inside the precipitate or GP-zone [8, 44].

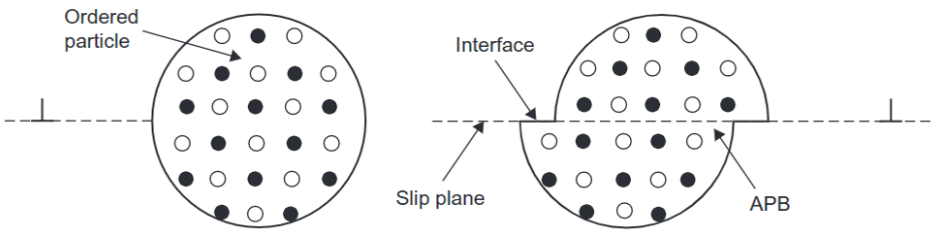

Figure 2.8: Illustration of chemical hardening mechanism, where a dislocation cuts through an ordered particle. APB = anti-phase boundary. Reproduced from [44].

Dispersion hardening occurs when the dislocation moves around or over widely spaced, large precipitates. The precipitate is not deformed with the matrix, and stress is sufficient to form a loop of dislocation around precipitates. This hardening mode takes place in overaged condition, when particles are incoherent and misfit strains are limited. As the distance between the precipitates increases the yield stress decreases. The majority of the strengthening will be from the debris of dislocation surrounding the precipitates. An illustration of dispersion hardening is shown in Figure 2.9 [8, 44].

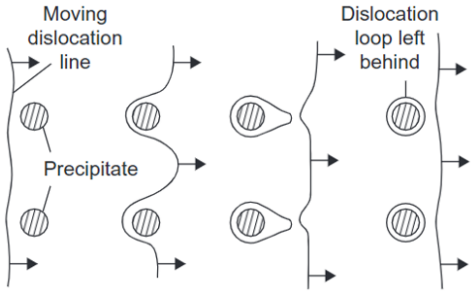

Figure 2.9: Illustration of dispersion hardening mechanism, where dislocations form loops around the precipitates. Reproduced from [44].

2.4 Intergranular Corrosion of AlMgSi-Alloys

The IGC susceptibility of AlMgSi-alloys was studied during the specialization project. Theory presented in the following sub-chapters is somewhat amended from specialization project together with additional relevant literature [22].

Intergranular corrosion (IGC) is a selective attack of the grain boundary region, without a significant attack of the grains themselves [12, 60]. As elaborated in Section 2.3.2, solute elements diffuse to grain boundaries during artificial ageing subsequent to quenching and can cause precipitation and formation of a solute-enriched film along the grain boundaries [39]. A microgalvanic coupling between the enriched grain boundary and the PFZ causes IGC [9, 61]. Depending on thermomechanical processing and composition of the alloy, IGC susceptibility of AlMgSi-alloys is generally related to either copper-enriched noble film or precipitates on the grain boundary or anodic precipitates at the grain boundaries [9, 11, 62]. IGC penetrates quicker than pitting but may reach a self-limiting depth as transportation of oxygen and corrosion species down IGC filament is limited. When the depth of the attack reaches a maximum, the attack spreads laterally across the surface [60, 63].

2.4.1 IGC Mechanism of AlMgSi(Cu)-Alloys

IGC in AlMgSi-alloys may take place through selective dissolution of the PFZ which is anodic with respect to nobler grain boundary film or precipitates. It may also proceed through selective dissolution of grain boundary precipitate that is anodic with respect to the PFZ. Which mechanism that takes place will depend on the composition of the alloy, such as copper-content and the magnesium to silicon ratio, and consequently the grain boundary structure [11, 62, 64].

The IGC mechanism of AlMgSi-alloys containing copper is illustrated in Figure 2.10 [65]. IGC susceptibility induced by copper content is related to a copper enriched film along grain boundaries which may form depending on the thermomechanical treatment. After the artificial ageing, where solute elements have segregated to the grain boundaries, a PFZ adjacent to the grain boundary is formed. A microgalvanic coupling between the noble copper enriched film and Q-phase particles and the active PFZ, causing preferential dissolution of the PFZ [9, 10, 61, 66, 67]. Kumari investigated the initiation of IGC in AlMgSi(Cu)-alloys, and suggested that the initial external cathode is α-phase and the internal cathode is the copper enriched film at the grain boundaries. Q-phase particles were passive with respect to α-phase particles, and acts initially as barriers towards IGC propagation. As α-phase corrodes and copper is enriched at corroding sites, copper will become the dominating electrode both internally and externally. Lower pH in IGC filaments than in the bulk solution was indicated by a difference in etching morphology on the surface compared with IGC filaments. Which can only occur by the participation of an external cathode, satisfying the principle of localized corrosion by the separated anode and cathode [65].

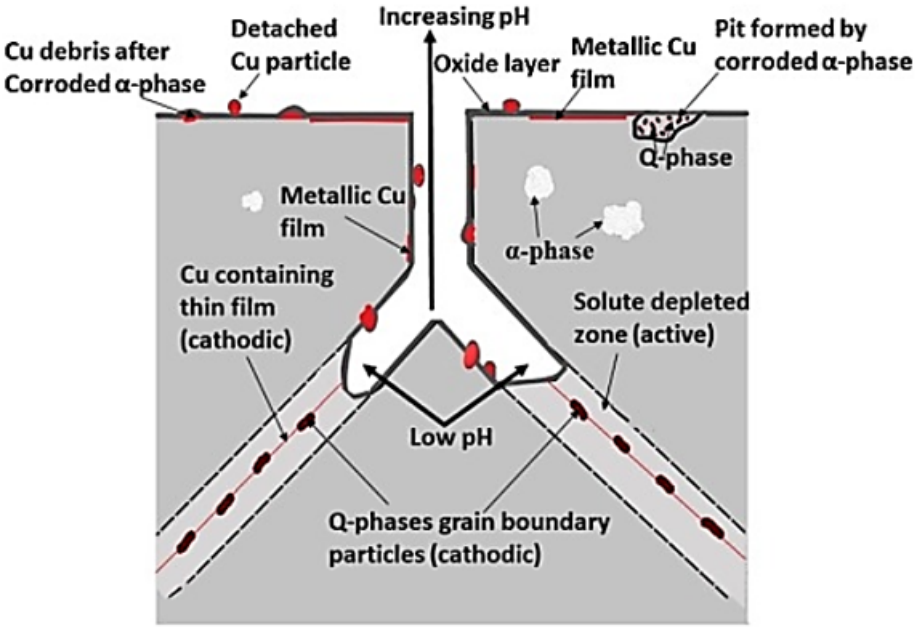

Figure 2.10: Illustration of the IGC mechanism of AlMgSi(Cu)-alloys in acidic solution. Reproduced from [68].

2.4.2 Effect of Alloying Elements

Amount of alloying elements present in AlMgSi-alloys affect the susceptibility to IGC. As presented in Section 2.3.4, many different phases may form in the grain boundary region, each having different corrosion potential which will affect the susceptibility to IGC [11]. Corrosion potentials in 0.1 M NaCl of phases in AlMgSi(Cu)-alloys are given in Table 2.2. As mentioned in Section 2.4.1, copper plays a significant part

in the IGC mechanism in alloys containing copper. Silicon present in excess of the stoichiometric Mg/Si-ratio of β-phase may increase IGC susceptibility as silicon may segregate to grain boundaries leaving an active depleted zone adjacent to the grain boundaries [57, 64, 69]. Iron is present as an impurity, and form intermetallic phases that are important during initiation of IGC [65]. The effect of copper- and zinc-content on IGC susceptibility of AlMgSi-alloys will be further discussed in the coming sub-chapters.

Table 2.2: Corrosion potentials in 0.1 M NaCl of phases in AlMgSi(Cu)-alloys [11].

Phase	Avg. Corr. Pot. [V_{SCE}]	Electrochemical behavior wrt. PFZ
Cu(99.9%)	-0.232 [70]	Cathodic
Si(99.9995%)	-0.441 [70]	Cathodic
Q($Al_3Cu_2Mg_8Si_6$)	-0.507 [71]	Cathodic
θ(Al_2Cu)	-0.627 [71]	Cathodic
PFZ(99.9999%Al)	-0.823 [70]	-
S(Al_2CuMg)	-0.883 [72]	Anodic
β(Mg_2Si)	-1.538 [72]	Anodic

Effect of Copper

Copper is added to AlMgSi-alloys for increased strength, however, it has an unfavourable effect on the corrosion resistance [7]. As described in Section 2.4.1, IGC of copper-containing AlMgSi-alloys are related to a copper enriched film at the grain boundaries and copper-containing grain boundary precipitates [9]. AlMgSi-alloys with a copper content down to 0.12 wt%, have been reported to be susceptible to IGC [10]. Variation in copper content has shown to have a more significant effect on the IGC susceptibility than the variation in Mg:Si-ratio for copper-containing alloys [62, 64].

Reducing the amount of copper on grain boundaries have shown to increase IGC resistance. Increased artificial ageing temperature, pre-deformation and slower cooling rate after SHT increase the amount of copper absorbed in precipitates. As more copper is incorporate into precipitates, copper is depleted from the matrix which leaves less copper available for formation of a copper-enriched film on the grain boundary [13]. Prolonged artificial ageing may lead to a coarsened and discontinuous copper-enriched film at the grain boundary, which improves the IGC resistance [61].

During the specialisation project the effect of copper on IGC susceptibility in a 6005 aluminium alloy was investigated. The results supported the reports stating that increasing the amount of copper increases IGC susceptibility. Samples that contained the largest amount of copper showed an increased maximum depth of IGC attacks, as well as the largest weight loss after being immersed in an acidified chlorine solution for 24 hours [22].

Effect of Zinc

Zinc has very high solubility in aluminium and can accumulate during recycling of aluminium alloys. It is, therefore, essential to investigate threshold values of zinc-

content that may lead to unfavourable effects on mechanical properties and corrosion behaviour [18, 19].

Early investigations indicated that zinc had a positive effect on the IGC resistance of AlMgSi-alloys. Zinc addition to AlMgSi-alloys where IGC may occur due to selective dissolution of Mg_2Si was proposed by Yamaguchi and Tohma to decrease the IGC susceptibility due to a reduction in electrochemical potential difference [73]. However, more recent studies indicate have reported a negative effect of zinc on IGC resistance. A zinc-content of 1 wt% in an AlMgSi-alloy have shown to develop an enrichment of zinc at the grain boundaries after heat treatment, increasing the susceptibility to IGC [19]. Stoknes studied zinc enrichment on the grain boundary further and whether it could exhibit a similar effect as a magnesium-enriched film which had shown to reduce IGC susceptibility [20, 40]. Though the results showed that a zinc content above 0.2 wt% increased the susceptibility to IGC, while below this value it did not affect IGC susceptibility [20]. The negative effect of zinc on IGC susceptibility was confirmed by the work of Lam, who proposed that the electrochemical potential difference between grain boundary and PFZ increased as zinc is more active than aluminium [21]. The addition of zinc up to 0.05 wt% in the 6005 aluminium alloy studied in the specialisation project did not have any effect on the IGC susceptibility [22].

2.4.3 Effect of Microstructure

Grain Size and Structure

Extruded 6005 aluminium alloys have been reported to have a four-layered structure, as shown in Figure 2.11 [65]. The first layer consist of small grains elongated perpendicular to the surface. The grains in the second layer are also elongated in the same direction as in the first layer but are larger than the grains in the first layer. In the third layer, the grains are large and elongated parallel to the surface and the extruded direction. The fourth layer, corresponding to the bulk, consist of small and randomly oriented grains [65, 74]. A similar layered structure was observed in the specialisation project [22]. Propagation of IGC filament is fastest along the grains in the two uppermost layers as these have grain boundaries perpendicular to the surface. As the filaments reach the third layer, the attack spreads laterally as these grain are elongated parallel to the surface. Propagation into the fourth layer was limited as the smaller grains of the bulk led to a more tortuous path along grain boundaries compared with the more straight grain boundaries of the three uppermost layers [65]. The results of the IGC test in the specialisation project confirmed that the IGC attack was in general limited to the three uppermost layers [22].

Grain Boundary Misorientation

Minoda and Yoshida studied the correlation between grain boundary misorientation and IGC susceptibility of a 6061 aluminium alloy at peak hardness. They reported that at high angle grain boundaries (HAGBs) close to the surface of the sample PFZs were formed, while at LAGBs in the centre rarely formed PFZs. The IGC attacks occurred more easily at HAGBs than at LAGBs, since PFZs and grain boundary precipitated

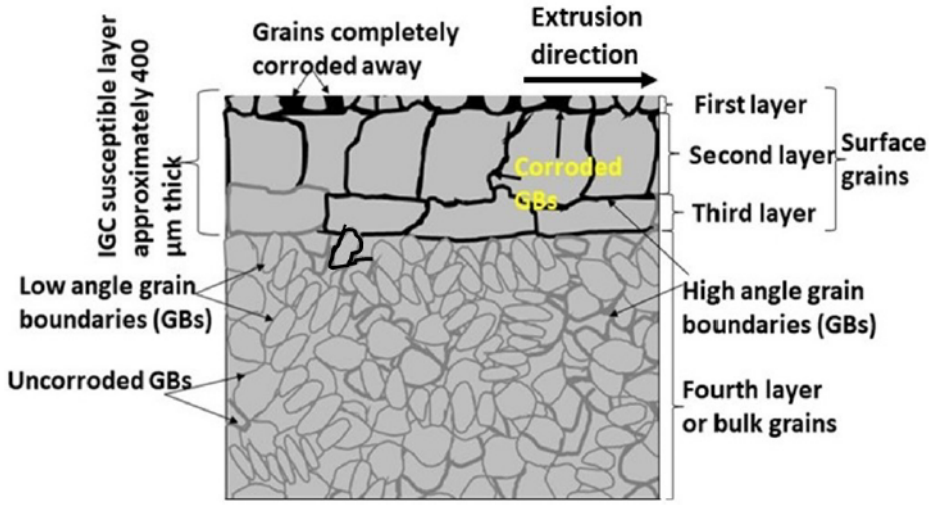

Figure 2.11: Illustration of the layered structure of extruded 6005 aluminium alloys. Low angle - and high angle grain boundaries are indicates, as well as typical IGC attacks. Reproduced from [65].

more regularly form at HAGBs [75]. Similar effects have been reported during investigations of IGC susceptibility of 6005 aluminium alloys. Higher susceptibility to IGC in HAGBs than LAGBS was proposed to be due to enhanced segregation of copper to form an enriched film in the surface near HAGBs than in LAGBs of the bulk [65, 74]. Figure 2.11, illustrates typical IGC attacks in the surface layer dominated by HAGBs [65].

2.4.4 Effect of Thermomechanical Processing

Effect of Cooling Rate After SHT

The cooling rate after SHT greatly affects the development of grain boundary structure and formation of precipitates, as was described in Section 2.3.2. Since the IGC mechanism is dependent on the electrochemical potential difference between different features of the microstructure in the grain boundary region, the IGC resistance of the alloy will depend on the cooling rate after SHT [9, 13, 14].

Svenningsen et al. studied the effect of thermomechanical processing in IGC susceptibility of AlMgSi(Cu)-alloys. Among the reported results, was that the cooling rate after SHT greatly affects the IGC susceptibility. Air cooling after SHT produced samples susceptible to IGC in naturally aged condition, while artificial ageing induced resistance and at peak hardness, IGC was eliminated. The increased resistance to IGC was proposed to be due to coarsening of copper-containing grain boundary precipitates precipitates, leading to a discontinuity of the copper-enriched film at the grain boundary. Water-quenched samples did not experience the same trend, as these were resistant to IGC at natural aged condition and artificial ageing induced susceptibility to IGC [9, 61, 66]. Lower cooling rates produces less copper-rich precipitates at the grain boundaries and a wider PFZ as compared with a higher cooling rates [14]. Lowering the cooling rate from SHT can increase the amount of copper incorporated

into precipitates. Reduced cooling rate promotes nucleation of Q′-phase containing copper on dispersoids and will increase disorder in bulk β''. Increased disorder in precipitates increases the amount of copper absorbed into the precipitates, which reduces the amount of copper available for the formation of a copper enriched film and consequently improve the IGC resistance [13].

Effect of Pre-Deformation

As described in Section 2.3.3, cold work induce the formation of dislocations. The formation of dislocation affect precipitation and will, as a consequence, influence the susceptibility to IGC of AlMgSi-alloys [13, 16].

Dislocations cause disordering of precipitates which can increase the amount of copper incorporated in the precipitates. This reduces the amount of copper that is available for the formation of a copper-enriched film at the grain boundaries, and may consequently reduce the susceptibility to IGC [13, 16]. Pre-deformation can cause a transition in corrosion mode from IGC to pitting corrosion by pre-deformation of water-quenched AlMgSi(Cu)-alloys, which can reduce both maximum penetration depth and weight loss experienced due to the IGC attack [16]. Transition of corrosion mode is attributed to dislocations accelerating precipitation rates, leading to coarsening of precipitates and a matrix more depleted from solutes. Consequently, the electrochemical potential difference between precipitate and the grain body increases, which increases the driving force for pitting corrosion similar to what has been observed for AlMgSi(Cu)-alloys in overaged conditions [16, 61].

Grønvold reported that pre-deformation affected the fraction between LAGBs and HAGBs. Pre-deformation led to a higher fraction of LAGBs, though it did not change the length of the HAGBs. The higher fraction of LAGBs may have contributed to the reported positive effect of reducing the severeness of IGC attacks of pre-deformed AlMgSi-alloys [16].

2.4.5 Testing for IGC Susceptibility

Resistance to IGC of heat treatable aluminium alloys can be tested by following the EN ISO 11846 standard. Results of this test are not absolute as the IGC resistance will differ with service environment, but can be used to rank susceptibility of alloys of different temper or compositions [76]. The test is reliable when investigation IGC susceptibility when understanding that it is highly accelerated compared with typical service environment. Materials that are resistant to IGC during the test are likely to be resistant also in normal operating environment. Further, the test has been found valuable for investigating the fundamental mechanisms of IGC and other corrosion modes [9, 10]. Samples of extruded AlMgSi-alloys that were resistant to IGC on the surface but experienced corrosion attacks on the edges during this test, can become susceptible to IGC when the edges are covered [21].

2.5 Pitting Corrosion

Pitting is very localized corrosion attacks that form small holes, were the surface diameter is usually less than or equal to the depth of the pit. It can be difficult to discover as the pits are small, can be covered in corrosion products and the overall weight loss is very little. Pitting may be difficult to predict and measure, as there may be differences in pit depths and number pits formed at equal conditions [12]. Pits generally initiate at a microscopic heterogeneity at the surface, which may be inclusions, solute depleted grain boundaries, dislocations or mechanical damages. The protective film is broken down by the accumulation of negatively charged anions, such as chloride. Pitting potential, E_{pit}, for a metal-electrolyte system is the threshold value of the anodic potential were pitting does not occur below this value but does occur above. Above E_{pit} catastrophic breakdown of the oxide film occurs and rapid pit propagation may take place [60, 77, 78]. Both pitting and IGC reduces the fatigue life of components, but IGC has a more unfavourable affect on the fatigue life as the sharper tips IGC filaments are greater stress riser than pits [60, 63].

2.5.1 Effect of Composition on Pitting Susceptibility

The pitting potential of aluminium does not differ significantly with many solute additions, but copper may shift the pitting potential in the noble direction. Still, aluminium alloys containing copper are reported to be least resistant to pitting corrosion. [60, 63]. Addition of copper reduce the size and increase the number density of precipitates formed in AlMgSi-alloys leading to a less defective interface between precipitate and aluminium matrix. A reduced the metastable pitting rate of AlMgSi-alloys with increased copper addition have been observed [79, 80]. Similar results have been reported in 2xxx- and 7xxx-aluminium alloy, where a critical size range of precipitates in which significantly changes the pitting susceptibility have been observed [81, 82, 83].

2.5.2 Effect of Thermomechanical Processing on Pitting Susceptibility

As described in the previous paragraph, the size of precipitates affects the pitting susceptibility of AlMgSi-alloys. Since precipitates coarsen with increases ageing time, the duration of artificial ageing can affect corrosion behaviour. Overageing lead to coarsening of matrix-and grain boundary precipitates that may act as cathodic initiation sites across the surface [61]. Further, growth of precipitates in the grain bodies due to overaging lead to depletion of solute in the matrix, which evens out the potential difference between grain and grain boundary. At the same time, the potential difference between the grain body and coarse precipitates increases. This results in an increased driving force of pitting corrosion [66, 84, 85]. Figure 2.12 illustrates how the grain boundary structure and corrosion mode changes with artificial ageing time. As described in Section 2.4.4, pre-deformation has shown to change the corrosion mode from intergranular to pitting-like corrosion. This transition is also proposed to take place because of coarsening of precipitates and depletion of solute atoms from the matrix, increasing the electrochemical potential difference between precipitate and matrix and consequently increasing the driving force for pitting corrosion [16].

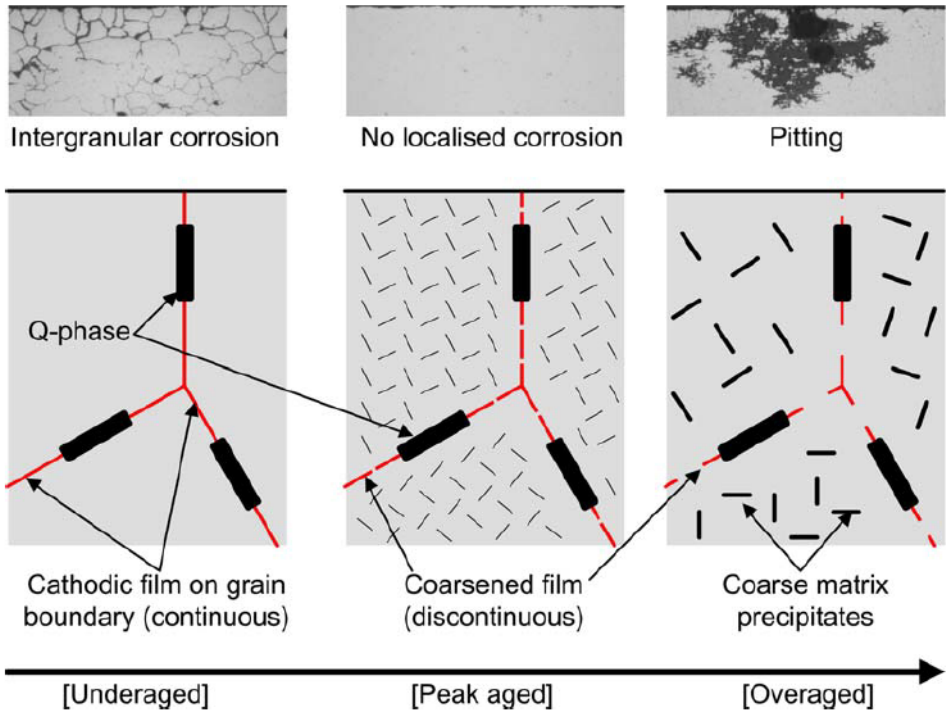

Figure 2.12: Illustration of correlation between artificial ageing, grain boundary structure and corrosion mode of AlMgSi(Cu)-alloys that were slowly cooled after SHT/extrusion. Reproduced from [61].

Chapter 3

Experimental

3.1 Materials

3.1.1 Composition

Six different variants of different copper- and zinc-content were used in this work. The composition of each variant, measured by optical emission spectroscopy, is given in Table 3.1. Amount of silicon, magnesium, iron and manganese were kept constant. The amount of copper was varied between 0.13 wt% and 0.17 wt%, while the amount of zinc was varied between 0.00 wt% and 0.05 wt%. The amount of copper and zinc denoted each compositional variant, for example, the variant containing 0.13 wt% copper and 0.00 wt% zinc was denoted as Cu13_Zn00.

Table 3.1: Composition of 6005.04 aluminium alloys measured by optical emission spectroscopy [wt%].

Alloy	Si	Mg	Fe	Mn	Cu	Zn	Al
Cu13_Zn00	0.6086	0.4827	0.2117	0.1535	0.1295	0.0027	Balance
Cu17_Zn00	0.6065	0.4822	0.2145	0.1519	0.1704	0.0027	Balance
Cu14_Zn02	0.6134	0.4925	0.2152	0.149	0.1423	0.0181	Balance
Cu15_Zn03	0.608	0.4814	0.2105	0.1548	0.1548	0.0319	Balance
Cu13_Zn05	0.6069	0.4871	0.2085	0.1443	0.1324	0.0506	Balance
Cu17_Zn05	0.6083	0.4823	0.2143	0.142	0.1722	0.0496	Balance

3.1.2 Processing of Received Materials

Casting of billets with a diameter of 95 mm was performed at the casting laboratory at Hydro RDS Sunndal by melt treatment and grain refining. The billets were homogenized at 575 °C for 2 hours and 15 minutes at the Reference Centre at Hydro RDS Sunndal. Extrusion of the billets were performed in a vertical extrusion press at SINTEF, Trondheim. The billets were preheated to 530 °C and the maximum temperature reached during extrusion was 560-570 °C. The ram moved at a speed of 5.6 mm/s and the die had dimensions of 4 x 25 mm^2. At the exit, the profiles were water-quenched and placed in a freezer for storage. The profiles were removed

from the freezer and kept approximately 24 hours at room temperature, before being artificially aged by a two-step process at 150 °C and 190 °C for a total of 6 hours. An illustration of the process as a function of time and temperature is illustrated in Figure 3.1. Further information about homogenisation, extrusion and artificial ageing of received materials are included in Appendix A.

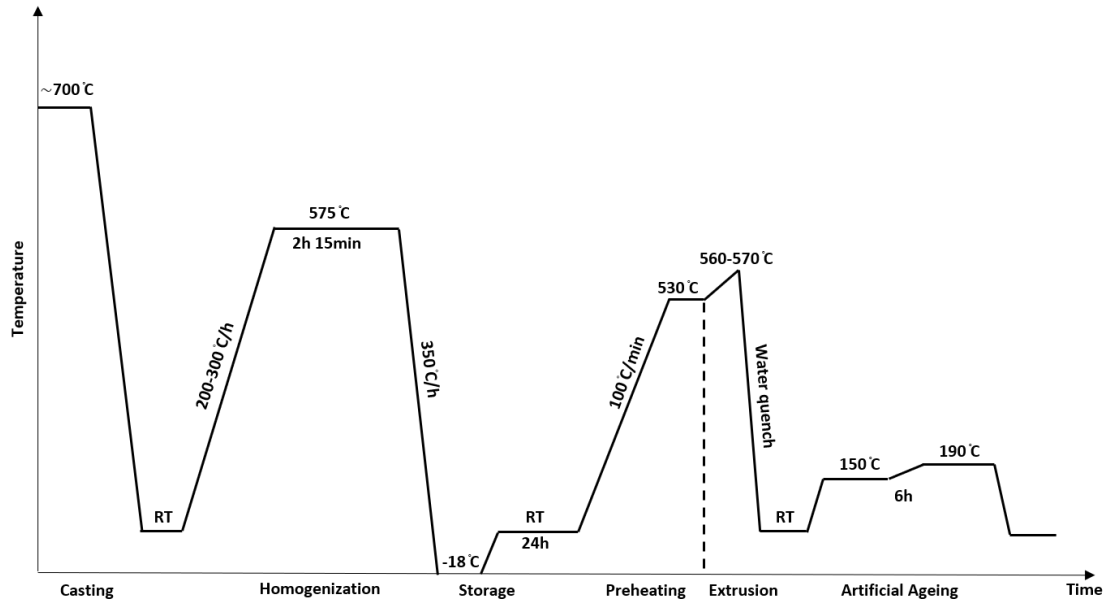

Figure 3.1: Illustration of the thermomechanical processing of the received materials as a function of temperature and time.

3.1.3 Additional Thermomechanical Treatment

To investigate the effect of cooling rate after SHT and the effect of pre-deformation on mechanical properties and IGC resistance, additional thermomechanical treatment was performed on the received materials. All the samples were solution heat treated at 540 °C for 30 min in a Nabertherm N15/65HA air circulation furnace. One sample of each variant of composition went through four different variants of processing routes, variating the cooling rate from SHT and whether pre-deformation was performed or not. Cooling from SHT was either performed by immersion in water holding room temperature or by taking the samples directly out of the furnace and placing on refractory material in room temperature. The cooling rate of air-cooling was measured by placing a thermocouple onto two different samples and recording the temperature every two seconds using datalogger Omega HH1384. Pre-deformation was performed by stretching to 5% elongation. The pre-deformation was performed by Pål Christian Skaret [1]. Finally, all the different variants were artificially aged at 185 °C for 5 hours in the same air circulating furnace. An overview of thermomechanical processing applied to the received materials are shown in Figure 3.2.

[1]Pål Christian Skaret, Department of Materials Science and Engineering, NTNU, Trondheim

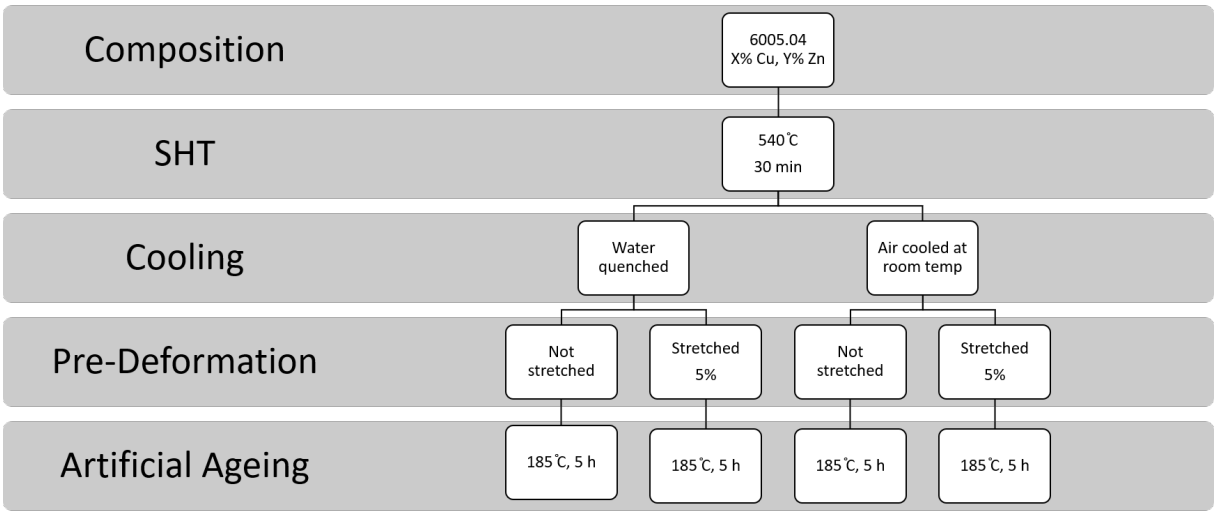

Figure 3.2: Overview of the additional thermomechanical treatment applied to the received materials.

The four different variants of processing route were denoted, as shown below:

- Samples that were water-quenched after SHT and not stretched prior to artificial ageing will be denoted as WQ_NS.
- Samples that were water-quenched after SHT and stretched prior to artificial ageing will be denoted as WQ_S.
- Samples that were air cooled after SHT and not stretched prior to artificial ageing will be denoted as AC_NS.
- Samples that were air cooled after SHT and stretched prior to artificial ageing will be denoted as AC_S.

The time-temperature relationship of additional thermomechanical treatment applied to the received materials is illustrated in Figure 3.3. Figure 3.3(a) illustrates the WQ_NS variation, which was water-quenched and stored in a freezer before artificial ageing. The WQ_S variant is illustrated in Figure 3.3(b), which was water-quenched and stored in a freezer. Pre-deformation was applied by stretching 5% and the total time in room temperature was approximately 1 hour before artificial ageing. Figure 3.3(c) illustrates time-temperature relationship of variant AC_NS. This variant was air cooled after SHT and stored in a freezer and artificially aged. The time-temperature relationship of variant AC_S is illustrated in Figure 3.3(d), which was air cooled after SHT and stored in a freezer. The samples of this variant were kept approximately 1 hour at room temperature while being stretched prior to artificial ageing.

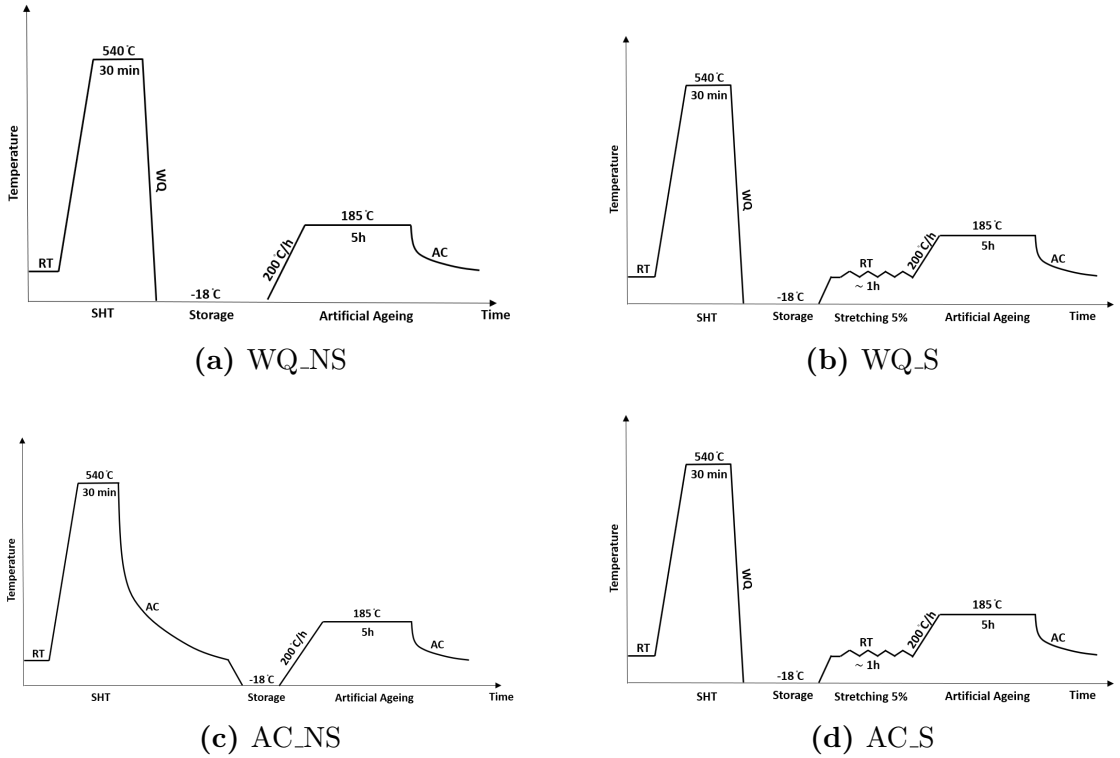

(a) WQ_NS **(b)** WQ_S

(c) AC_NS **(d)** AC_S

Figure 3.3: Temperature versus time profile for the four different variants of additional thermomechanical treatment applied to the received materials. (a) Illustrates WQ_NS variation, (b) illustrates WQ_S variation, (c) illustrates AC_NS variation and (d) illustrates AC_S variation. SHT = solution heat treatment, WQ = water quench, AC = air cooling.

3.2 Microstructural Characterization

3.2.1 Polarized Light Microscopy

Investigation with polarized light microscope was performed to investigate the microstructure of the samples. Samples for analysis in polarized light microscopy were made by cutting the profiles parallel to extruded direction, to dimensions of 15 mm x 15 mm x 4 mm, as shown in Figure 3.4. The samples were mounted in epoxy, and ground with SiC-grinding paper P320 using water as a lubricant. Further, the samples were polished using diamond pastes with particle sizes in the order of 9 μm, 3 μm and 1 μm, rinsing with water and ethanol between each polishing step. The final polishing step was vibration polishing for one hour using a Buehler Vibramet 2 with colloidal silica suspension, followed by rinsing in water and ethanol. The samples were anodized using a Struers Lectropol-5. The samples were exposed to fluoroboric acid (HBF_4, 5%) for 90 seconds while applying a voltage of 20 V. Lastly, the samples were rinsed in water and ethanol.

A Zeiss Axiovert 25 optical microscope with a sub-parallel λ-plate was used with polarized light to study the microstructure. The cross-section that was investigated was parallel to the extruded direction, as illustrated in Figure 3.4.

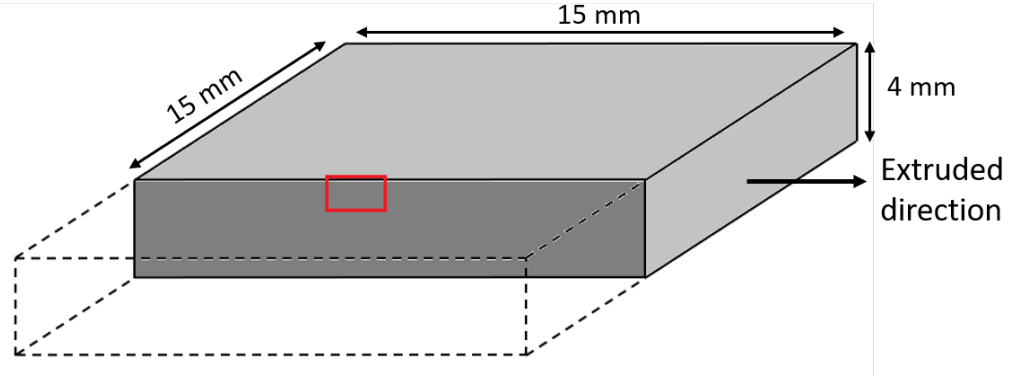

Figure 3.4: Illustration of the samples used for analysis using polarized light microscopy. The darker cross section is parallel to the extruded direction, and the red square illustrates the area seen with the microscope.

3.2.2 Electron Backscatter Diffraction

Electron backscatter diffraction (EBSD) analysis was performed to study the microstructure close to the surface and grain boundary misorientation. The samples were prepared in the same manner as described in Section 3.2.1, except anodizing, which was not performed. Instead, the polished samples were immersed in liquid nitrogen to remove the epoxy from the sample and stored overnight at 60 °C. A Low Vacuum Field Emission SEM Zeiss Supra 55 VP and a Nordif detector were used for the analysis. An accelerating voltage of 20 keV, the approximate working distance of 23 mm, aperture diameter of 120 μm, 70° angle tilt were the operating conditions used. To analyze the diffraction patterns, OIM Data Analysis was used.

3.2.3 Transmission Electron Microscope

Analysis in a transmission electron microscope (TEM) was performed to obtain information about the concentration of solute elements at grain boundaries, the thickness of PFZ and grain boundary precipitates.

The samples preparation was performed by Birgitte Karlsen[2]. Samples were prepared by cutting the profiles into two halves parallel to the transverse direction. One of the halves was ground with SiC-grinding paper from the interior side towards to surface until a thickness of approximate 100 μm was reached. Disks of 3 mm diameter were punched out from the foil. Electropolishing was performed using an electrolyte of 1/3 nitric acid (HNO_3) and 2/3 methanol (CH_3OH). The temperature was kept between -20 °C and -30 °C and a potential of 30 V was applied.

Analysis in TEM was performed by Calin D. Marioara[3]. The variants chosen for TEM analysis were Cu17_Zn05_WQ_NS and Cu17_Zn05_AC_NS. Two grain boundaries for each variant were the chosen areas for investigation. Energy-dispersive X-ray spectroscopy (EDS) mapping was performed by scanning TEM angular dark field an-

[2]SINTEF Industry, Metal Production and Processing
[3]SINTEF Industry, Materials and Nanotechnology

alytical mode using a Jeol 2100F TEM operated at 200 kV with 1.5 nm spot size. The EDS maps were obtained by INCA software from Oxford Instruments.

3.3 Electrical Conductivity Test

Electrical conductivity was measured as it can indicate the amount of alloying elements that are in solid solution [18, 86]. The conductivity was measured on the top surface of the profile, and no sample preparation was done in advance. A Sigmatest 2.069 was used to perform the measurements. Five parallels of each sample were measured.

3.4 Hardness Test

Vickers hardness measurements were performed to investigate the influence of processing route and content of copper and zinc on hardness. Samples were made by cutting the profiles parallel to the extruded direction. They were mounted in epoxy and ground with SiC-grinding paper in the order P320, P500, P800, P1200 and P2400 with water as a lubricant. Vickers hardness measurements were performed using an Innovatest Micro Hardness Tester, applying a pressure of 1kg and 10 seconds dwell time. The Vickers hardness was measured on the cross-section parallel to the extruded direction, as shown in Figure 3.5. Five parallels of each sample were measured.

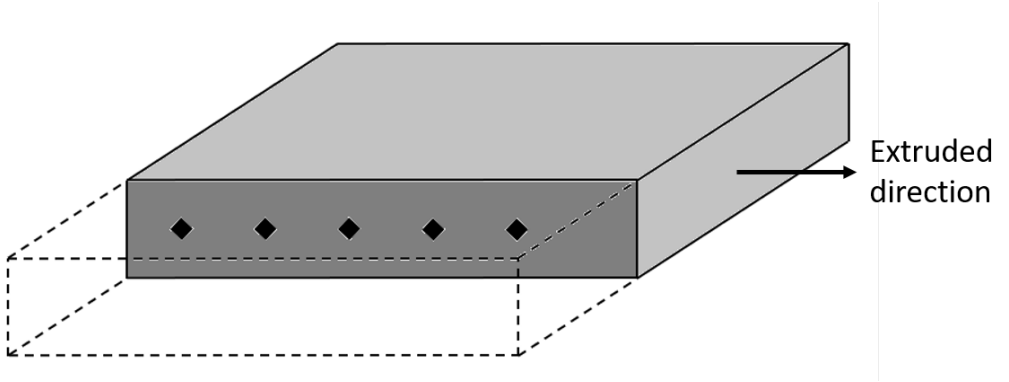

Figure 3.5: Illustration of the five indentations applied on the sample used for Vickers hardness measurement.

3.5 Accelerated Corrosion Test

Accelerated corrosion test was performed in accordance with the ISO standard 11846. The test is used to study and compare the susceptibility to IGC of solution heat-treatable aluminium alloys [76].

The acidified chlorine solution was prepared by mixing 10 ml concentrated hydrochloric acid (ρ = 1.19 g/ml) and 30 g NaCl per litre of solution. Samples were cut to dimension 20 mm x 25 mm, as shown in Figure 3.6(a). The standard specifies that the longer edge should be parallel to metal working direction, but due to dimensions of received material and amount of material available the samples were cut with the

short sides parallel to the extruded direction. Further, the samples were immersed in a sodium hydroxide solution (7.5%, 60 °) for 2.5 minutes. Desmutting was performed by immersing the samples in concentrated nitric acid (ρ = 1.4 g/ml), before being rinsed in distilled water and dried. The samples were tied in a fishing line and immersed in the acidified chlorine solution in a glass beaker. Two parallels of one variant composition and processing route were placed in the same beaker, with a ratio of 5 cm^3 solution per surface area of samples. After 24 hours of immersion, the samples were immersed in concentrated nitric acid (ρ = 1.4 g/ml) for two minutes to dissolve corrosion products. Finally, the samples were rinsed in tap water while brushed with a non-metallic brush, rinsed with distilled water and dried.

The samples were weighed before immersing in an acidified chlorine solution, and weighed after being immersed and rinsed of corrosion products. Measurement of pH of the acidified chlorine solution was performed before and after immersion of the samples, using a pH meter. The exposed samples were cut at an arbitrary location parallel to the extruded direction, ground with P320 SiC-grinding paper and polished using diamond pastes of 9 μm, 3 μm and 1 μm. The samples were rinsed with water and ethanol between each polishing step. Investigations of the darker cross-section illustrated in Figure 3.6(b) was performed by bright-field optical microscopy with a Zeiss Axiovert 25. The maximum corrosion depth was measured from a cross-section with a total length of 4 cm.

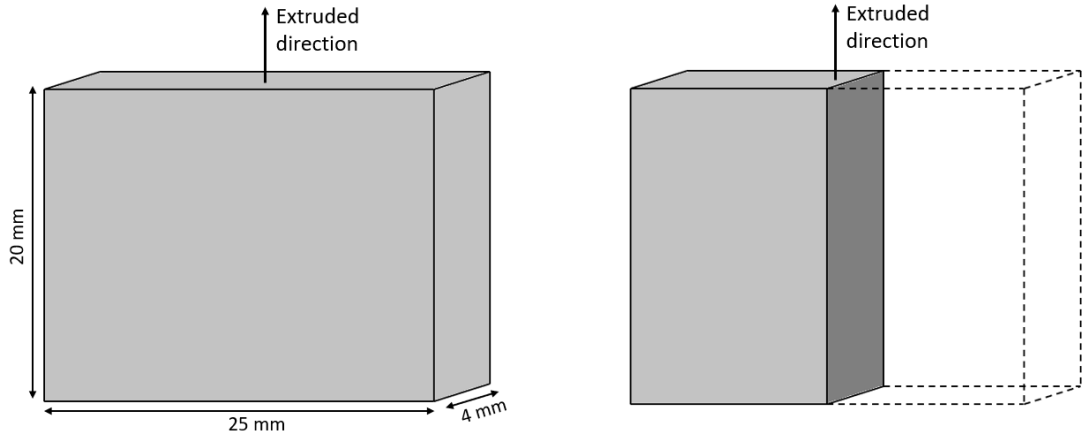

(a) Sample as immersed in acidified chlorine solution

(b) Exposed sample cut parallel to the extruded direction.

Figure 3.6: (a) Illustration of the dimensions of the samples used in accelerated corrosion test. (b) Illustration of the exposed samples used for examination in a bright-field optical microscope, where the darker cross-section is parallel to the extruded direction.

Chapter 4

Results

4.1 Air Cooling Rate

The temperature of a sample taken directly out of an air circulation furnace at 540 °C and into room temperature was measured every two seconds, to determine the cooling rate. This was performed twice, and the average cooling rate was calculated. The average measured cooling rate from 540 °C to 370 °C was approximately 9.5 °C/s. Figure 4.1 shows the average measured cooling rate plotted into the time-temperature-precipitation diagram constructed by Milkereit et al. [43]. The measured cooling rate did not cross the C-curves of the TTP-diagram but is close to touching the nose indicating 10% precipitation around 375 °C and 22 seconds. The complete temperature profile during cooling from SHT is included in Appendix B.1.

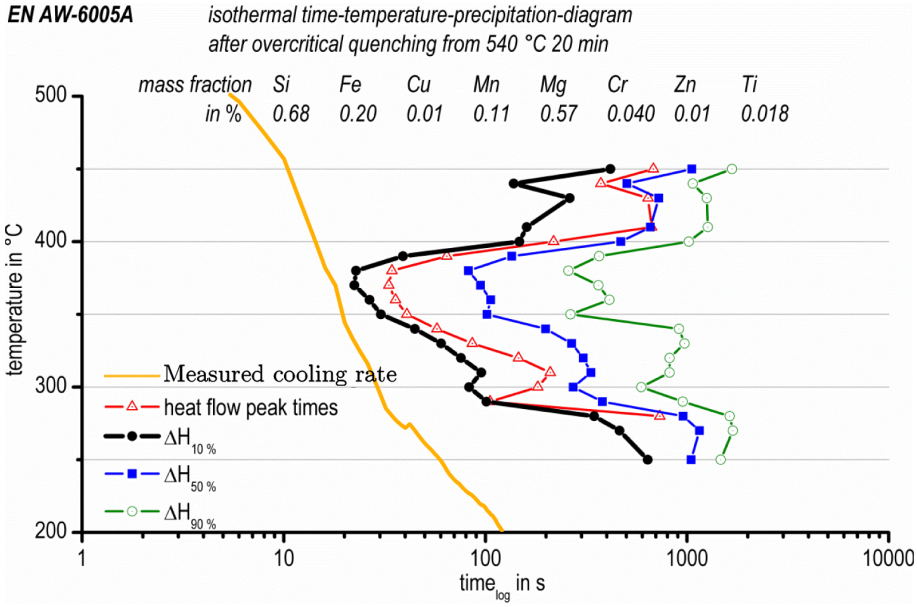

Figure 4.1: The average measured cooling rate plotted into the time-temperature-precipitation diagram constructed by Milkereit et al. for 6005A an aluminium alloy [43]. The mass fractions given in the TTP-diagram is of the alloy used for construction of the diagram and not for the alloy used in this work.

4.2 Microstructural Characterization

4.2.1 Polarized Light Micrographs

Polarized light micrographs of alloy Cu13_Zn00 of all four variants of processing route are shown in Figure 4.2. A layer of random texture was observed close to the surface in all micrographs. The microstructure seems to be fully recrystallized. No difference in microstructure can be observed from the micrographs between the different variants.

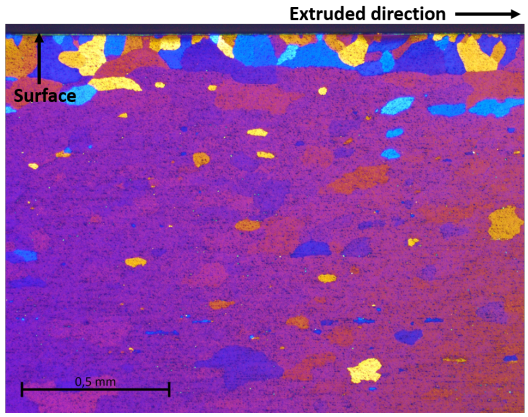

(a) Cu13_Zn00_AC_NS

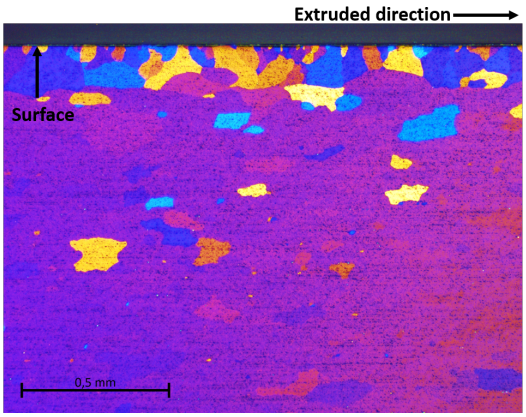

(b) Cu13_Zn00_WQ_NS

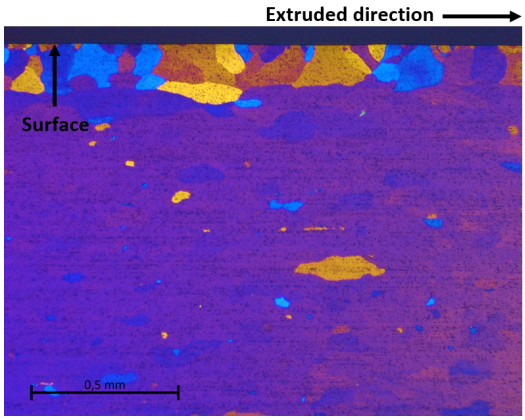

(c) Cu13_Zn00_AC_S

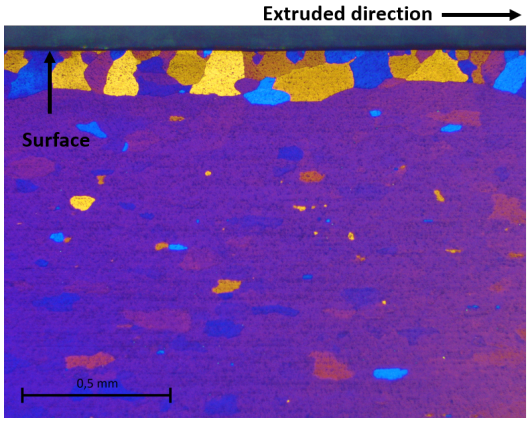

(d) Cu13_Zn00_WQ_S

Figure 4.2: Polarized light micrographs of a cross section parallel to the extruded direction close to the surface of alloy Cu13_Zn00 after different processing routes.

4.2.2 Electron Backscatter Diffraction

Electron Backscatter Diffraction was used to examine the grain structure and grain boundary misorientation angles. Figure 4.3 - 4.6 show the grain orientation maps (a) and grain boundary misorientation maps (b) of the area close to the surface parallel to the extruded direction of all variants of processing route. The compositional variant shown is Cu17_Zn13. A four-layered structure, similar to described by Kumari [65] and Danbolt [74], can be observed. The uppermost layer consists of very fine grains at the surface, while the second layer consists of larger grains with grain boundaries perpendicular to the surface. A third layer consist of large grains elongated parallel to the surface. The fourth layer corresponds to the bulk, and consist of a mixture of mostly equiaxed small grains and few larger equiaxed grains. Most of the surface near grain boundaries are HAGBs, while the bulk contains more LAGBs. All the variants have close to equal fractions of HAGBs and LAGBs.

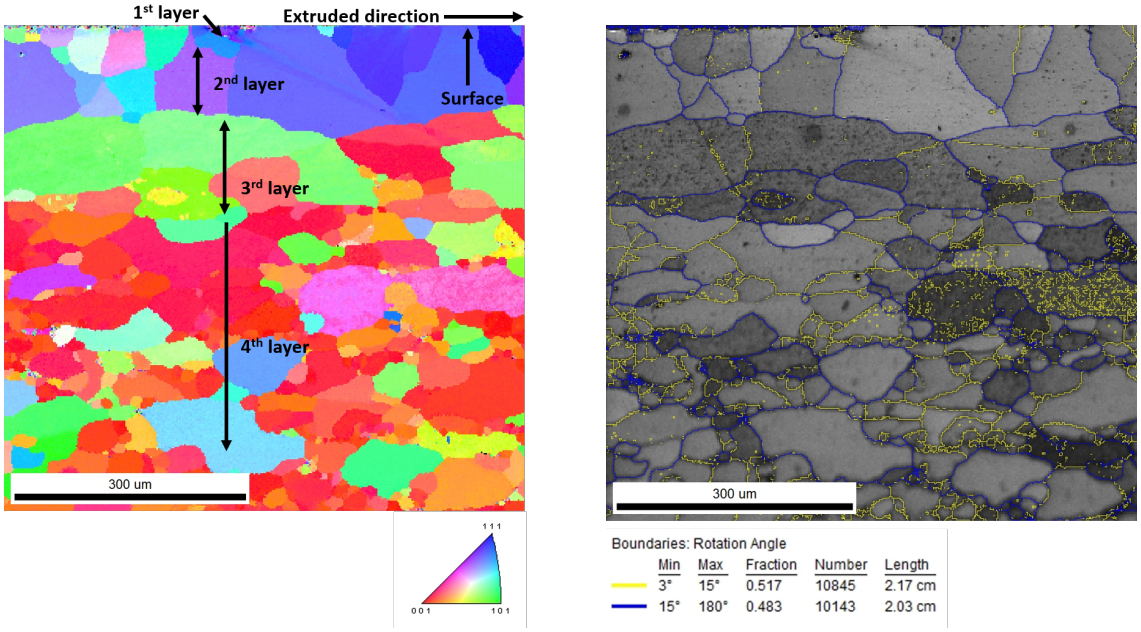

(a) Grain orientation map **(b)** Grain boundary misorientation map

Figure 4.3: Grain orientation map (a) and grain boundary misorientation map (b) of variant Cu17_Zn05_WQ_NS.

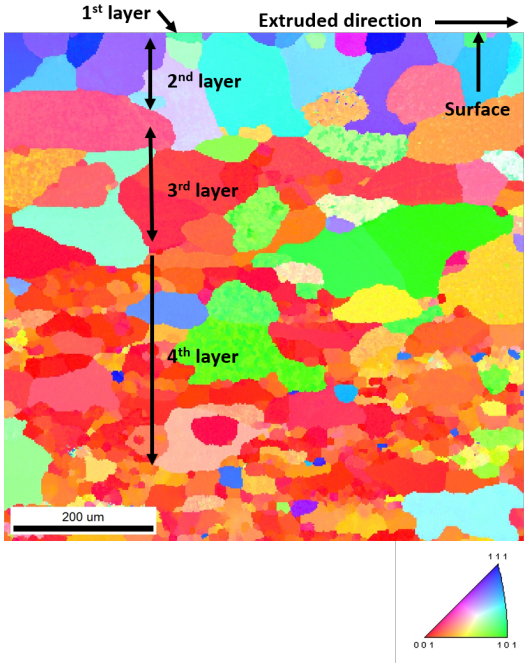

(a) Grain orientation map

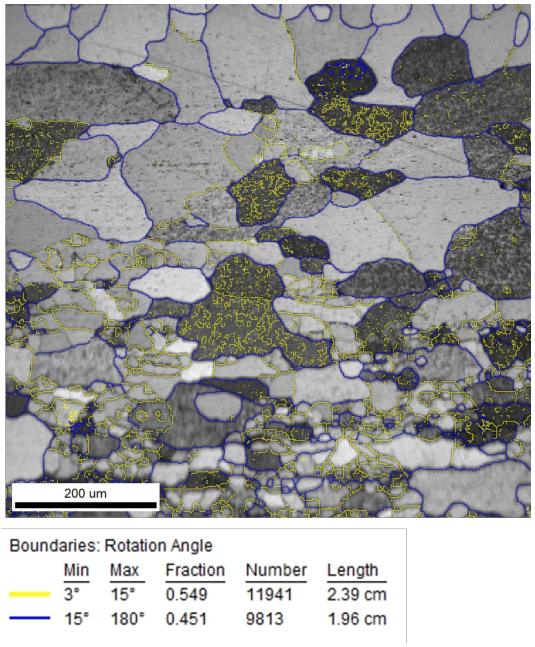

(b) Grain boundary misorientation map

Figure 4.4: Grain orientation map (a) and grain boundary misorientation map (b) of variant Cu17_Zn05_AC_NS.

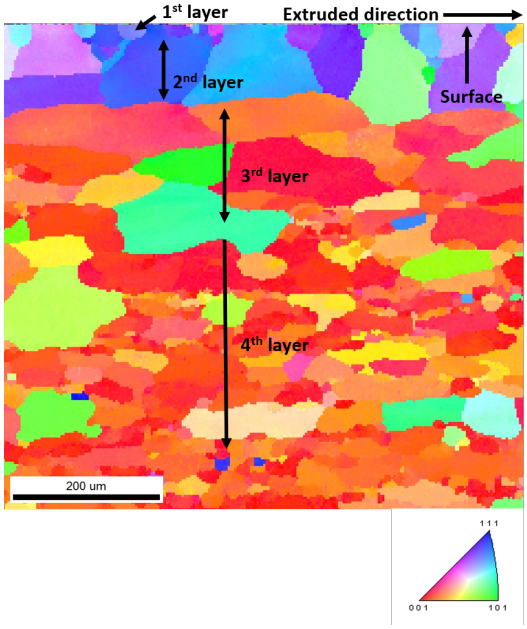

(a) Grain orientation map

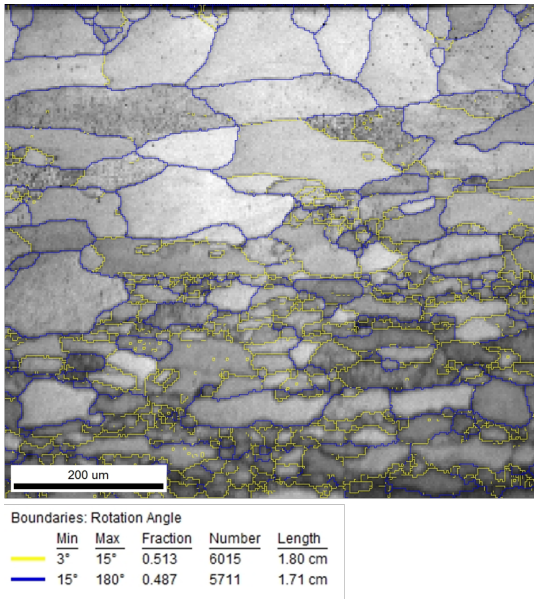

(b) Grain boundary misorientation map

Figure 4.5: Grain orientation map (a) and grain boundary misorientation map (b) of variant Cu17_Zn05_WQ_S.

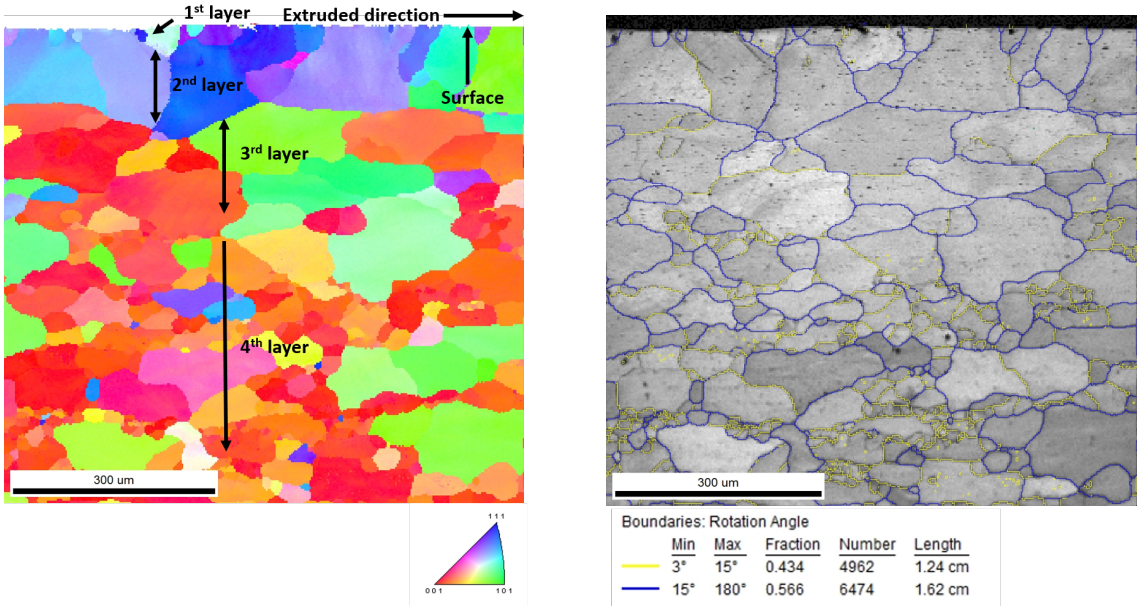

(a) Grain orientation map **(b)** Grain boundary misorientation map

Figure 4.6: Grain orientation map (a) and grain boundary misorientation map (b) of variant Cu17_Zn05_AC_S.

4.2.3 TEM

The results presented in this section were obtained by Calin D. Marioara[1].

Water-Quenched Not Pre-Stretched

The results of the EDS mapping of one of the grain boundaries that were investigated in the Cu17_Zn05_WQ_NS variant, are shown in Figure 4.7. Fine grain boundary precipitates containing silicon, magnesium and copper were present along the grain boundary. The PFZ was narrow and had a thickness of approximately 80 nm. Copper had segregated to the grain boundary and was present both in precipitates and as an enriched film. Figure 4.7(e) reveal AlFeMnSi-dispersoids. No heterogeneous precipitation had taken place at these dispersoids.

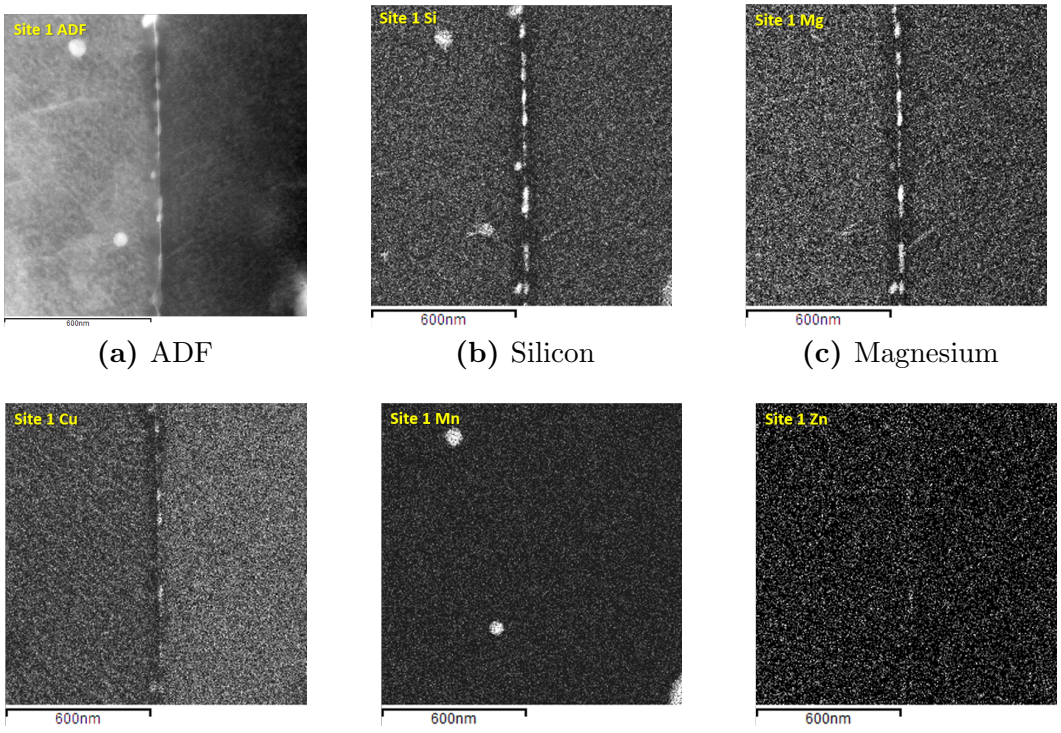

(a) ADF **(b)** Silicon **(c)** Magnesium

(d) Copper **(e)** Manganese **(f)** Zinc

Figure 4.7: EDS mapping of a grain boundary in the Cu17_Zn05_WQ_NS.

Air-Cooled Not Pre-Stretched

The result of the EDS mapping of a grain boundary of the Cu17_Zn05_AC_NS variant that were investigated, is shown in Figure 4.8. Only two precipitates were present at the grain boundary. The grain boundary precipitates were coarser than the ones observed in the WQ_NS variant. The PFZ had a thickness of approximately 500 nm. Copper had segregated somewhat to the grain boundary but was barely visible. Needle-shaped precipitates containing magnesium and silicon were revealed, and seem

[1]SINTEF Industry, Materials and Nanotechnology

to have precipitated heterogeneously at dispersoids. Copper was present in a few precipitates on the grain boundary and in the bulk.

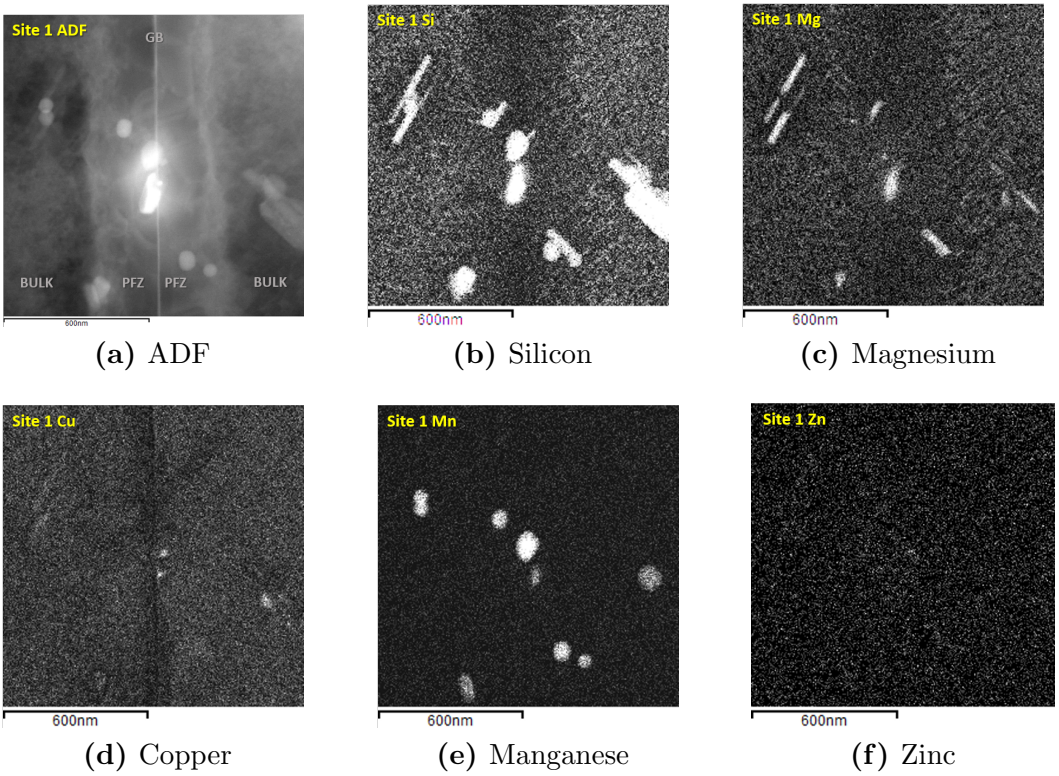

(a) ADF **(b)** Silicon **(c)** Magnesium

(d) Copper **(e)** Manganese **(f)** Zinc

Figure 4.8: EDS mapping of a grain boundary in the Cu17_Zn05_AC_NS.

Segregation to Grain Boundaries

The average values of how depleted the PFZs were as compared to the bulk, when the bulk is normalized for each element, are given in Table 4.1. The average values were obtained from two grain boundaries of each variant, and the solute concentration measured of the bulk includes both precipitates and the solid solution in-between precipitates. Solute elements; silicon, magnesium and copper were more depleted in the PFZ of the water-quenched variant than in the air-cooled variant. Copper is the least depleted element in the PFZ, but has segregated to the grain boundary in both air-cooled and water-quenched variants. Figure 4.9 show that grain boundary segregation to a HAGB in the AC_NS condition was not uniform. The PFZ was less depleted close to the bulk, while close to the grain boundary the solute concentration is similar to the solute concentration in the WQ_NS variant.

Table 4.1: Average values of how depleted the PFZs were as compared to bulk, when the bulk is normalised for each element.

Variant	Silicon	Magnesium	Copper
AC_NS	30.15	33.53	82.03
WQ_NS	24.10	17.25	60.00

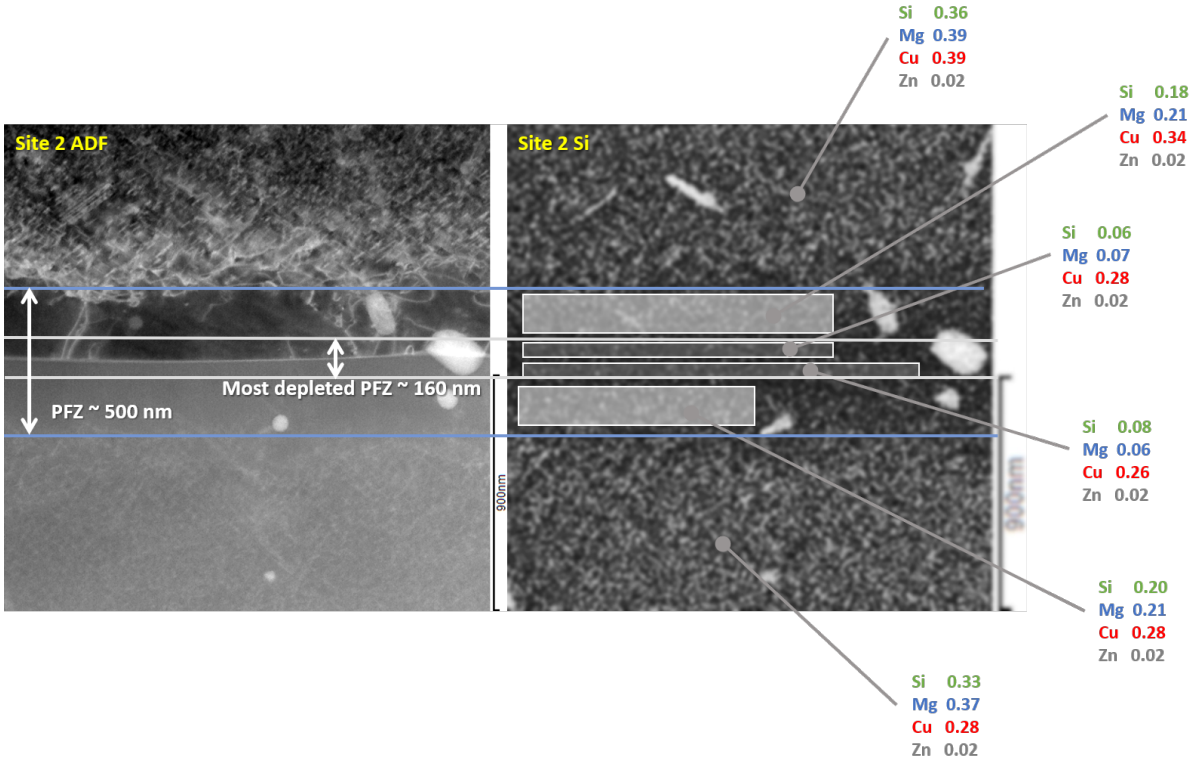

Figure 4.9: EDS mapping of a high angle grain boundary in the AC_NS variant. Solute concentrations are given in atomic percent.

4.3 Hardness

4.3.1 Effect of Processing Route

Measured Vickers hardness of each variation of composition and processing route is shown in Figure 4.10. It reveals that the hardness was more dependent on the processing route, than on chemical composition. Of the four different processing variants, water-quenched samples obtained the highest hardness. The WQ_NS samples had the highest measure hardness values, while WQ_S samples had the second highest measured hardness values. Between the air-cooled samples, the difference in hardness was small, but there was a tendency that the pre-stretched variant obtained slightly higher hardness. Measured Vickers hardness values of all parallels are given in Appendix B.2.

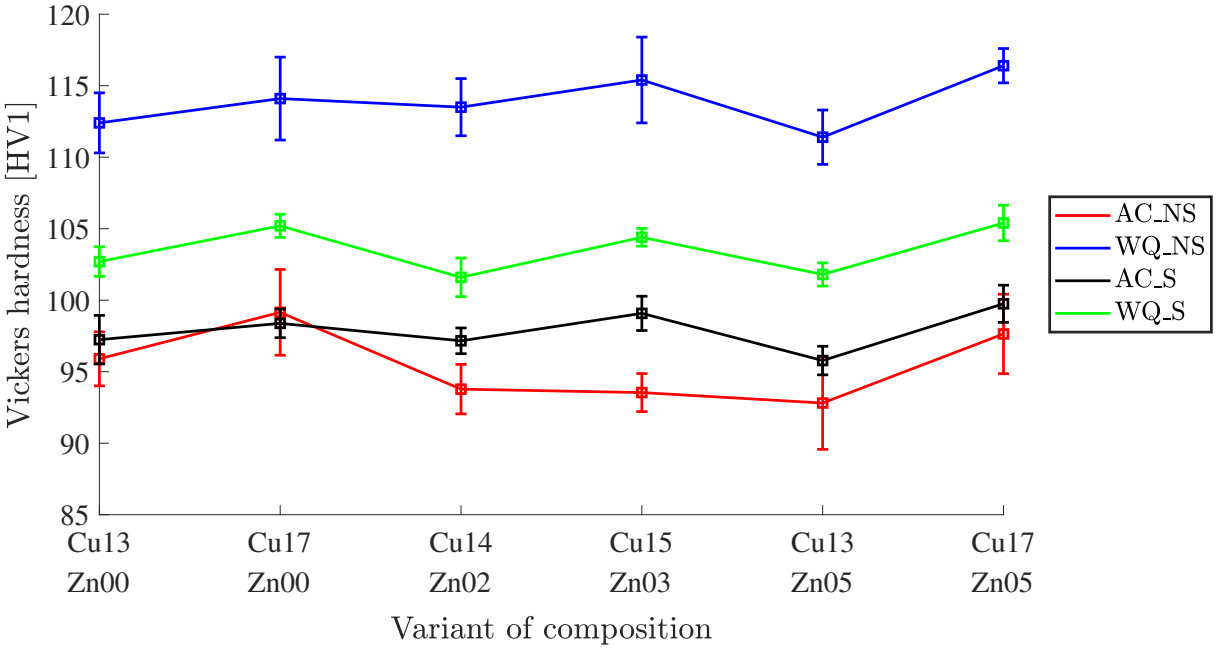

Figure 4.10: Vickers hardness of different variants of composition and processing route. Error bars show one standard deviation.

4.3.2 Effect of Composition

Figure 4.10 indicated that there was little difference in hardness between variants of different copper- and zinc-content.

Effect of Copper

Figure 4.11 shows measured Vickers hardness as a function of copper-content when the zinc-content is kept constant. Figure 4.11(a) display values for samples containing 0.00 wt% Zn and Figure 4.11(b) for samples containing 0.05 wt% Zn. All graphs in both plots show a slight increase in hardness with increasing copper content.

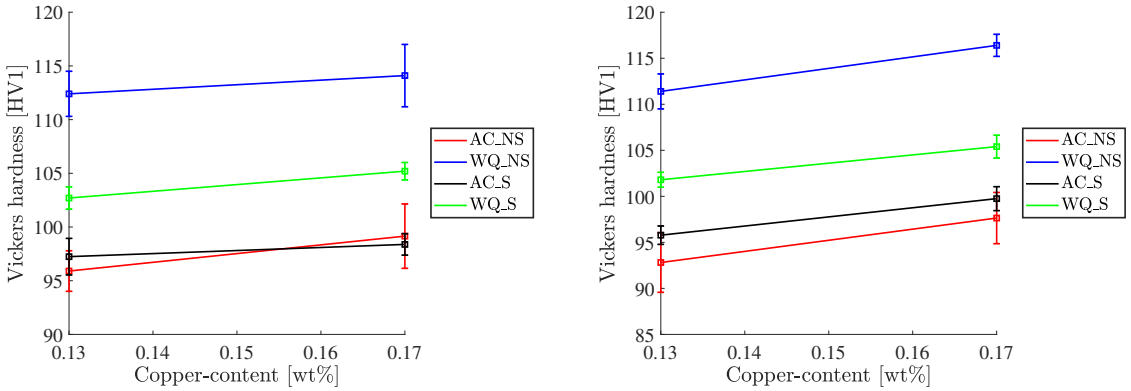

(a) 0.00 wt% Zn **(b)** 0.05 wt% Zn

Figure 4.11: Effect of copper-content on Vickers hardness of 6005.04 aluminium alloys. (a) Vickers hardness as a function of copper-content for alloys with 0.00 wt% Zn. (b) Vickers hardness as a function of copper-content for alloys with 0.05 wt% Zn. Error bars show one standard deviation.

Effect of Zinc

Figure 4.12 shows measured Vickers hardness values for constant copper-content and varying zinc-content. Figure 4.12(a) shows values obtained for alloys with a copper-content of 0.13 wt% and 4.12(b) shows values obtained for alloys with a copper-content of 0.17 wt%. The graphs reveal no significant correlation between zinc-content and hardness.

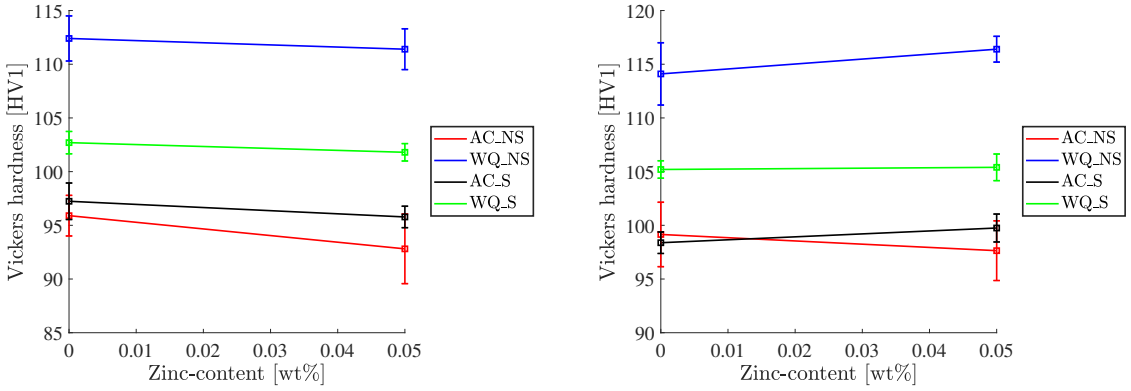

(a) 0.13 wt% Cu **(b)** 0.17 wt% Cu

Figure 4.12: Effect of zinc-content on Vickers hardness of 6005.04 aluminium alloys. (a) Vickers hardness as a function of zinc-content for alloys with 0.13 wt% Cu. (b) Vickers hardness as a function of zinc-content for alloys with 0.17 wt% Cu. Error bars show one standard deviation.

4.4 Electrical Conductivity

4.4.1 Effect of Processing Route

Measurements of electrical conductivity for all variants of composition and processing routes are shown in Figure 4.13. The results revealed that the processing route had more influence on the electrical conductivity than the copper- and zinc-content. Samples that were air-cooled obtained higher electrical conductivity than samples that were water-quenched. Further, the pre-stretched samples of both water-quenched and air-cooled variants obtained higher conductivity than their counterparts that were not pre-stretched. Measured electrical conductivity values of all parallels are included in Appendix B.3.

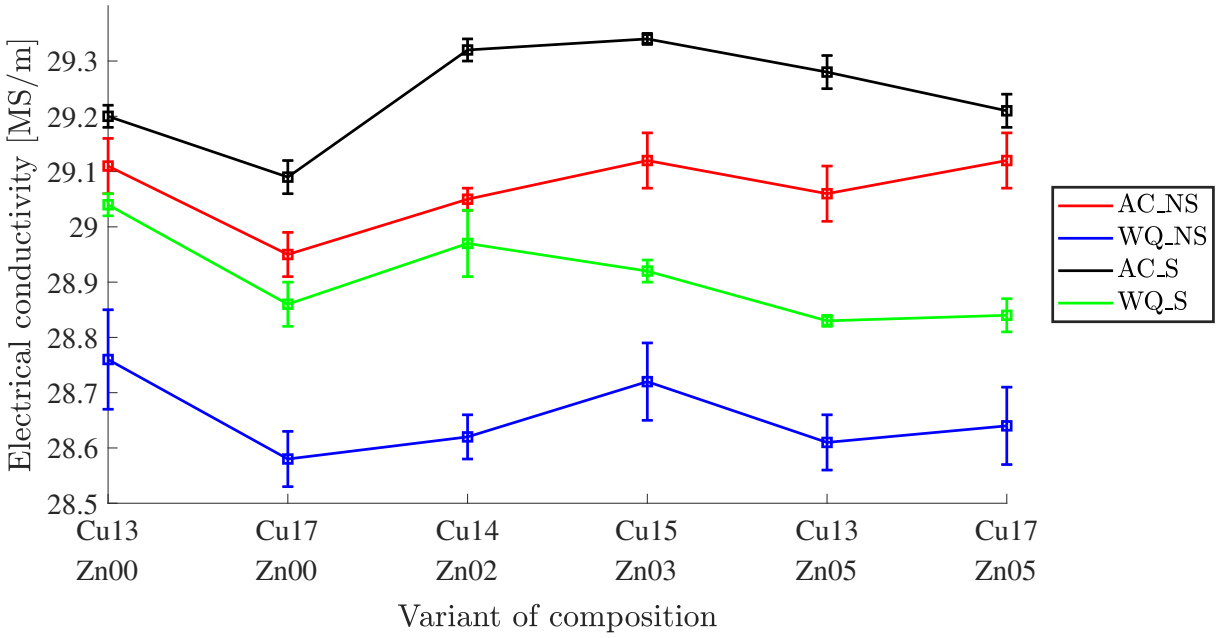

Figure 4.13: Electrical conductivity of different variants of composition and processing route. Error bars show one standard deviation.

4.4.2 Effect of Composition

From Figure 4.13, the effect of processing route on electrical conductivity was more evident than the effect of composition, and no clear trends of copper- and zinc-content was evident.

Effect of Copper

Measured electrical conductivity as a function of copper-content for a constant content of zinc is displayed in Figure 4.14. Figure 4.14(a) displays results for samples with zinc-content of 0.00 wt% and Figure 4.14(b) display the results for samples with zinc-content of 0.05 wt%. For the samples containing 0.00 wt% zinc, all the variants of processing route experienced a decrease in electrical conductivity with increasing copper-content. For samples that contain 0.05 wt% zinc there was no clear correlation between copper-content and electrical conductivity.

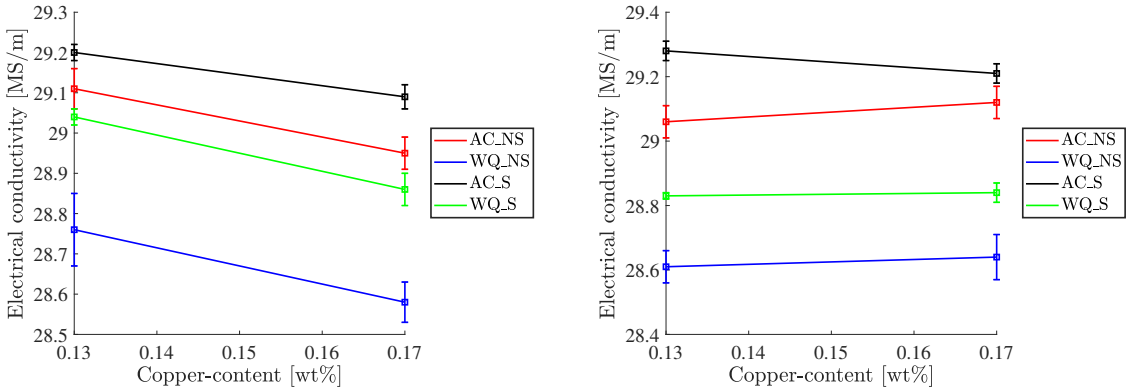

(a) 0.00 wt% Zn **(b)** 0.05 wt% Zn

Figure 4.14: Effect of copper-content on electrical conductivity of 6005.04 aluminium alloys. (a) Electrical conductivity as a function of copper-content for alloys with 0.00 wt% Zn. (b) Electrical conductivity as a function of copper-content for alloys with 0.05 wt% Zn. Error bars show one standard deviation.

Effect of Zinc

Measured electrical conductivity plotted as a function of zinc-content for a constant content of copper is shown in Figure 4.15. Figure 4.15(a) displays results for samples with copper-content of 0.13 wt% and Figure 4.15(b) display the results for samples with zinc-content of 0.13 wt%. There was no clear trend between zinc-content and electrical conductivity for constant copper content of 0.13 wt% or 0.17 wt%.

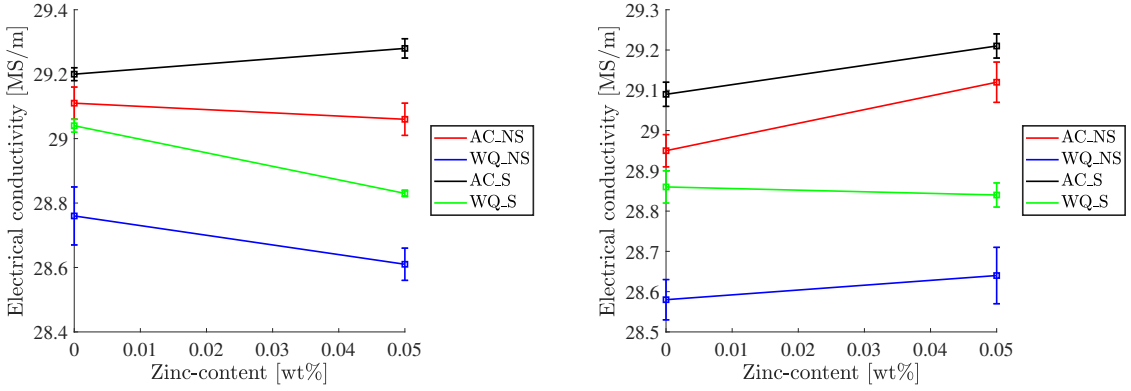

(a) 0.13 wt% Cu **(b)** 0.17 wt% Cu

Figure 4.15: Effect of zinc-content on electrical conductivity of 6005.04 aluminium alloys. (a) Electrical conductivity as a function of zinc-content for alloys with 0.13 wt% Cu. (b) Electrical conductivity as a function of zinc-content for alloys with 0.17 wt% Cu. Error bars show one standard deviation.

4.5 Accelerated Corrosion Test

4.5.1 Weight Loss

Weight loss per surface area after 24 hours of being immersed in acidified chlorine solution of each variant of composition and processing route, is shown in Figure 4.16. The processing route had a more significant effect on experienced weight loss than the difference in composition. Weight loss of water-quenched variants was greater than weight loss of air-cooled variants. Of the water-quenched variants, samples that were not pre-stretched experienced the greatest weight loss. There was a tendency that samples of the AC_S variant experienced slightly higher weight loss compared to the AC_NS variant.

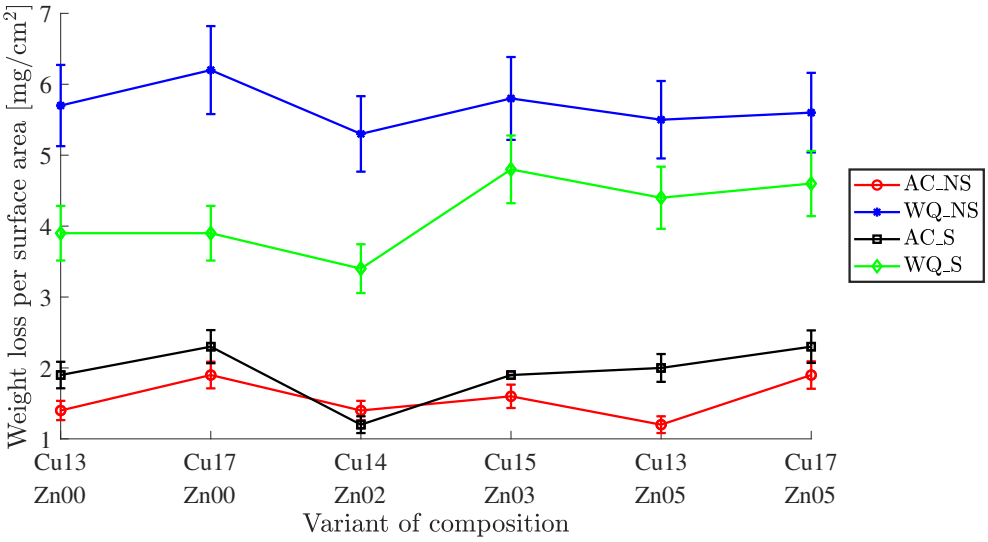

Figure 4.16: Weight loss per area of samples exposed to acidified chlorine solution for 24 hours. Error bars show one standard deviation.

Effect of Composition

Figure 4.17 shows weight loss as a result of the accelerated corrosion test as a function of copper-content for while the zinc-content is kept constant. Both variants with no zinc, Figure 4.17(a), and with 0.05 wt% zinc, Figure 4.17(b), shows a tendency of increased weight loss with increased copper-content.

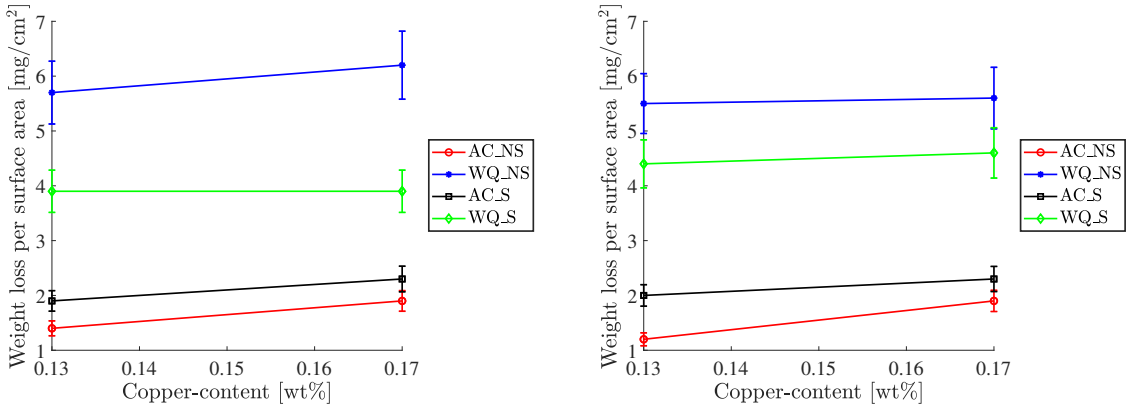

(a) 0.00 wt% Zn **(b)** 0.05 wt% Zn

Figure 4.17: Effect of copper-content on weight loss of 6005 aluminium alloys after immersion in acidified chlorine solution for 24 hours. Error bars show one standard deviation.

Weight loss after accelerated corrosion test as a function of zinc-content for alloys with 0.13 wt% copper is shown in Figure 4.18(a) and for alloys with 0.17 wt% copper is shown in Figure 4.18(b). There was not observed a clear correlation between zinc content and weight loss during the accelerated corrosion test.

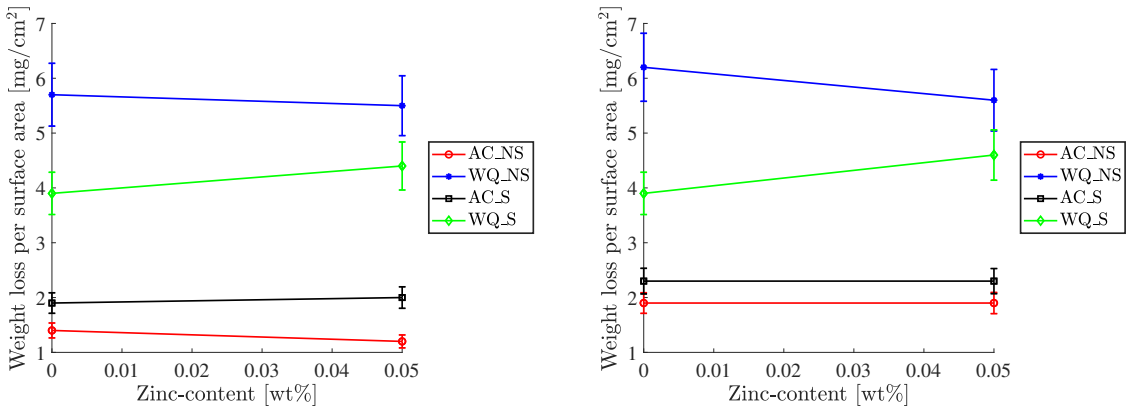

(a) 0.13 wt% Cu **(b)** 0.17 wt% Cu

Figure 4.18: Effect of zinc-content on weight loss of 6005 aluminium alloys after immersion in acidified chlorine solution for 24 hours. Error bars show one standard deviation.

Weight Loss Versus Hardness

The measured Vickers hardness of variant Cu17_Zn05 is plotted against the weight loss per surface area measured during the accelerated corrosion test for the same variant,

in Figure 4.19. It seems to be a close to linear relationship between hardness and weight loss experienced during accelerated corrosion test, where increased hardness also increase the weight loss.

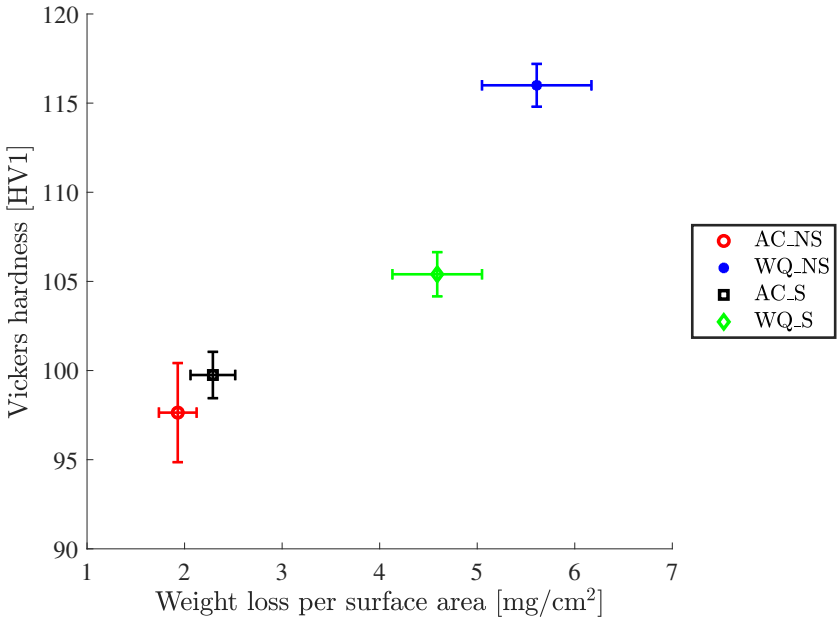

Figure 4.19: Vickers hardness plotted against the weight loss per area of samples exposed to acidified chlorine solution for 24 hours. The results used are for the variant Cu17_Zn05. Error bars show one standard deviation.

4.5.2 Investigation in Optical Microscope

Water-Quenched Not Pre-Stretched

Optical micrographs of WQ_NS samples exposed to acidified chlorine solution for 24 hours, obtained from a cross-section parallel to the extruded direction is shown in Figure 4.20. All the different variations in composition experience uniform IGC across the surface.

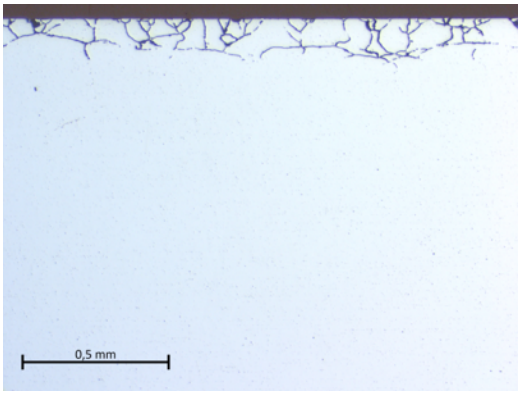

(a) Cu13_Zn00_WQ_NS

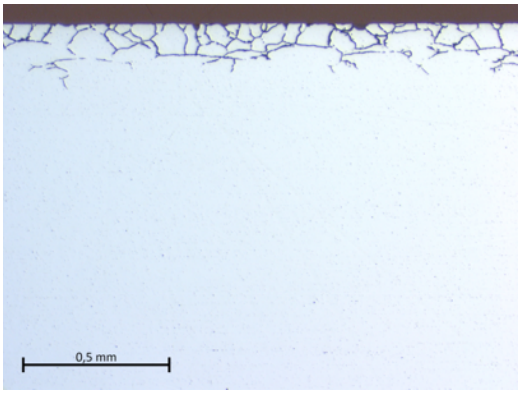

(b) Cu17_Zn00_WQ_NS

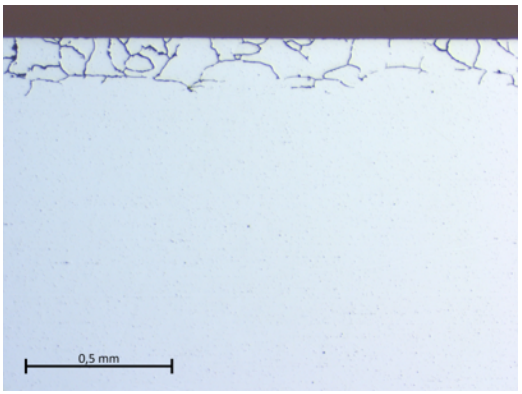

(c) Cu14_Zn02_WQ_NS

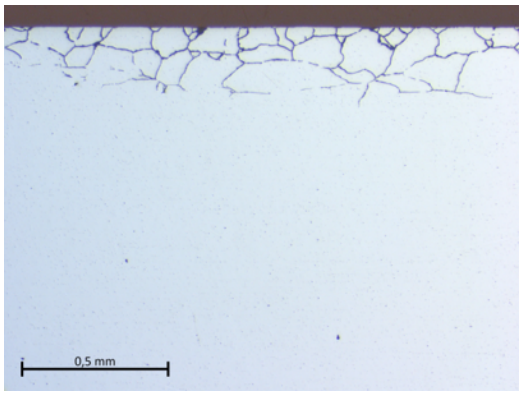

(d) Cu15_Zn03_WQ_NS

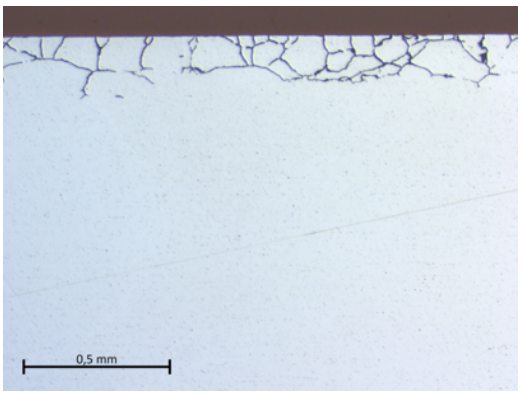

(e) Cu17_Zn05_WQ_NS

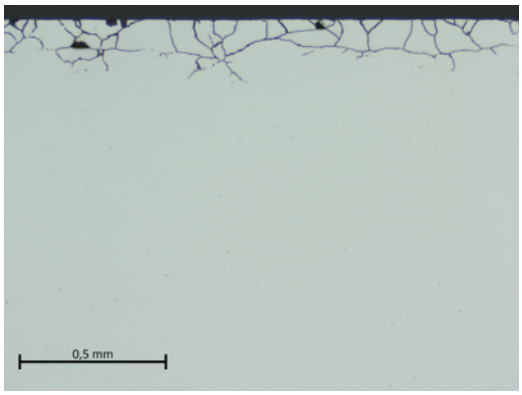

(f) Cu17_Zn05_WQ_NS

Figure 4.20: Optical micrographs obtained at 5x magnification of samples of WQ_NS that have been exposed to acidified chloride solution for 24. The cross-sections shown are parallel to the extruded direction.

Parameters obtained from the accelerated corrosion test are given in Table 4.2. Initial pH of the acidified chlorine solution was 1.05. The corrosion depth was in general between 200 μm and 250 μm, which correspond well with the depth of the layer of random texture close to the surface as was seen in the polarized light micrographs. Deepest maximum penetration was 345 μm, while the lowest was 259 μm.

Table 4.2: Results of accelerated corrosion test of water-quenched, not pre-stretched samples for different compositions.

Composition	Corrosion Mode	Max. Penetration Depth [μm]	Weight Loss [mg/cm^2]	pH After Immersion
Cu13_Zn00	Uniform IGC	345	5.7 +/-0.6	2.91
Cu17_Zn00	Uniform IGC	306	6.2 +/-0.2	3.63
Cu14_Zn02	Uniform IGC	259	5.3 +/-0.4	1.95
Cu15_Zn03	Uniform IGC	335	5.8 +/-0.2	2.95
Cu13_Zn05	Uniform IGC	272	5.5 +/-0.3	1.94
Cu17_Zn05	Uniform IGC	266	5.6 +/-0.2	3.68

Figure 4.21 shows a polarized light optical micrograph of a corroded sample of the variant Cu17_Zn05_WQ_NS. The micrograph shows that the IGC attacks is limited to the surface layer of random texture, with only a few IGC filaments penetrating down to some of the grains in the third layer elongated parallel to the surface.

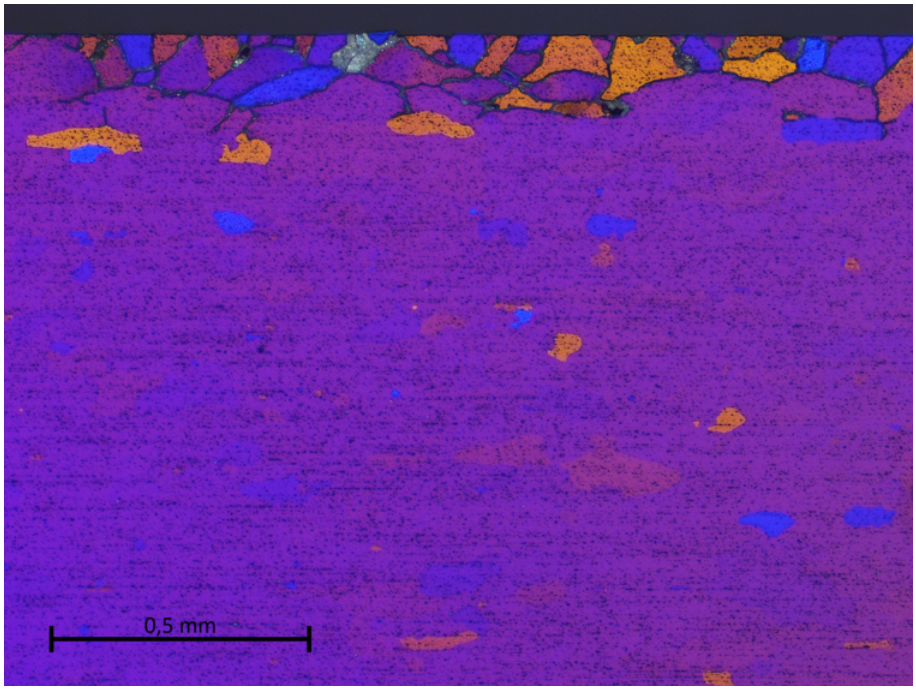

Figure 4.21: Polarized light optical micrograph of a sample of the variant Cu17_Zn05_WQ_NS after exposure for 24 hours to acidified chlorine solution. The cross section is parallel to the extruded direction.

Air-Cooled Not Pre-Stretched

Optical micrographs of AC_NS samples exposed to acidified chlorine solution for 24 hours, obtained from a cross-section parallel to the extruded direction is shown in Figure 4.22. There were no corrosion attacks visible on the surface of any of the variants of different composition.

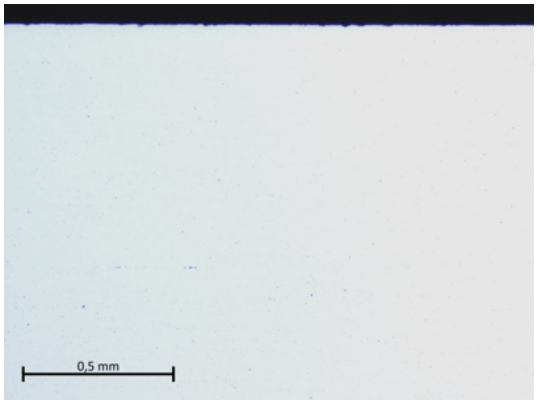

(a) Cu_13_Zn00_AC_NS

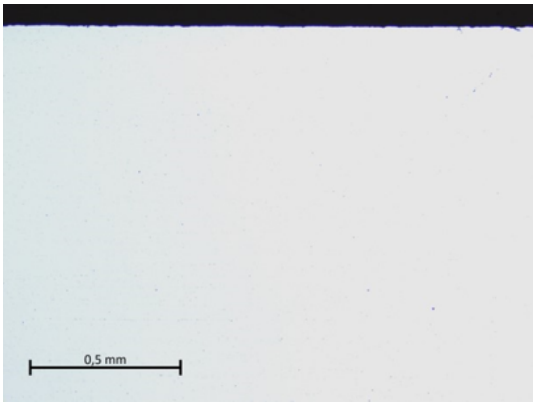

(b) Cu_17_Zn00_AC_NS

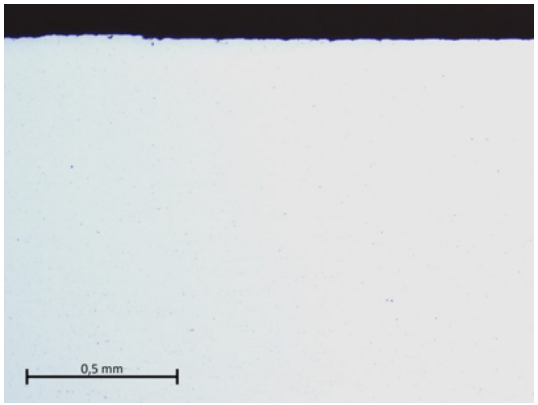

(c) Cu_14_Zn02_AC_NS

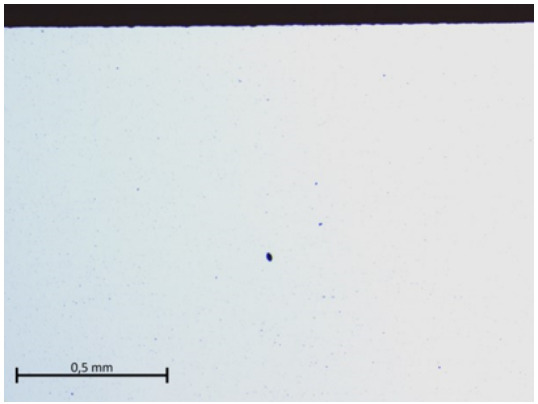

(d) Cu_15_Zn03_AC_NS

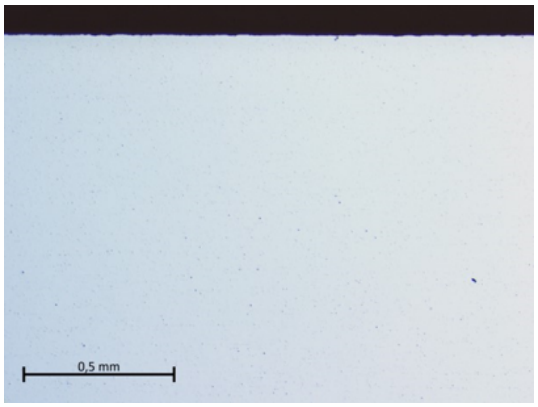

(e) Cu_13_Zn05_AC_NS

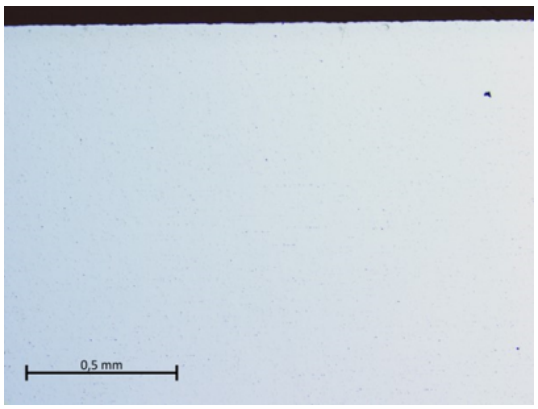

(f) Cu_17_Zn05_AC_NS

Figure 4.22: Optical micrographs obtained at 5x magnification of samples of AC_NS that have been exposed to acidified chloride solution for 24. The cross sections shown are parallel to the extruded direction.

Results of corrosion parameters obtained from accelerated corrosion tests for AC_NS samples are given in Table 4.3. The samples experience a weight loss between 1.2 - 1.9 mg/cm^2, which is significantly less than the weight loss of the WQ_NS samples. The acidified chlorine solution experienced little pH change during the accelerated corrosion test.

Table 4.3: Results of accelerated corrosion test of air-cooled, not pre-stretched samples for different compositions.

Composition	Corrosion Mode	Max. Penetration Depth [μm]	Weight Loss [mg/cm^2]	pH After Immersion
Cu13_Zn00	None	-	1.4 +/-0.3	1.20
Cu17_Zn00	None	-	1.9 +/-0.3	1.26
Cu14_Zn02	None	-	1.4 +/-0.6	1.20
Cu15_Zn03	None	-	1.6 +/-0.0	1.22
Cu13_Zn05	None	-	1.2 +/-0.1	1.19
Cu17_Zn05	None	-	1.9 +/-0.3	1.24

The mass loss of the AC_NS samples after the accelerated corrosion test is related to corrosion attacks on the cut edges that are perpendicular to the extruded direction. This is denoted as edge corrosion. Edge corrosion was the only mode of corrosion visible in the micrographs and was visible for all compositional variants. One example of edge corrosion is shown in Figure 4.23, showing an attack on Cu15_Zn03_AC_NS.

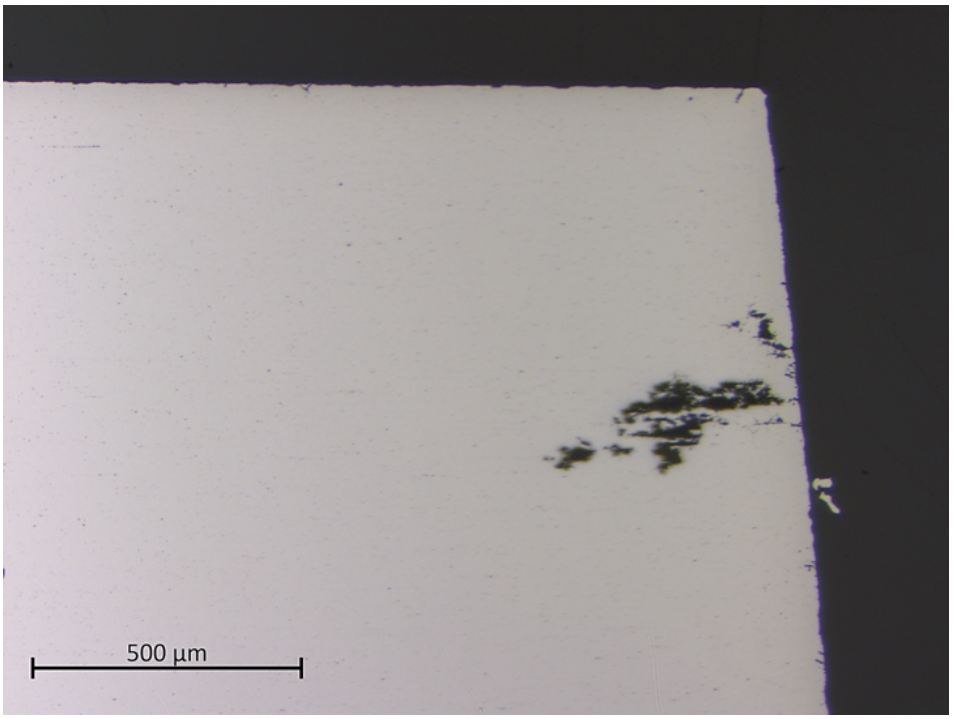

Figure 4.23: Optical micrograph obtained at 5x magnification of samples Cu15_Zn03_AC_NS that have been exposed to acidified chloride solution for 24. The cross sections shown are parallel to the extruded direction, at the edge of the sample.

Water-Quenched Pre-Stretched

Optical micrographs of WQ_S samples exposed to acidified chlorine solution for 24 hours, obtained from a cross-section parallel to the extruded direction is shown in Figure 4.24. Intergranular attacks are visible over most of the surface. In a few areas, there are corrosion attacks on the grain bodies, similar to pitting corrosion.

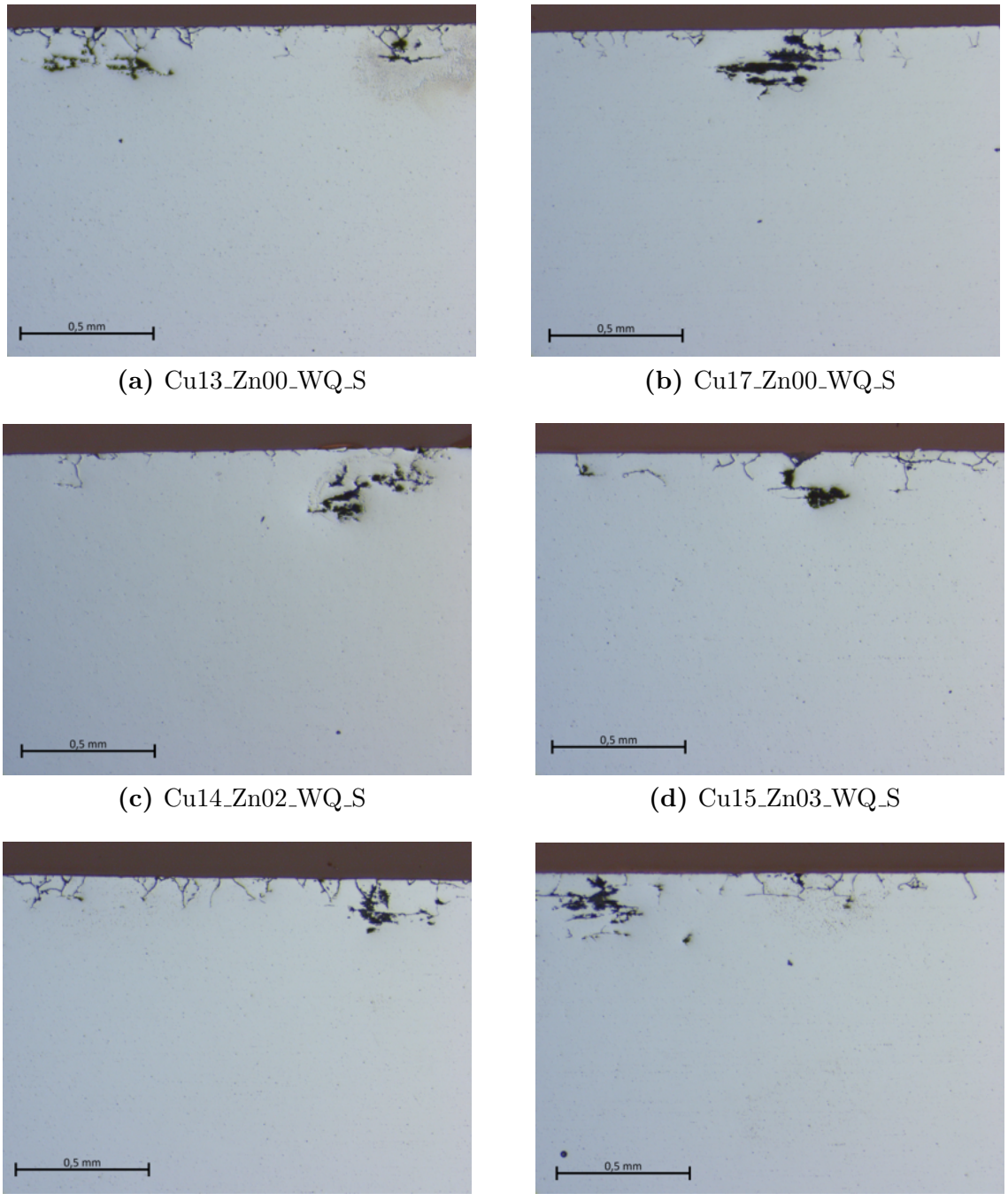

(a) Cu13_Zn00_WQ_S **(b)** Cu17_Zn00_WQ_S

(c) Cu14_Zn02_WQ_S **(d)** Cu15_Zn03_WQ_S

(e) Cu13_Zn05_WQ_S **(f)** Cu17_Zn05_WQ_S

Figure 4.24: Optical micrographs of samples of WQ_S that have been exposed to acidified chloride solution for 24. The cross sections shown are parallel to the extruded direction.

The results obtained from the accelerated corrosion test on WQ_S samples are given in Table 4.4. The weight loss and change in pH is significantly lower than experienced for WQ_NS samples. On average, the IGC depth is reduced as compared to WQ_NS samples. The deepest attacks are seen where the corrosion attacks have propagated from intergranular attack to attack the grain bodies. Deepest measured maximum penetration depth was 369 μm, and most shallow maximum penetration depth was 264 μm. This is similar to the maximum penetration depths obtained by the WQ_NS samples.

Table 4.4: Results of accelerated corrosion test of water-quenched, pre-stretched samples for different compositions.

Composition	Corrosion Mode	Max. Penetration Depth [μm]	Weight Loss [mg/cm^2]	pH After Immersion
Cu13_Zn00	IGC/Pitting	274	3.9 +/-0.1	1.50
Cu17_Zn00	IGC/Pitting	264	3.9 +/-0.0	1.43
Cu14_Zn02	IGC/Pitting	277	3.4 +/-0.1	1.34
Cu15_Zn03	IGC/Pitting	369	4.8 +/-0.2	1.72
Cu13_Zn05	IGC/Pitting	265	4.4 +/-0.3	1.60
Cu17_Zn05	IGC/Pitting	329	4.6 +/-0.5	1.63

Air-Cooled Pre-Stretched

Optical micrographs of AC_S samples exposed to acidified chlorine solution for 24 hours, obtained from a cross section parallel to the extruded direction is shown in Figure 4.25. Four out of six compositional variants experienced pitting corrosion in the cross-section that was investigated. Of the samples that did experience pitting corrosion, most of the surface was not attacked while 3-5 pits were visible. Cu13_Zn00_AC_S and Cu14_Zn02_AC_S did not experience pitting corrosion on the surface of cross-section investigated but experienced slight edge corrosion.

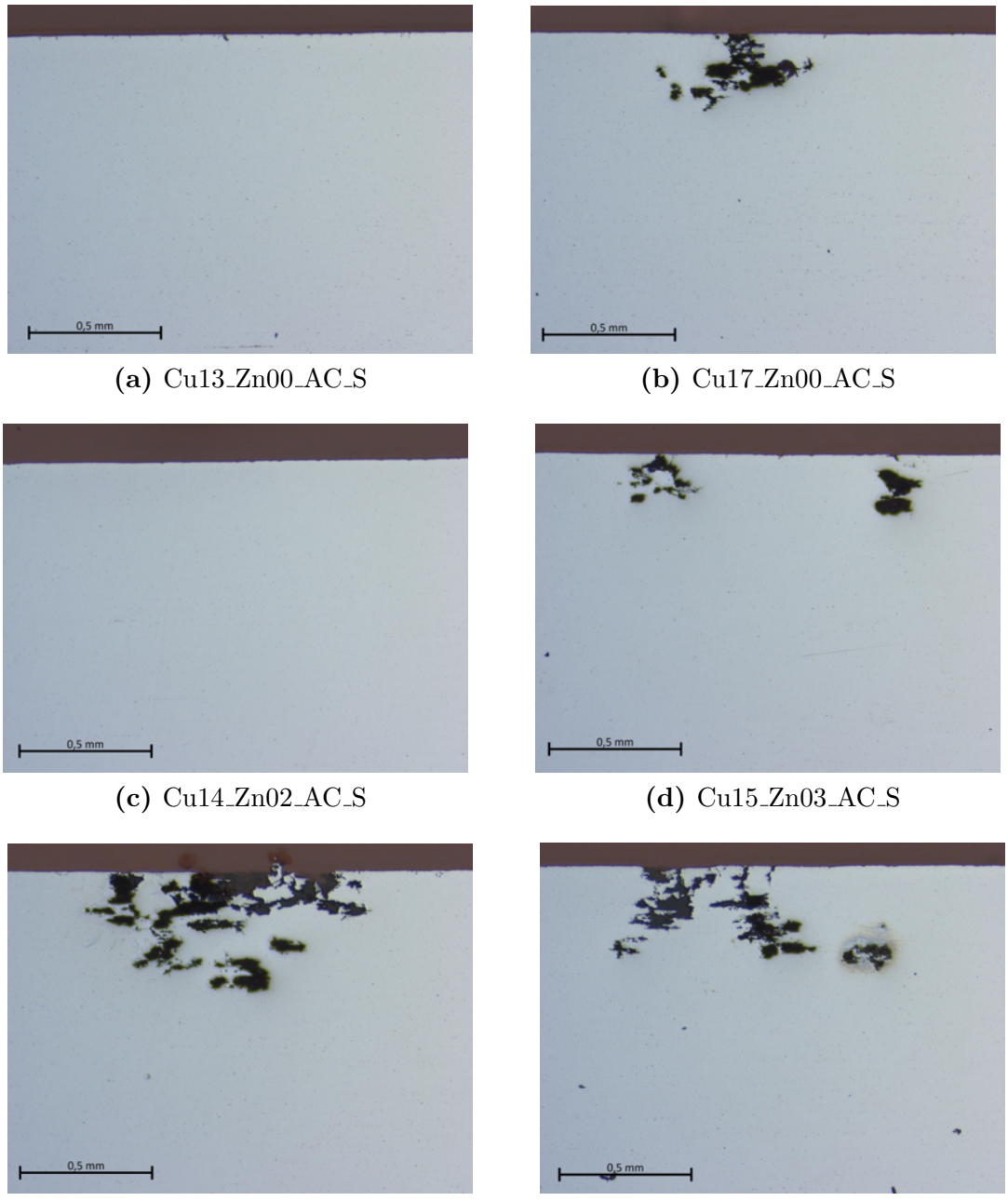

(a) Cu13_Zn00_AC_S **(b)** Cu17_Zn00_AC_S

(c) Cu14_Zn02_AC_S **(d)** Cu15_Zn03_AC_S

(e) Cu13_Zn05_AC_S **(f)** Cu17_Zn05_AC_S

Figure 4.25: Optical micrographs of samples of AC_S that have been exposed to acidified chloride solution for 24. The cross sections shown are parallel to the extruded direction.

Corrosion parameters obtained from accelerated corrosion test is given in Table 4.5. The weight loss and change in pH is in general, slightly higher than experienced by AC_NS samples. Maximum penetration depth varied between 294 μm and 450 μm.

Table 4.5: Results of accelerated corrosion test of air-cooled, pre-stretched samples for different compositions.

Composition	Corrosion Mode	Max. Penetration Depth [μm]	Weight Loss [mg/cm^2]	pH After Immersion
Cu13_Zn00	Pitting	-	1.9 +/-0.1	1.15
Cu17_Zn00	Pitting	395	2.3 +/-0.1	1.21
Cu14_Zn02	Pitting	-	1.2 +/-0.0	1.11
Cu16_Zn04	Pitting	294	1.9 +/-0.1	1.17
Cu13_Zn05	Pitting	450	2.0 +/-0.1	1.16
Cu17_Zn05	Pitting	404	2.3 +/-0.1	1.20

4.5.3 Penetration Depth

The maximum penetration depth of corrosion attacks of each variant of processing route and composition after accelerated corrosion tests is shown in Figure 4.26. The water-quenched samples did not show a significant change in maximum penetration depth with pre-stretching. The water-quenched samples obtained maximum penetration depth between 250 μm and 370 μm independent of whether pre-deformation was performed or not. The AC_NS variant did not experience any corrosion attacks on the surface of the cross-section investigated. For the AC_S variant no attacks were observed for alloys Cu13_Zn00 and Cu14_Zn02, to pits with penetration depths around that 400 μm for alloys Cu17_Zn00, Cu13_Zn05 and Cu17_Zn05.

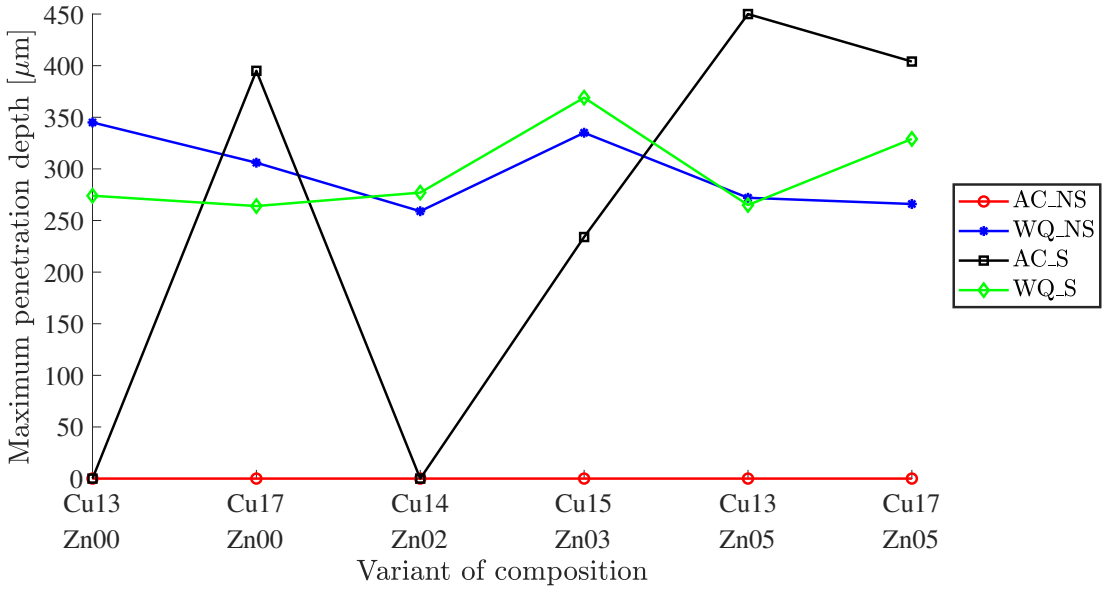

Figure 4.26: Maximum penetration depth of samples exposed to acidified chlorine solution for 24 hours. Error bars show one standard deviation.

Effect of Composition

Figure 4.27 and Figure 4.28 show maximum penetration depth as a function of copper-content and zinc-content, respectively. There is no significant correlation between the content of copper and zinc and the maximum penetration depth observed.

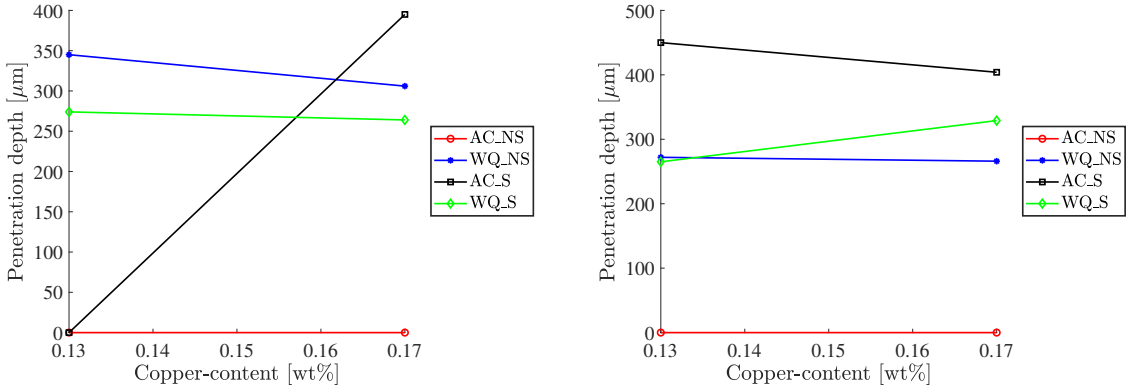

(a) 0.00 wt% Zn **(b)** 0.05 wt% Zn

Figure 4.27: Effect of copper-content on the maximum penetration depth of 6005 aluminium alloys after immersion in an acidified chlorine solution for 24 hours. Error bars show one standard deviation.

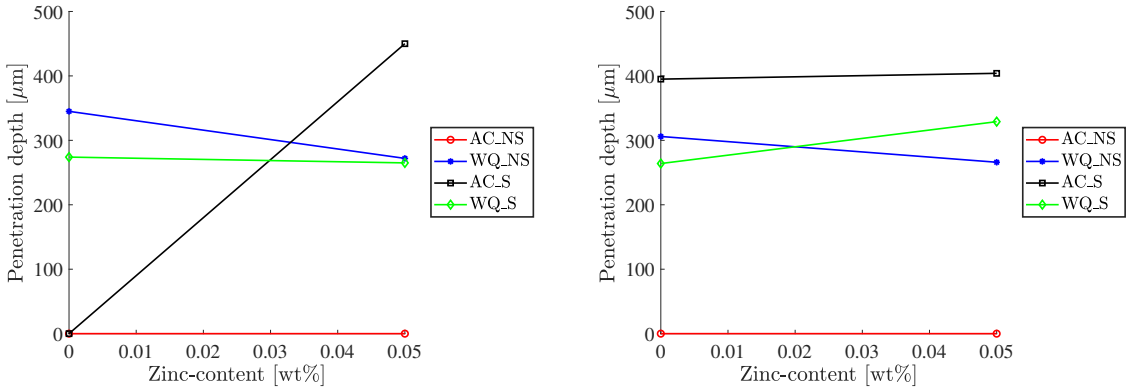

(a) 0.13 wt% Cu **(b)** 0.17 wt% Cu

Figure 4.28: Effect of zinc-content on the maximum penetration depth of 6005 aluminium alloys after immersion in an acidified chlorine solution for 24 hours. Error bars show one standard deviation.

Chapter 5

Discussion

5.1 Effect of Cooling Rate on Hardness

Vickers hardness measurements revealed that increased cooling rate after SHT leads to increased hardness. As seen in Figure 4.10, the water-quenched variants obtained significantly higher hardness than corresponding air-cooled variants.

As elaborated in Section 2.3.2, the cooling rate after SHT will determine the level of supersaturation. Slow cooling after SHT will reduce the level of supersaturation because of precipitation of MgSi-phases, and consequently less solute magnesium and silicon will be available for precipitation of hardening phases during artificial ageing [8, 36, 37]. Reducing the cooling rate may also reduce the amount of quenched-in vacancies, which can affect the formation of hardening β''-phase [41]. A low cooling rate is thus expected to induce lower hardness than a rapid cooling rate, due to the lower amount of hardening phases and an inhomogeneous distribution which corresponds well with the results obtained in this work. The upper critical cooling rate to avoid precipitation of MgSi-phases in a 6005 aluminium alloy was reported to be 6.25 °C/s [37]. The average cooling rate during air cooling from 540 °C down to 370 °C was approximately 9.5 °C/s, indicating that precipitation is restricted. Figure 4.1, where measured average cooling rate plotted in the TTP-diagram, shows that the plotted cooling curve comes close to touching the nose of the C-curve indicating 10% precipitation at 370 °C after 25 seconds. As the quench sensitivity is dependent on both composition and dispersoid density, the exact event of precipitation may be somewhat different from what was observed by Milkereit et al. while developing the TTP-diagram [31, 43]. As the cooling curve was laying close to the nose indicating 10% precipitation of β'- and B′-phase it is likely that some precipitation of these phases have taken place on dispersoids.

Electrical conductivity measurements indicated a lower amount of solutes in solid solution in the AC_NS variant, as the electrical conductivity of AC_NS samples was higher than the WQ_NS samples, as shown in Figure 4.13. EDS mapping, presented in Section 4.2.3, confirmed that MgSi-phases had precipitated on dispersoids in the AC_NS variant, while there were no observed precipitates on the dispersoids in the WQ_NS variant. It was not performed an analysis of the number density or distribution

of β''-precipitates in this work, but based on the presented literature and experimental results, the reduce hardness observed with reduced cooling rate is likely to be because of a reduced amount of hardening β''-precipitates.

5.2 Effect of Pre-Deformation on Hardness

The water-quenched and air-cooled variants experienced a different influence of pre-deformation on hardness. The measured Vickers hardness was presented in Figure 4.10, and showed that the hardness of the water-quenched variant was reduced when pre-deformation was applied. The influence of pre-deformation on the hardness of the air-cooled variants was not pronounced, although, there was a tendency that the AC_S variant obtained slightly higher hardness than the AC_NS samples.

As described in Section 2.3.3, deformation increases the dislocation density. Increased dislocation density increases the hardness because of enhanced hindrance of dislocation movement [25, 44]. However, pre-deformation can reduce the age-hardening response as dislocations suppress formation Mg-Si co-clusters and β''-precipitates and promote precipitation of post-β''-phases such as β'-, B′- and Q′-precipitates. Precipitation rate increases with pre-deformation as dislocations acts as high diffusion paths and precipitation may take place on heterogeneously dislocation lines during artificial ageing [45, 46, 46, 47, 48, 49, 50]. The hardening mechanism of pre-deformed and subsequently artificially aged AlMgSi-alloys is a combination of strain hardening and age-hardening [49]. The lower age-hardening response of WQ_S samples compared with WQ_NS indicates that the introduced dislocations have reduced the number of hardening phases and caused an inhomogeneous distribution. Further, the strain hardening contribution induced by dislocations does not compensate for the reduced age-hardening response. During artificial ageing dislocations density is reduced due to annihilation and rearrangement of dislocations [25, 52]. The reduced dislocation density during artificial ageing is a possible reason for why strain hardening does not compensate for the loss in age-hardening response. The hardness of air-cooled the variants did not significantly change with pre-stretching, although there was a slight tendency that hardness increased with pre-stretching. This indicates that the effect of strain hardening compensates for the reduced age-hardening response of the air-cooled variant.

Reports on the effect of deformation prior to artificial ageing have not been unambiguous. Kolar reported that the pre-deformed materials obtained higher hardness than undeformed materials after artificial ageing [49]. Grønvold reported that hardness obtained of a 6005.40 aluminium alloy after artificial ageing was independent of the degree of pre-deformation, while a 6016 aluminium alloy experienced reduced hardness when deformation was applied prior to artificial ageing. The reduced hardness was proposed to be caused by overageing because of increased precipitation kinetics and a higher content on silicon [16]. Jin et al. reported that in an AlMgSi(Cu)-alloy 5% pre-deformation reduced artificial ageing time to reach peak hardness by 50% [87]. Overageing might be a contributing factor to the reduced hardness of the WQ_S. However, overageing is not observed in the AC_S, and since hardness measurements as a function of artificial ageing time were not performed, overageing can not be confirmed.

5.3 Effect of Composition on Hardness

Vickers hardness measurements revealed that variating the processing route had considerably more influence on hardness than variation in copper- and zinc-content. Still, Figure 4.11 shows that there was a slight increase in hardness with increasing copper-content. This is in accordance with literature reporting that copper refines precipitates and increase precipitate number density, which has a positive effect on the hardness [17, 58].

As shown in Figure 4.12 and Figure 4.15, zinc-content did not affect the hardness or the electrical conductivity of any of the variations studied. An increase in both hardness and electrical with zinc-content is reported in the literature. The addition of 1 wt% zinc has been reported to slightly increase the hardness and decrease the conductivity in an AlMgSi-alloy, while addition of 0.1 wt% zinc has shown not to affect hardness or conductivity. Higher hardness was related to an observed refinement of precipitates, while the increase in electrical conductivity was proposed to be due to more zinc present in solid solution [19]. An increase in hardness and a decrease in electrical conductivity of copper-free AlMgSi-alloys containing 0.6 wt% zinc has also been reported [20]. Considering the maximum content of zinc in this work is 0.05 wt%, it is in accordance with reported literature that the hardness and electrical conductivity was not influenced by zinc-content.

5.4 Effect of Cooling Rate on IGC Susceptibility

The accelerated corrosion test revealed that there was a significant difference in the IGC susceptibility between air-cooled and water-quenched variants. Micrographs of the samples exposed to acidified chlorine solution were presented in Section 4.5.2. The WQ_NS variant experienced uniform IGC across the surface, while no IGC attacks were observed at the surface of the AC_NS variant.

As elaborated in Section 2.4, one important method to reduce the IGC susceptibility of extruded AlMgSi(Cu)-alloys is to reduce the amount of copper on grain boundaries to promote discontinuity of the copper-enriched film [9, 11, 13]. Reducing the cooling rate from SHT leads to the formation of coarser of grain boundary precipitates [14]. Coarsening of grain boundary precipitates have been proposed to cause a discontinuity of copper enriched film at the grain boundaries [9, 61]. Nucleation of copper-containing precipitates on dispersoids, such as Q′-phase, is promoted by reducing the cooling rate. Increased disorder in bulk β''-precipitates is also promoted by reduced cooling rate, which can increase the amount of copper that is incorporated into the precipitates. A positive correlation between the amount of copper incorporated in precipitates and the resistance to IGC has been observed [13].

The results of EDS mapping, presented in Section 4.2.3, revealed that copper had segregated to the grain boundary in both air-cooled and water-quenched variants. Though it seems that the amount of copper on the grain boundary was slightly higher in the WQ_NS variant than in the AC_NS samples. In the WQ_NS variant, fine copper-containing precipitates were present at the grain boundary and connected by a copper-enriched film. In the AC_NS, variant the grain boundary precipitates were

coarse, and the amount of copper observed at the grain boundary seems to be less than what was observed in the WQ_NS variant. Generally, the less amount of copper observed in a grain boundary plane the higher is the possibility that the copper-enriched film is discontinuous [13]. The difference in the amount of copper observed in the grain boundary plane, indicates that a continuous copper-enriched film is more probable in the WQ_NS variant than in the AC_NS variant. As a discontinuity of the copper-enriched film has been reported to increase IGC resistance, the low amount of copper observed on the grain boundary in the AC_NS is the probable reason for the observed IGC resistance [9]. Reduced cooling rates generally leads to increased width of the PFZs, which was also observed in this work by EDS mapping of the grain boundary region of the AC_NS and WQ_NS variants [14, 17]. Segregation of solute in the PFZ was lowest in the AC_NS variant, and the segregation was not uniform, as shown in Figure 4.9. In approximation, the less depletion of the PFZ could cause a lower difference in corrosion potential between PFZ and solid solution, which could attribute to the IGC resistance observed in the AC_NS variant. The results obtained from EDS mapping and accelerated corrosion test, suggests that increased resistance with decreasing cooling rate is due to reduced amount of copper on the grain boundaries leading to a discontinuity of the copper-enriched film.

AC_NS samples were resistant to IGC at the surface, but experienced edge corrosion, as shown in Figure 4.23. Lam studied the relation between edge corrosion and IGC susceptibility in AlMgSi(Cu, Zn)-alloys. The reported results were that samples in T5 condition, which had a non recrystallized fibrous structure in the centre and were resistant to IGC at the surface, could experience IGC attacks when the edges were covered during BS-ISO 11846 accelerated corrosion test. Samples in T6 condition that were completely recrystallized, were susceptible to IGC without covering the edges and covering the edges did not increase the severity of the IGC attack. It was proposed that the fibrous structure at the edges acted as a form of sacrificial anode for the samples in T5 condition [21]. In this work, the samples are completely recrystallized and do not have the fibrous structure at the centre, and are, therefore, not directly comparable. However, as there are no IGC attacks at the surface, and there are examples of edge corrosion, these samples may experience IGC attacks at the surface if the edges were covered.

5.4.1 Effect of Pre-Deformation on IGC Susceptibility

Water-Quenched Pre-Stretched

The accelerated corrosion test revealed that the weight loss per surface was significantly reduced when water-quenched variants were pre-deformed, as was shown in Figure 4.16. This indicates a suppression in IGC attacks. It was confirmed by the optical micrographs presented in Section 4.5.2. For WQ_S samples, the corrosion attacks tend to be a little more localized than the WQ_NS samples. The attacks of WQ_S are mostly shallow IGC attacks, but in certain areas, grain bodies are attacked similar to pitting corrosion. In the areas of where grain bodies were attacked the penetration depth was similar to the maximum penetration depth of WQ_NS variants.

Deformation prior to artificial ageing increases the dislocation density, and induce

heterogeneous precipitation on dislocations lines during artificial ageing [47, 49]. Pre-deformation may increase the amount of copper that are incorporated into precipitates [13, 16]. As the IGC susceptibility is reduced by reducing the amount of copper on the grain boundary, precipitation of copper-containing precipitates on dislocations could be beneficial for the IGC resistance of AlMgSi(Cu)-alloys. A correlation between increased amount of copper incorporated in precipitates decreased amount of copper on grain boundaries and reduced IGC susceptibility have been reported [13]. The presented results of reduced weight loss and more localized and shallow IGC attacks by applying pre-deformation to the water-quenched variant indicates that precipitation on dislocation has increased the IGC resistance of the WQ_S variants studied. Even if annihilation of dislocations takes place during artificial ageing, precipitation at dislocations is still likely to have taken place as Teichman et al. reported that precipitation takes place on dislocations already after 10 minutes of artificial ageing at 190 °C [48]. Due to time constraints, the pre-stretched variants were not investigated in TEM and precipitation on dislocation lines was not confirmed, but it is expected as precipitation dislocations have been reported to take place in AlMgSi(Cu)-alloys pre-deformed 5% and 10% [16, 87].

The change in corrosion mode from only intergranular attack to a combination of intergranular attack with an additional pitting-like attack of grain bodies have been proposed to be due to coarsening of matrix precipitates and solute depletion of the matrix [16]. Accelerated precipitation kinetics cause coarser precipitates to be found in pre-deformed variants after artificial ageing as compared to undeformed variants [47, 49]. The Vickers hardness measurements, presented in Figure 4.10, and the electrical conductivity measurements, presented in Figure 4.13, indicate that the WQ_S variant has coarser precipitate and more depleted matrix. The lower hardness of the WQ_S compared with WQ_NS variant indicates the presence of coarser and less coherent precipitates, and the higher electrical conductivity of the WQ_S samples compared with the WQ_NS variant indicates fewer solutes in solid solution [86]. Coarsening of bulk precipitates and depletion of solute elements in the matrix leads to an increased electrochemical driving force between precipitates and matrix, which can induce the transition of corrosion mode from IGC to pitting corrosion [16, 61].

The pre-stretched variants in this work were stretched to 5% elongation, which is more than the typical industrial practice, which usually ranges from 1% to 3% [15]. Grønvold reported that the positive effect of pre-deformation on IGC resistance was negligible for AlMgSi-alloys pre-deformed 1%, while at 5% pre-deformation there was a significant increase in IGC resistance [16]. The effect of pre-deformation on IGC susceptibility may, therefore, be less in today's commercial alloys than compared with these results.

Air-Cooled Pre-Stretched

During the accelerated corrosion test, the AC_S variant experienced a slightly greater weight loss per surface area compared to AC_NS for most of the compositional variants. The optical micrographs were presented in Section 4.5.2. No visible corrosion attacks were observed at the surface of AC_NS samples, while pitting corrosion was observed at the surface of AC_S samples for four out of six compositional variants.

As described in the previous sub-chapter, the coarsening of matrix precipitates and depletion of solute in the matrix can increase the driving force for pitting corrosion [16, 61]. At the same time, the driving for IGC can be reduced due to less copper present on grain boundaries which may cause discontinuity of copper-enriched film on grain boundary [13]. EDS mapping revealed that the AC_NS variant seemed to have a low amount of copper at grain boundaries and coarser precipitates both on grain boundary and in the matrix. As dislocations acts as fast diffusion paths and increase rates of precipitation, pre-deformation can cause further coarsening of these precipitates [47, 49]. Increased coarsening of precipitates due to pre-deformation, indicates that the AC_S variant may obtain coarser precipitates and more depleted matrix than the AC_NS variant. As the driving for IGC is increased with coarser precipitates and more depleted matrix, this could explain the introduced susceptibility to pitting corrosion AC_S variant [16, 61].

The results of the electrical conductivity measurements, given in Section 4.4, revealed that the AC_S variant in general obtained higher electrical conductivity than AC_NS variant. The AC_S variant obtained average values of electrical conductivity between 28.95 - 29.12 MS/m, while the AC_NS variant obtained average values between 29.09 - 29.32 MS/m, depending on composition. Since electrical conductivity increases with decreasing amount of solutes in the matrix [18, 86], the higher electrical conductivity of the AC_S variant indicates that the matrix was more depleted in the AC_S variant than in the AC_NS variant. Similar values of electrical conductivity have been reported to correspond to the transition region from no localized corrosion to pitting corrosion of an air-cooled AlMgSi(Cu)-alloy during artificial ageing [61]. Four of the six different compositional variant of the AC_S variant experienced pitting corrosion as seen in the cross-section the in optical micrographs presented in Section 4.5.2. There was no correlation between the electrical conductivity measurement and observed pitting corrosion between the different compositional variants of the AC_S variant. As only one cross-section of each exposed sample was studied in optical microscope, it cannot be ruled out that the two samples were pitting was not observed could have experienced pitting corrosion at other locations of the samples. Overall the difference in electrical conductivity between the AC_NS variant and the AC_S variant indicates that depletion of solute from the matrix because of coarsening of matrix precipitates is a contributing factor to the pitting susceptibility of the AC_S variant [16, 61].

5.4.2 Effect of Microstructure on IGC Susceptibility

Figure 4.19 shows the measured Vickers hardness of the alloys plotted against the weight loss per surface area experienced during accelerated corrosion test of each processing variant of the Cu17_Zn05 variant. It illustrates the compromise between mechanical properties and corrosion behaviour of AlMgSi(Cu)-alloys, as increased hardness is obtained at the expense of reduced corrosion resistance. It should be noted that even though the AC_S variant experience little weight loss during the accelerated corrosion test, several of the pits observed penetrates deeper than the IGC attacks of the WQ_NS and WQ_S variant.

Results of the maximum penetration depths observed in each variant after accelerated corrosion test was presented in Section 4.5.3. The maximum penetration depths of

the WQ_NS variant and the WQ_S variant were between 250 μm and 370 μm, while the deepest attack observed in the AC_S variant was 450 μm. The limited depth of the IGC attacks can be attributed to the effect of microstructure on IGC attacks, which was elaborated in Section 2.4.3. HAGBs close to the surface are more prone to form PFZs and experience IGC than LAGBs in the centre [75]. Further, IGC is limited when propagating towards the smaller grains of the bulk, which leads to a more tortuous path along the grain boundaries [65]. The IGC filaments penetrated down to the grains of the third layer, elongated parallel to the surface, but not into the bulk, as shown in Figure 4.21. The EBSD analysis, presented in Section 4.2.2 revealed a layer-structure with mostly HAGBs close to surface, similar to described by Kumari [65] and Danbolt [74]. The transition from larger grains with straight grain boundaries to the tortuous grain boundary paths in the bulk and the transition of HAGBs close to the surface to LAGBs in the bulk, corresponds to the depths of IGC attacks observed. These microstructural features may be factors limiting the penetration depth of the IGC attacks [16, 65, 74].

The grain boundary misorientation maps revealed LAGBs within grains in the undeformed variants, which were unexpected as sub-grains form from dislocation cells [25, 52]. Due to time constraints, the observed LAGBs within grain were not further investigates, but as LAGBs are not observed within surface grains it is assumed that it does not significantly affect the IGC susceptibility.

5.4.3 Effect of Composition on IGC Susceptibility

The results from the specialisation project, which is included in Appendix C, indicated that the copper-content increased both weight loss and maximum penetration depth of the IGC attacks [22], which was in accordance with literature reporting that copper reduces corrosion resistance [7, 10]. The results in this work confirmed that the weight loss was greater for increased copper-content when the zinc-content was kept constant, as can be seen in Figure 4.17. This was the case for all variants of processing route. The maximum penetration depth of the water-quenched samples experiencing IGC attacks did not variate with copper-content, shown in Figure 4.27, as opposed to the results obtained in the specialisation project [22]. Of the air-cooled and pre-stretched samples experiencing pitting corrosion, the maximum penetration depth also seems to be independent of copper-content.

Zinc-content on IGC susceptibility did not show any effect on the IGC susceptibility in the specialisation project [22]. This was in accordance with reports of Saito stating that zinc-content below 0.1 wt% does not affect corrosion properties of AlMgSi-alloys [19]. It was also in accordance with reports by Lam [21] and Stoknes [20], who reported that IGC susceptibility was independent of zinc-content below 0.2 wt%. These reports together with the EDS mapping which did not reveal any significant segregation of zinc, suggest that the maximum zinc-content of 0.05 wt% in this work should not affect the corrosion properties, which is confirmed as increasing zinc-content did neither affect weight loss nor maximum penetration depth during the accelerated corrosion test.

5.5 Further Work

Varying the cooling rate from SHT between water-quench and air-cooling would be of great interest. Different cooling rates could be obtained by cooling with different rates of air-blasts or spraying with water, which are cooling systems that are industrially relevant. If one could successfully control the cooling rate, one can investigate if there is a threshold cooling rate that induces IGC susceptibility. Further, optimum values compromising of mechanical properties and corrosion behaviour can be mapped with regards to the cooling rate.

Investigation of the effect of depletion of solute in the PFZ on the IGC susceptibility could increase the understanding of the effect of cooling rate from SHT on corrosion behaviour of AlMgSi(Cu)-alloys. The depletion of solute elements in the PFZ observed by EDS mapping was significantly lower in the AC_NS variant than in the WQ_NS variant. Measuring the corrosion potential of the PFZ for different degree of solute depletion would give a further understanding of how depletion in the PFZ affect the microgalvanic coupling that can be induced between grain boundary and PFZ.

Accelerating corrosion test revealed edge corrosion in the AC_NS variant. It would be of interest to cover the edges of the AC_NS samples during accelerated corrosion test to investigate if this will initiate IGC attacks on the surface, as was seen in the work of Lam [21]. It is of relevance as a final product might be used in an application where edges are covered, and IGC attack could cause a catastrophic failure.

Chapter 6

Conclusion

The main objective of this master's thesis was to investigate how the IGC susceptibility of a 6005.04 aluminium alloy was affected by the cooling rate from SHT and pre-deformation. Also, the effect of copper- and zinc-content on IGC susceptibility was investigated. The effect of processing route was investigated by applying either water-quench or air-cooling after SHT, and whether a 5% pre-stretch was performed or not. Effect of composition was investigated by variating the copper-content between 0.13 - 0.17 wt% and zinc-content between 0.00 - 0.05 wt%.

The results of this master's thesis emphasise the trade-off between mechanical properties and corrosion resistance in extruded AlMgSi-alloys. The accelerated corrosion test revealed that the IGC susceptibility to a greater extent was dependent on the processing route, rather than the compositional variations of copper and zinc that was studied. Increased resistance to IGC can be obtained by proper thermomechanical treatment, however, IGC resistance is induced at the expense of hardness. Water-quenched variants experienced uniform IGC, while air-cooled variants were resistant to IGC. Increased IGC resistance with decreasing cooling rate was attributed to a lower amount of copper on grain boundaries, which has been reported to cause discontinuity of the copper-enriched film. Reducing the cooling rate reduced the obtained hardness, presumably because precipitation on dispersoids reduced the amount of solute available to form hardening phases.

Pre-deformation increased the IGC resistance but induced susceptibility to pitting corrosion. The water-quenched and pre-stretched variant experienced a combined IGC and pitting attack, while the air-cooled variants experienced pitting corrosion when pre-deformed. Strain hardening compensated for the loss in the age-hardening response for air-cooled variants, while the pre-deformation reduced the hardness in water-quenched variants.

Bibliography

[1] The Paris Agreement | UNFCCC. URL https://unfccc.int/process-and-meetings/the-paris-agreement/the-paris-agreement.

[2] Fourth Biennial Report from the European Union: under the United Nations Framework Convention on Climate Change, December 2019. URL https://www4.unfccc.int/sites/SubmissionsStaging/NationalReports/Documents/045612387_European%20Union-BR4-1-European%20Union-BR4_C_2019_8832_and_SWD_2019_432.pdf.

[3] Annual European Union greenhouse gas inventory 1990–2017 and inventory report 2019 — European Environment Agency. URL https://www.eea.europa.eu/publications/european-union-greenhouse-gas-inventory-2019. Library Catalog: www.eea.europa.eu.

[4] J. Hirsch. Aluminium in Innovative Light-Weight Car Design. *Materials Transacions*, 52(5):818–824, 2011.

[5] H. C. Kim and T. J. Wallington. Life-Cycle Energy and Greenhouse Gas Emission Benefits of Lightweighting in Automobiles: Review and Harmonization. *Environmental Science & Technology*, 47(12):6089–6097, June 2013.

[6] R. Lumley. *Fundamentals of Aluminium Metallurgy: Production, Processing and Applications*. Woodhead Publishing, Oxford, 2011.

[7] F. Campbell. *Elements of Metallurgy and Engineering Alloys*. ASM International, 1st edition, 2008.

[8] I. J Polmear. *Light alloys : from traditional alloys to nanocrystals*. Elsevier/Butterworth-Heinemann, Oxford, 4th edition, 2006.

[9] G. Svenningsen, M. H. Larsen, J. H. Nordlien, and K. Nisancioglu. Effect of thermomechanical history on intergranular corrosion of extruded AlMgSi(Cu) model alloy. *Corrosion Science*, 48(12):3969–3987, December 2006.

[10] G. Svenningsen, J. E. Lein, A. Bjørgum, J. H. Nordlien, Y. Yu, and K. Nisancioglu. Effect of low copper content and heat treatment on intergranular corrosion of model AlMgSi alloys. *Corrosion Science*, 48(1):226–242, January 2006.

[11] S.K. Kairy, P.A. Rometsch, C.H.J. Davies, and N. Birbilis. On the Intergranular Corrosion and Hardness Evolution of 6xxx Series Al Alloys as a Function of Si:Mg

Ratio, Cu Content, and Aging Condition. *CORROSION*, 73(10):1280–1295, October 2017.

[12] M. G. Fontana. *Corrosion Engineering.* McGraw-Hill, New York, 3rd edition, 1986.

[13] C. Marioara, A. Lervik, J. Grønvold, O. Lunder, S. Wenner, T. Furu, and R. Holmestad. The Correlation Between Intergranular Corrosion Resistance and Copper Content in the Precipitate Microstructure in an AA6005A Alloy. *Metallurgical and Materials Transactions A*, 49(10):5146–5156, 2018.

[14] X. Zhang, X. Zhou, and J. Nilsson. Corrosion behaviour of AA6082 Al-Mg-Si alloy extrusion: The influence of quench cooling rate. *Corrosion Science*, 150: 100–109, 2019. Publisher: Elsevier Ltd.

[15] P. Saha. *Aluminum extrusion technology.* ASM International, Materials Park, OH, 2000.

[16] J. Grønvold. *The Effect of Deformation on Intergranular Corrosion of AlMgSi Alloys.* Master's thesis. Norwegian University of Science and Technology, 2017.

[17] T. Saito, C. D. Marioara, J. Røyset, K. Marthinsen, and R. Holmestad. The effects of quench rate and pre-deformation on precipitation hardening in Al–Mg–Si alloys with different Cu amounts. *Materials Science and Engineering: A*, 609:72 – 79, 2014.

[18] J. Hatch. *Aluminum : Properties and Physical Metallurgy.* American Society for Metals, Metals Park, Ohio, 1984.

[19] T. Saito, S. Wenner, E. Osmundsen, C. D. Marioara, S. J. Andersen, J. Røyset, W. Lefebvre, and R. Holmestad. The effect of Zn on precipitation in Al-Mg-Si alloys. *Philosophical Magazine*, 94(21):2410–2425, 2014.

[20] M. Stoknes. *Effect of Copper and Zinc on Corrosion Behaviour and Mechanical Properties in 6082-Alloys.* Master's thesis. Norwegian University of Science and Technology, 2015.

[21] P. V. T. Lam. *Intergranular Corrosion of Extruded AlMgSi(Cu,Zn) Alloys.* Master's thesis. Norwegian University of Science and Technology, 2016.

[22] E. Koren. *The Effect of copper and Zinc on Surface Properties of AlMgSi.* Specialization Project. Norwegian University of Science and Technology, 2019.

[23] R. Lumley. *Fundamentals of Aluminium Metallurgy : Recent Advances.* Woodhead Publishing, Duxford, United Kingdom, 2018.

[24] ASM Int. Staff. *ASM Handbook: Properties and Selection: Nonferreous alloys and Special-Purpose Materials*, volume 2. ASM International, 1991.

[25] W. D. Callister and D. G. Retwisch. *Material Science and Engineering.* Wiley, 9th edition, 2014.

[26] H. J. McQueen, S. Spigarelli, M.E. Kassner, and E Evangeliste. *Hot Deformation and Processing of Aluminum Alloys.* CRC Press, 2011.

[27] Hydro: Technical datasheet - Extruded products Alloy EN AW-6005A [AlSiMg(A)]. URL https://www.hydro.com/Document/Index?name=Hydro%20EN%20AW%206005A.pdf&id=7821.

[28] O. Reiso. Extrusion of AlMgSi Alloys. *Materials Forum*, 28, 2004.

[29] H. Tanihata, T. Sugawara, K. Matsuda, and S. Ikeno. Effect of casting and homogenizing treatment conditions on the formation of Al–Fe–Si intermetallic compounds in 6063 Al–Mg–Si alloys. *Journal of Materials Science*, 34(6):1205–1210, 1999. Place: Dordrecht Publisher: Kluwer Academic Publishers.

[30] B. Milkereit and M. J. Starink. Quench sensitivity of Al-Mg-Si alloys: A model for linear cooling and strengthening. *Materials and Design*, 76(C):117–129, 2015.

[31] K. Strobel, M. A. Easton, L. Sweet, M. J. Couper, and J. F. Nie. Relating Quench Sensitivity to Microstructure in 6000 Series Aluminium Alloys. *Materials Transactions*, 52(5):914–919, 2011.

[32] L. Lodgaard and N. Ryum. Precipitation of dispersoids containing Mn and/or Cr in Al–Mg–Si alloys. *Materials science & engineering*, 283(1-2):144–152, 2000. Publisher: Elsevier BV.

[33] L. F Mondolfo. *Metallography of aluminium alloys*. Wiley & Sons, New York, 1943.

[34] D. R. Askeland. *The science and engineering of materials*. Thomson, Toronto, Ont, 5th edition, 2006.

[35] J. W. Evancho and J. T. Staley. Kinetics of precipitation in aluminum alloys during continuous cooling. *Metallurgical Transactions*.

[36] E. Tempelman. *Manufacturing and design : understanding the principles of how things are made*. Elsevier, Amsterdam, 1st edition, 2014.

[37] B. Milkereit, N. Wanderka, C. Schick, and O. Kessler. Continuous cooling precipitation diagrams of Al–Mg–Si alloys. *Materials Science and Engineering*, 550: 87–96, July 2012.

[38] H. LI, C. ZENG, M. HAN, J. LIU, and X. LU. Time–temperature–property curves for quench sensitivity of 6063 aluminum alloy. *Transactions of Nonferrous Metals Society of China*, 23(1):38–45, 2013. Publisher: Elsevier BV.

[39] P. Lejcek. *Grain Boundary Segregation in Metals*, volume 136 of *Springer Series in Materials Science*. Springer, Berlin, Heidelberg, 2010.

[40] J. Holmestad. *(Scanning) Transmission Electron Microscopy Studies of Grain Boundary Segregation relevant to Intergranular Corrosion in Al-Mg-Si-Cu Alloys*. NTNU, 2015.

[41] S. Pogatscher, H. Antrekowitsch, H. Leitner, D. Pöschmann, Z. L. Zhang, and P. J. Uggowitzer. Influence of interrupted quenching on artificial aging of Al–Mg–Si alloys. *Acta materialia*, 60(11):4496–4505, 2012. Publisher: Elsevier BV.

[42] K. Yamada, T. Sato, and A. Kamio. Effects of Quenching Conditions on Two-Step Aging Behavior of Al-Mg-Si Alloys. *Materials science forum*, pages 669–674, 2000.

[43] B. Milkereit, L. Giersberg, O. Kessler, and C. Schick. Isothermal Time-Temperature-Precipitation Diagram for an Aluminum Alloy 6005A by In Situ DSC Experiments. *Materials*, 7(4):2631–2649, 2014.

[44] A.H.W. Smallman and R. E. Ngan. *Modern Physical Metallurgy*. Elsevier Science, 8 edition, 2013.

[45] H. Mehrer, P. Fulde, and K. von Klitzing. *Diffusion in Solids: Fundamentals, Methods, Materials, Diffusion-Controlled Processes*. Springer, Berlin, Heidelberg, 2009.

[46] A. Chbihi, S. Vincent, J. Ribis, C. Toffolon-Masclet, and J. Garnier. Influence of plastic deformation on the precipitation sequence in an AA6061 alloy. *Journal of Materials Science*, 52(10):6063–6073, 2017. Place: New York Publisher: Springer US.

[47] K. Teichmann, C. D. Marioara, S. Andersen, and K. Marthinsen. The Effect of Preaging Deformation on the Precipitation Behavior of an Al-Mg-Si Alloy. *Metallurgical and Materials Transactions A*, 43(11):4006–4014, 2012. Place: Boston Publisher: Springer US.

[48] K. Teichmann, C. D. Marioara, S. J. Andersen, K. O. Pedersen, S Gulbrandsen-Dahl, M. Kolar, R. Holmestad, and K. Marthinsen. HRTEM study of the effect of deformation on the early precipitation behaviour in an AA6060 Al-Mg-Si alloy. *Philosophical Magazine*, 91(28):3744–3754, 2011. Publisher: Taylor & Francis Group.

[49] M. Kolar. *The effect of pre-deformation on precipitation and mechanical properties during aging of Al-Mg-Si alloys : an experimental study*, volume 2011:84 of *Doctoral thesis*. Norwegian University of Science and Technology, Trondheim, 2011.

[50] R. S. Yassar, D. P. Field, and H. Weiland. The effect of predeformation on the and precipitates and the role of Q phase in an Al–Mg–Si alloy; AA6022. *Scripta Materialia*, 53(3):299–303, 2005. Publisher: Elsevier Ltd.

[51] T. Saito, C. D. Marioara, S. J. Andersen, W. Lefebvre, and R. Holmestad. Aberration-corrected HAADF-STEM investigations of precipitate structures in Al-Mg-Si alloys with low Cu additions. *Philosophical Magazine*, 94(5):520–531, 2014. Publisher: Taylor & Francis.

[52] A. D Rollett, Gregory S. Rohrer, and F. J Humphreys. *Recrystallization and Related Annealing Phenomena*. Elsevier, third edition, 2017.

[53] M. Murayama and K. Hono. Pre-precipitate clusters and precipitation processes in Al–Mg–Si alloys. *Acta Materialia*, 47(5):1537–1548, 1999. Publisher: Elsevier Ltd.

[54] H. Znadbergen, S. Andersen, and J. Jansen. Structure determination of Mg5Si6 particles in A1 by dynamic electron diffraction studies. *Science*, 277(5330):1221–1225, 1997. Place: Washington Publisher: The American Association for the Advancement of Science.

[55] H. S. Hasting, A. G. Froseth, S. J. Andersen, R. Vissers, J. C. Walmsley, C. D. Marioara, F. Danoix, W. Lefebvre, and R. Holmestad. Composition of [beta]-precipitates in Al-Mg-Si alloys by atom probe tomography and first principles calculations.(Report). *Journal of Applied Physics*, 106(12):123527–1–123527–9, 2009. Publisher: American Institute of Physics, Inc.

[56] J. K. Solberg. *Teknologiske metaller og legeringer*. Institutt for materialteknologi, NTNU, 2008.

[57] D. J. Chakrabarti and D. E. Laughlin. Phase relations and precipitation in Al-Mg-Si alloys with Cu additions. *Progress In Materials Science*, 49(3-4):389–410, 2004.

[58] C. D. Marioara, S. J Andersen, T. N Stene, H Hasting, J Walmsley, A. T. J Van Helvoort, and R Holmestad. The effect of Cu on precipitation in Al-Mg-Si alloys. *Philosophical Magazine*, 87(23):3385–3413, 2007.

[59] C. Wolverton. Crystal structure and stability of complex precipitate phases in Al–Cu–Mg–(Si) and Al–Zn–Mg alloys. *Acta Materialia*, 49(16):3129–3142, 2001.

[60] J.R. Davis. *Corrosion of Aluminum and Aluminum Alloys*. ASM International, Materials Park, OH, 1999.

[61] G. Svenningsen, M. H. Larsen, J. C. Walmsley, Jan Halvor Nordlien, and K. Nisancioglu. Effect of artificial aging on intergranular corrosion of extruded AlMgSi alloy with small Cu content. *Corrosion Science*, 48(6):1528–1543, June 2006.

[62] W. J. Liang, P.A. Rometsch, L.F. Cao, and N. Birbilis. General aspects related to the corrosion of 6xxx series aluminium alloys: Exploring the influence of Mg/Si ratio and Cu. *Corrosion Science*, 76:119–128, 2013.

[63] P.A. Schweitzer. *Corrosion Engineering Handbook*, volume 11 of *Corrosion technology*. Marcel Dekker, New York, 1996.

[64] M. H. Larsen, J. C. Walmsley, Otto Lunder, and Kemal Nisancioglu. Effect of Excess Silicon and Small Copper Content on Intergranular Corrosion of 6000-Series Aluminum Alloys. *Journal of The Electrochemical Society*, 157(2), 2010.

[65] S. Kumari. *Initiation and Propagation of Intergranular Corrosion on AA6005 Aluminium Alloy*. Number Doctoral thesis. Norwegian University of Science and Technology, Trondheim, 2018.

[66] G. Svenningsen, M. H. Larsen, J. H. Nordlien, and K. Nisancioglu. Effect of high temperature heat treatment on intergranular corrosion of AlMgSi(Cu) model alloy. *Corrosion Science*, 48(1):258–272, January 2006.

[67] M. H. Larsen, J. C. Walmsley, O. Lunder, R. H. Mathiesen, and K. Nisancioglu.

Intergranular Corrosion of Copper-Containing AA6xxx AlMgSi Aluminum Alloys. *Journal of The Electrochemical Society*, 155(11), 2008.

[68] S. Kumari, S. Wenner, J.C. Walmsley, O. Lunder, and K. Nisancioglu. Copper enriched by dealloying as external cathode in intergranular corrosion of aluminium alloy AA6005. *Corrosion Science*, 158, 2019.

[69] A. Shi, B. A. Shaw, and E. Sikora. The Role of Grain Boundary Regions in the Localized Corrosion of a Copper-Free 6111-Like Aluminum Alloy. *Corrosion (Houston, Tex.)*, 61(6):534–547, 2005. ISSN 0010-9312. Place: Houston Publisher: NACE International.

[70] N. Birbilis and R. G. Buchheit. Electrochemical Characteristics of Intermetallic Phases in Aluminum Alloys. *Journal of The Electrochemical Society*, 152(4):B140, 2005.

[71] S.K. Kairy, P.A. Rometsch, C.H.J. Davies, and N. Birbilis. On the Electrochemical and Quasi In Situ Corrosion Response of the Q-Phase ($Al_x Cu_y Mg_z Si_w$) Intermetallic Particle in 6xxx Series Aluminum Alloys. *CORROSION*, 73(1): 87–99, January 2017.

[72] N. Birbilis and R. G. Buchheit. Investigation and Discussion of Characteristics for Intermetallic Phases Common to Aluminum Alloys as a Function of Solution pH. *Journal of The Electrochemical Society*, 155(3):C117, 2008.

[73] K. Yamaguchi and K. Tohma. Effect of Zn addition on intergranular corrosion resistance of Al-Mg-Si-Cu alloys. In *6th Int. Conf. Alum. Alloy*, volume 3, pages 1657–1662, 1998.

[74] T. Danbolt. *The Effect of Fe Content on Intergranular Corrosion Behaviour of a 6005 Aluminium Alloy.* Master thesis. Norwegian University of Science and Technology, 2019.

[75] T. Minoda and H. Yoshida. Effect of grain boundary characteristics on intergranular corrosion resistance of 6061 aluminum alloy extrusion. *Metallurgical and Materials Transactions A*, 33(9):2891–2898, 2002. Place: New York Publisher: Springer-Verlag.

[76] EN ISO 11846:1995. Corrosion of metals and alloys - Determination of resistance to intergranular corrosion of solution heat-treatable aluminium alloys., 1995.

[77] G. Frankel. Pitting corrosion of metals - A review of the critical factors. *Journal Of The Electrochemical Society*, 145(6):2186–2198, 1998. Publisher: ELECTROCHEMICAL SOC INC.

[78] Z. Szklarska-Smialowska. *Pitting corrosion of metals.* National Association of Corrosion Engineers, Houston, Tex, 1986.

[79] S. K. Kairy, P. A. Rometsch, C. H. J. Davies, and N. Birbilis. The Influence of Copper Additions and Aging on the Microstructure and Metastable Pitting of Al-Mg-Si Alloys. *Corrosion*, 71(11):1304–1307, 2015. Place: Houston Publisher: NACE International.

[80] S.K. Kairy, P.A. Rometsch, K. Diao, J.F. Nie, C.H.J. Davies, and N. Birbilis. Exploring the electrochemistry of 6xxx series aluminium alloys as a function of Si to Mg ratio, Cu content, ageing conditions and microstructure. *Electrochimica Acta*, 190:92–103, 2016. Publisher: Elsevier Ltd.

[81] K.D Ralston, N Birbilis, M Weyland, and C.R Hutchinson. The effect of precipitate size on the yield strength-pitting corrosion correlation in Al–Cu–Mg alloys. *Acta Materialia*, 58(18):5941–5948, 2010. Publisher: Elsevier Ltd.

[82] K.D Ralston, N Birbilis, M.K Cavanaugh, M Weyland, B.C Muddle, and R.K.W Marceau. Role of nanostructure in pitting of Al–Cu–Mg alloys. *Electrochimica Acta*, 55(27):7834–7842, 2010. Publisher: Elsevier Ltd.

[83] R. K Gupta, A Deschamps, M. K Cavanaugh, S. P Lynch, and N Birbilis. Relating the Early Evolution of Microstructure with the Electrochemical Response and Mechanical Performance of a Cu-Rich and Cu-Lean 7xxx Aluminum Alloy. *Journal of The Electrochemical Society*, 159(11):C492–C502, 2012. Publisher: Electrochemical Society.

[84] V. Guillaumin. Influence of overaging treatment on localized corrosion of Al 6056. *Corrosion*, 56(1):12–23, 2000. Publisher: National Assoc. of Corrosion Engineers International.

[85] K. El-Menshawy, A. El-Sayed, M. E. El-Bedawy, H. A. Ahmed, and S. M. El-Raghy. Effect of aging time at low aging temperatures on the corrosion of aluminum alloy 6061. *Corrosion Science*, 54(1):167–173, 2012. Publisher: Elsevier Ltd.

[86] A. Pitman, M. Salazar-Guapuriche, Y. Y. Zhao, and A. Greene. Correlation of Strength with Hardness and Electrical Conductivity for Aluminium Alloy 7010. *Materials science forum*, 519-521:853–858, 2006.

[87] S. Jin, T. Ngai, L. Li, S. Jia, T. Zhai, and D. Ke. Aging Response and Precipitation Behavior after 5% Pre-Deformation of an Al-Mg-Si-Cu Alloy. *Materials*, 11 (8):1422, 2018. Place: Switzerland Publisher: MDPI AG.

Appendix A

Received Materials

A.1 Homogenisation

Figure A.1 shows the measured temperature as a function of time of the received materials performed at the the Reference Center at Hydro RDS Sunndal. The homogenisation temperature was 575 °C and was kept for 2 hours and 15 minutes. The heating rate was 200-300 °C/hour and the cooling rate was 350 °C/hour.

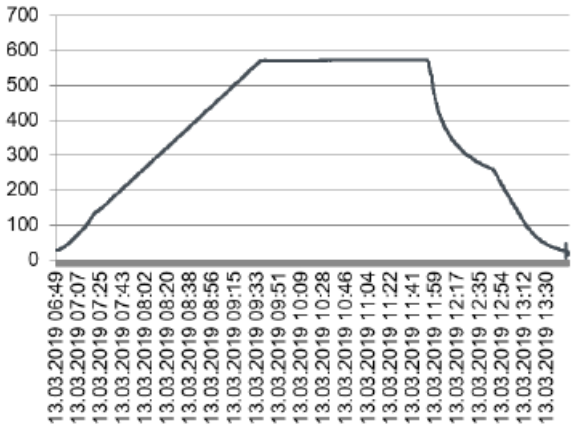

Figure A.1: Homogenization curve for billets of 6005.04 aluminium alloy.

A.2 Extrusion Parameter

The extrusion of the received materials was performed in a vertical extrusion press at SINTEF Trondheim, and the extrusion parameters are presented below:

Vertical press	800 ton
Container diameter	100 mm
Billet length	200 mm
Induction heating rate of billets	100 °C
Average billet temperature	530 °C
Container temperature	420 °C
Die	H4-1, 4x25 mm^2 with thermocouple
Extrusion ratio	78.5
Ram speed	5.6 mm/s
Profile speed	26 m/min
T profile (max)	560-570 °C
Cooling	Water quenched

A.3 Artificial Ageing

Figure A.2 shows the measured temperature as a function of time during artificial ageing of the received materials.

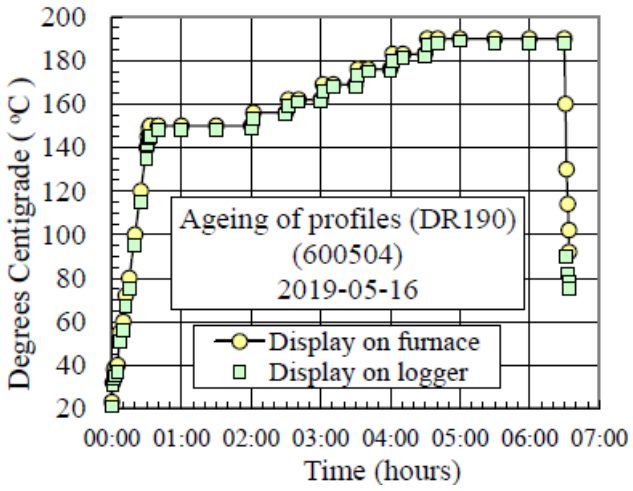

Figure A.2: Temperature profile for artificial ageing received of 6005.04 aluminium alloy extruded profiles.

Appendix B

Experimental Results

B.1 Cooling Rate From SHT

Figure B.1 shows the complete temperature profile measured during air cooling after SHT.

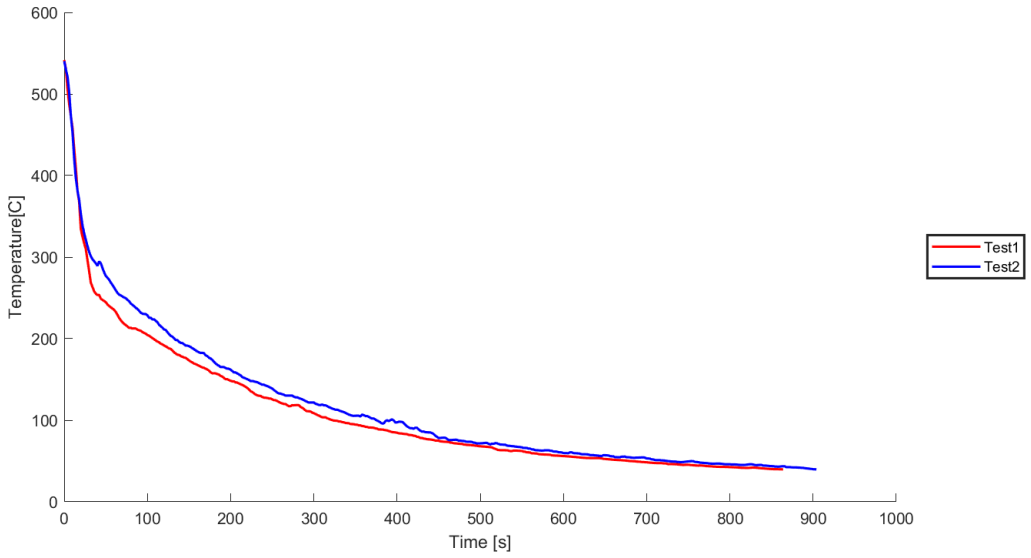

Figure B.1: Temperature profile during air cooling after SHT.

B.2 Hardness

The measured Vickers hardness of variants for all parallels are given in Table B.1. Average Vickers hardness values and standard deviations are also given.

Table B.1: Vickers hardness measurement [HV1] of all variants of composition and processing routes.

Variant	1	2	3	4	5	Avg.	Std. dev.
Cu13_Zn00_WQ_NS	112.0	111.5	114.1	115.3	109.2	112.4	2.1
Cu17_Zn00_WQ_NS	118.6	116.4	111.7	111.2	112.8	114.1	2.9
Cu14_Zn02_WQ_NS	116.1	114.9	111.4	118.2	111	114.3	2.8
Cu15_Zn03_WQ_NS	113.5	114.7	117.1	120.1	111.5	115.4	3.0
Cu13_Zn05_WQ_NS	109.7	111.4	110.8	110.0	114.9	111.4	1.9
Cu17_Zn05_WQ_NS	116.4	115.8	116.9	114.6	118.3	116.4	1.2
Cu13_Zn00_AC_NS	95.03	98.22	94.19	98.14	93.94	95.90	1.89
Cu17_Zn00_AC_NS	103.1	94.57	97.61	101.6	98.85	99.15	3.00
Cu14_Zn02_AC_NS	95.32	92.19	92.92	96.35	92.11	93.78	1.73
Cu15_Zn03_AC_NS	93.61	91.43	93.74	93.28	95.62	93.54	1.33
Cu13_Zn05_AC_NS	94.11	90.56	98.62	90.13	90.64	92.81	3.24
Cu17_Zn05_AC_NS	97.04	94.15	100.6	103.8	92.07	97.53	4.25
Cu13_Zn00_WQ_S	101.7	105.2	100.1	103.7	102.6	102.7	1.7
Cu17_Zn00_WQ_S	107.1	104.8	105.0	104.4	104.9	105.2	1.0
Cu14_Zn02_WQ_S	102.8	101.0	101.8	102.0	100.2	101.6	0.9
Cu15_Zn03_WQ_S	104.0	103.3	106.6	104.6	103.3	104.4	1.2
Cu13_Zn05_WQ_S	101.4	101.5	101.2	103.7	101.1	101.8	1.0
Cu17_Zn05_WQ_S	107.1	104.4	106.6	105.6	103.5	105.4	1.3
Cu13_Zn00_AC_S	97.04	96.13	98.58	96.13	98.31	97.24	1.04
Cu17_Zn00_AC_S	99.43	97.26	97.78	98.31	99.12	98.38	0.81
Cu14_Zn02_AC_S	95.88	95.66	99.19	98.18	96.87	97.16	1.35
Cu15_Zn03_AC_S	99.66	99.29	97.87	99.25	99.34	99.08	0.62
Cu13_Zn05_AC_S	96.61	96.31	95.66	96.05	94.28	95.78	0.81
Cu17_Zn05_AC_S	99.57	98.67	100.5	101.7	98.31	99.75	1.24

B.3 Electrical Conductivity

Electrical conductivity measurements of all variants for all parallels are shown in Table B.2. Calculated average values and standard deviations are also given.

Table B.2: Electrical conductivity measurements [MS/m] of all variations of composition and processing routes.

Variant	1	2	3	4	5	Avg.	Std. dev.
Cu13_Zn00_WQ_NS	28.62	28.73	28.85	28.76	28.86	28.76	0.09
Cu17_Zn00_WQ_NS	28.51	28.55	28.65	28.55	28.62	28.58	0.05
Cu14_Zn02_WQ_NS	28.66	28.60	28.55	28.67	28.60	28.62	0.04
Cu16_Zn03_WQ_NS	28.74	28.85	28.65	28.71	28.65	28.72	0.07
Cu13_Zn05_WQ_NS	28.53	28.59	28.63	28.69	28.63	28.61	0.05
Cu17_Zn05_WQ_NS	28.72	28.58	28.73	28.58	28.61	28.64	0.07
Cu13_Zn00_AC_NS	29.09	29.10	29.20	29.06	29.09	29.11	0.05
Cu17_Zn00_AC_NS	28.88	28.94	28.93	28.98	29.00	28.95	0.04
Cu14_Zn02_AC_NS	29.04	29.06	29.05	29.09	29.02	29.05	0.02
Cu16_Zn03_AC_NS	29.08	29.17	29.04	29.16	29.13	29.12	0.05
Cu13_Zn05_AC_NS	29.04	29.15	29.04	29.04	29.03	29.06	0.05
Cu17_Zn05_AC_NS	29.14	29.19	29.06	29.06	29.13	29.12	0.05
Cu13_Zn00_WQ_S	29.07	29.05	29.03	29.04	29.00	29.04	0.02
Cu17_Zn00_WQ_S	28.91	28.84	28.93	28.94	28.95	28.97	0.06
Cu14_Zn02_WQ_S	28.95	29.08	28.93	28.94	28.95	28.97	0.06
Cu16_Zn03_WQ_S	28.91	28.94	28.92	28.93	28.89	28.92	0.02
Cu13_Zn05_WQ_S	28.84	28.82	28.83	28.84	28.81	28.83	0.01
Cu17_Zn05_WQ_S	28.86	28.83	28.88	28.81	28.82	28.84	0.03
Cu13_Zn00_AC_S	29.19	29.23	29.18	29.21	29.20	29.20	0.02
Cu17_Zn00_AC_S	29.12	29.08	29.07	29.05	29.11	29.09	0.03
Cu14_Zn02_AC_S	29.33	29.30	29.32	29.35	29.32	29.32	0.02
Cu15_Zn03_AC_S	29.33	29.35	29.32	29.35	29.36	29.34	0.01
Cu13_Zn05_AC_S	29.24	29.25	29.31	29.28	29.30	29.28	0.03
Cu17_Zn05_AC_S	29.22	29.24	29.22	29.15	29.21	29.21	0.03

Appendix C

Results From Specialisation Project

During the specialisation project the IGC susceptibility was studied of as received materials, as no additional thermomechanical treatment was applied. The notation used in the specialisation project was different from this work:

- Variant A corresponds to the Cu13_Zn00.
- Variant B corresponds to the Cu17_Zn00.
- Variant C corresponds to the Cu13_Zn05.
- Variant D corresponds to the Cu17_Zn05.

C.1 IGC Test

Figure C.2 shows the weight loss per surface area during accelerated corrosion test as a function of time immersed in acidified chlorine solution.

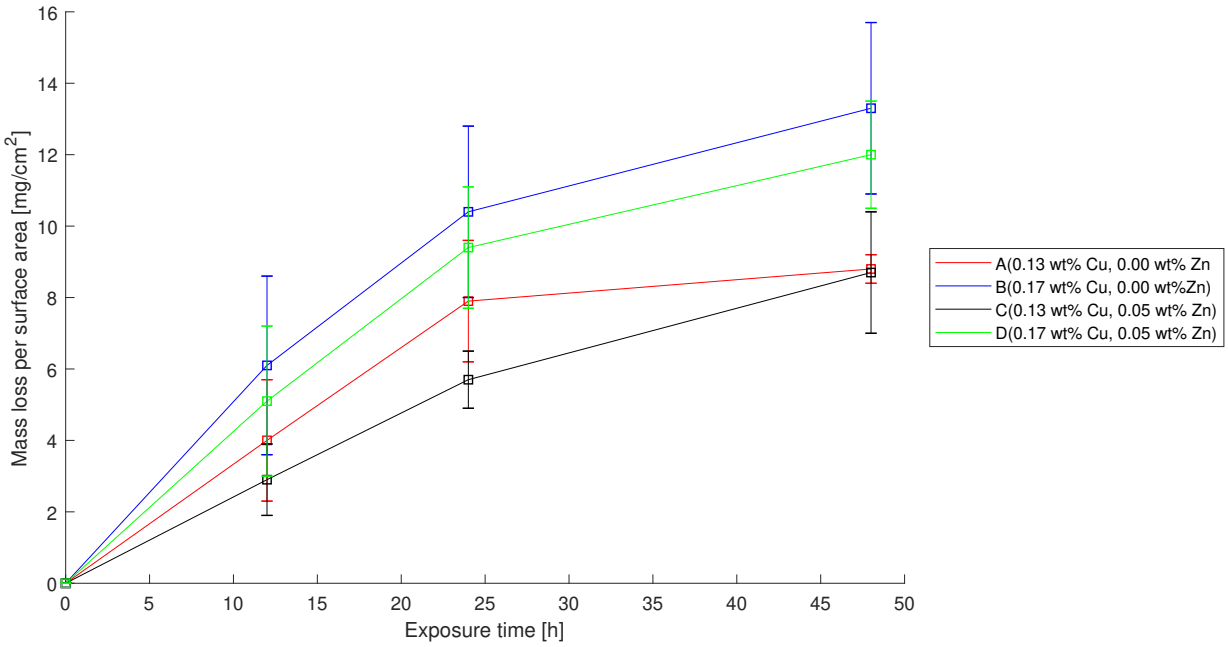

Figure C.1: Mass loss per surface area for different time exposed to acidified chlorine solution. Error bars shows one standard deviation.

Figure C.2 shows the maximum penetration depth during accelerated corrosion test as a function of time immersed in acidified chlorine solution.

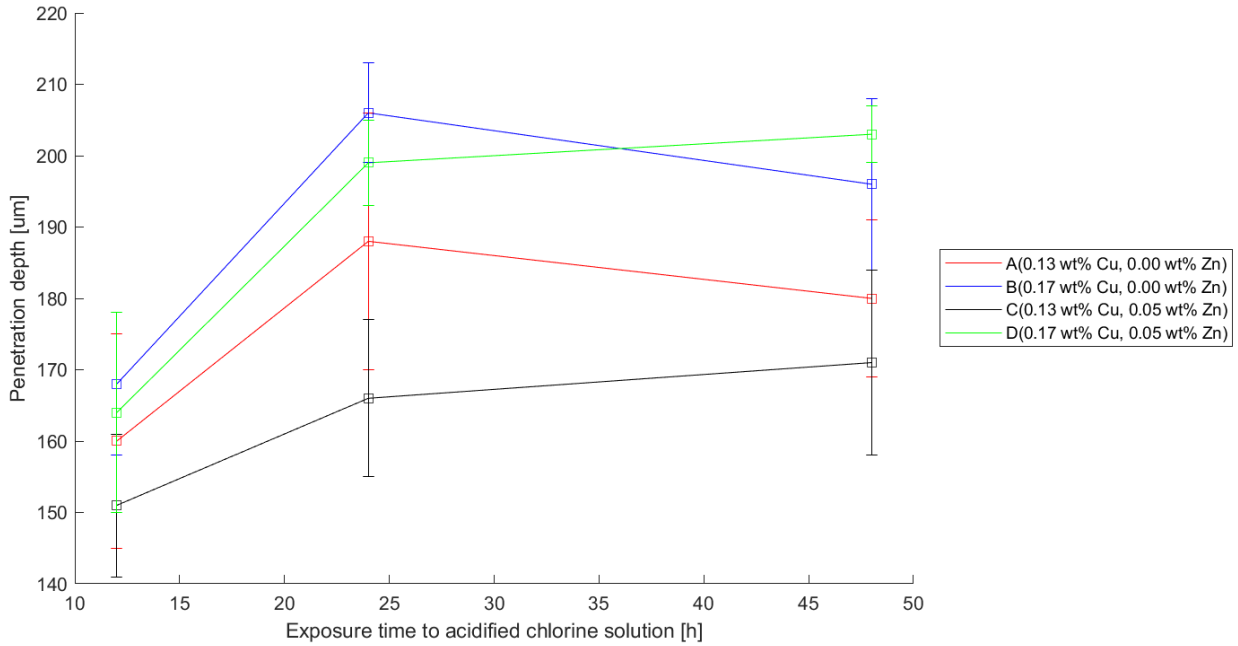

Figure C.2: Average maximum IGC penetration depth between three parallels of each of the four different alloys for increasing exposure time to acidified chlorine solution. Error bars show one standard deviation.

C.2 Conductivity Measurement

Table C.1 shows results obtained from conductivity measurements, together with calculated average and standard deviation.

Table C.1: Conductivity Measurement [MS/m]

Alloy	Avg.	Std. dev.	1	2	3	4	5	6	7	8	9	10
A	28.45	0.05	28.42	28.37	28.43	28.45	28.45	28.4	28.49	28.48	28.53	28.5
B	28.31	0.02	28.32	28.26	28.34	28.29	28.33	28.31	28.29	28.31	28.31	28.33
C	28.50	0.04	28.5	28.55	28.48	28.5	28.47	28.57	28.44	28.55	28.47	28.45
D	28.44	0.02	28.42	28.44	28.39	28.45	28.44	28.44	28.45	28.43	28.43	28.46

C.3 Hardness Measurement

Table C.2 shows all the measured Vickers hardness values, together with calculated average and standard deviation.

Table C.2: Vickers Hardness [HV1]

Alloy	Avg.	Std. dev.	1	2	3	4	5	6	7	8	9	10
A	108.8	1.8	110.2	108.1	110.7	108.9	107.6	108.3	105.2	112.2	108.9	108
B	111.4	1.3	109	111.8	113	112.1	111.3	112.5	112.9	111.5	109.4	110.6
C	108.3	1.4	105.1	109.3	108.1	109.9	108.1	107.5	109.7	108.5	106.7	109.7
D	109.9	1.0	110.7	107.9	111.7	111.7	109.3	109.6	110.4	109.8	109.1	111

NTNU

Norwegian University of
Science and Technology